

**THE LAMELLAR STRUCTURE OF  
THE SHELL OF PATELLA CRENATA:  
A CRYSTALLOGRAPHIC STUDY**

A DISSERTATION SUBMITTED FOR THE DEGREE OF DOCTOR OF  
NATURAL SCIENCES AT THE DEPARTMENT OF EARTH SCIENCES OF  
THE UNIVERSITY OF HAMBURG

BY  
**RADINA PRAMATAROVA**  
FROM SOFIA



HAMBURG  
JANUAR 2003

As a Dissertation accepted by the Department of Earth Sciences of the  
University of Hamburg

Due to the assessments of Prof. Dr. U. Bismayer  
and Prof. Dr. K. Bandel

Hamburg, 06.02.2003

Prof. Dr. U. Bismayer  
Dean  
Department of Earth Sciences

---

## **Acknowledgements**

This work was developed in the years 1999-2002 in the Mineralogisch-Petrographisches Institut of the University of Hamburg.

I would like to thank all the people without whose help this work would not be possible.

First of all I want to thank my mother, who has been helping me fatigueless to united my work, staying always beside me.

I am particularly grateful to:

- my advisor Prof. Dr. U. Bismayer. I would like to thank him for his support, insight and wisdom during our work.
- Prof. Dr. K. Bandel, who has supplied the shells and supported me in the world of molluscs.
- Dr. Carsten Paulmann for support and arrangement to make measurements in HASYLAB possible.
- Dr. K. Klaska<sup>†</sup> and Dr. J. Ludwig for their help by the X-Ray measurements.
- B. Cornelisen for her kindly help with the measurements on the Microprobe.
- Dr. Grambole, who has done the PIXE measurements in FZ Rossendorf.
- H. Lemmens from University of Antwerp, who has measured the samples on the TEM.
- Prof. Dr. H. Schleicher, making possible to take images on the Polarized Light Microscope.
- Ass. Prof. B. Mihailova for her support, especially with the Raman and IR-spectra discussion.
- Dr. Jan Ming from University of Cambridge, who has helped with the polarized IR-spectra.
- Dr. G. Adiwidjaja for measuring the samples at the Single Crystal Diffractometer.
- A. Kondyurin and E. Pecheva for measuring the polarized Raman spectra in Forschungszentrum Rossendorf.
- P. Stutz for the preparation of the thin cuts.
- David Presker, my friend, helping me studying and understanding the matter, preparing for discussion and supporting me all the time.

Deutsche Forschungsgemeinschaft (DFG) has been supporting this work within the priority program "Principles of Biomineralization" SPP 1117 for 2 years.

---

## **INTRODUCTION**

Mollusc shells are the only biomineralizing invertebrates that create an aragonitic crossed lamellar structure (Bandel, 1990). The shell of *Patella crenata* from the Canary Islands, Fuerteventura, consists of both calcitic and aragonitic crossed lamellar layers (Pramatarova et al., 2000). Details of the macroscopic structure of the layers had been studied previously (Bandel and Geldmacher, 1996). Between the outer calcitic crossed lamellar layers and the inner aragonitic material exists a ring-shaped ribbon of the attachment area of the retractor muscle; the myostracum which mainly consists of aragonite. The inner aragonitic crossed lamellar layer was found to contain prismatic intercalations with some content of organic material (Macclintock, 1967). No detailed studies on structural and orientational features within the lamellae of the calcitic and aragonitic material on a local length scale are known. Hence, inelastic light scattering techniques and X-ray diffraction was used in order to study the local and macroscopic structural characteristics of the shell of *Patella crenata*.

Some information on the biomineralization process, including the deposition of protein sheets, phase control in material chemistry (Belcher et al., 1996), and models of oscillatory zoning are available (Wand and Merino, 1992; Lee and Salje, 2000). Bandel and Geldmacher (1996) showed that the calcitic crossed lamellar layers of *Patella crenata* contain Mg, Fe, Zn, Mn, Co, and Cd while the aragonite layers preferentially contain Sr, Br, and Pb. Our spatial analysis of the distribution of Sr in the aragonitic lamellae and of Mg in the calcitic lamellae confirms significant zoning which is in agreement with the thermodynamic concept of Lee and Salje (2000). Up to now nanometer-scale features of the crossed lamellar structure of the aragonitic material were not well understood. Therefore in this work, spectroscopic, diffraction and high-resolution electron microscopy studies were performed in order to correlate macroscopic and microscopic qualities and to determine the size of the smallest well-organized clusters in the shell.

In this work we aim to elucidate on different lengths scales topological and orientational features of the crossed lamellar structure of the shell of *Patella crenata* in order to better understand the relationship between local structural characteristics and macroscopic physical properties as well as aspects of the biomineralization process.

## **CONTENT**

<b><u>I Biomineralization</u></b>	<b>1</b>
1. Biological Mineralization	1
2. Introduction to Molluscs	2
3. Gastropoda (snails, slugs and their kin)	3
3.1. Morphology	4
3.2. Classification	5
3.3. Ecology	6
3.4. Stratigraphy	7
4. Biomineralization mechanisms	7
4.1. Introduction	7
4.2. The mineralization medium	8
4.3. Nucleation	11
4.4. The organic matrix	12
4.5. Molluscan shell	13
4.6. Concluding remarks	17
<b><u>II Carbonates</u></b>	<b>19</b>
1. The Calcite Group of Minerals	19
1.1. The mineral Calcite	20
1.1.1. General Information	20
1.1.2. Crystallography	21
1.1.3. Physical Properties	22
1.1.4. Optical Properties	22
2. The Aragonite Group of Minerals	24
2.1. The mineral Aragonite	24
2.1.1. General Information	24
2.1.2. Crystallography	25
2.1.3. Physical Properties	26
2.1.4. Optical Properties	26
<b><u>III The structure of the shell of <i>Patella crenata</i></u></b>	<b>28</b>
1. Collection and sampling of <i>Patella crenata</i> shells	28
2. Shape, mesoscopic structure and development of the shell	29

---

<b><u>IV Polarized Light Microscopy</u></b>	<b>34</b>
1. Introduction	35
2. Polarized Light Microscope equipment	35
3. Results and Discussion	36
3.1. Cross section of <i>Patella crenata</i>	36
3.2. Lateral section of <i>Patella crenata</i>	37
3.3. Calcitic crossed lamellae	39
3.3.1. Crossed section	39
3.3.2. Lateral section	43
3.4. Aragonitic cross lamellae	45
3.4.1. Crossed section	46
3.4.2. Lateral section	48
3.5. Aragonitic myostracum	48
<b><u>V X-Ray diffraction</u></b>	<b>50</b>
1. X-Ray Powder Diffraction equipment	50
2. Single crystal X-Ray Diffraction equipment	51
3. Kappa-Diffractometer at F1 in HASYLAB, DESY	51
4. Results and Discussion	52
4.1. X-Ray Powder Diffraction studies	52
4.2. Single crystal X-Ray Diffraction studies	54
4.3. Kappa-Diffractometer at F1 in HASYLAB, DESY study	55
<b><u>VI Electron microscopy</u></b>	<b>57</b>
1. Scanning Electron Microscopy (SEM) investigation	57
1.1. SEM equipment and sampling	57
1.2. Results and Discussion	57
1.3. Calcitic crossed lamellae	58
1.4. Aragonitic Myostracum	61
1.5. Aragonitic Hypostracum crossed lamellae	62
2. Transmission Electron Microscopy (TEM) investigation	64
2.1. TEM equipment and sampling	65
2.2. Results and Discussion	65

---

<b><u>VII Vibrational spectroscopy</u></b>	<b>70</b>
1. IR and Raman Spectroscopy	70
2. Methods of Infrared and Raman Spectra measurements	75
2.1.Polarized IR spectra	75
2.2.Polarized Raman spectra	75
3. Results and discussion	75
3.1.IR spectra	76
3.1.1. Unpolarized IR spectra	77
3.1.2. Polarizer IR spectra	78
3.2.Raman spectra	80
3.2.1. Aragonite	80
3.2.2. Calcite	82
<b><u>VIII Chemical distribution of elements in the shell</u></b>	<b>87</b>
1. Proton Induced X-Ray Emission (PIXE) analysis	87
1.1.PIXE equipment	88
1.2.Results and Discussion	91
2. Electron Microprobe Analysis (EMPA) investigation	91
2.1.EMPA equipment	91
2.2.EMPA sample preparation	91
2.3.Results and Discussion	92
2.3.1. Aragonite	92
2.3.2. Calcite	94
2.3.3. Effects of electron interaction using EMPA	97
2.3.4. BSE images of aragonitic and calcitic crossed lamellae	99
<b><u>Conclusions</u></b>	<b>101</b>
<b><u>References</u></b>	<b>102</b>

## **Chapter I. Biomineralization**

### **1. Biological Mineralization**

Recent biological and biochemical investigations have demonstrated the ability of many living organisms to control crystallization through a biomineralization process involving the application of specialized macromolecules which enable nucleation and growth of crystalline structures of carbonates, phosphates, oxides, silicates, and other inorganic materials. By selectively inhibiting or modifying nucleation, step kinetics, surface morphologies and facet stability these organisms are able to produce nanophase materials as well as exquisite and topologically complex single-crystals and multi-layer composites. The resulting materials have biological functions as diverse as structural supports porous filtration media, grinding and cutting tools, lenses, gravity sensors and magnetic guidance systems. Technological advances in materials-based technologies often rely on the properties of single crystals, composites, interfaces and nanocrystals generated through the controlled growth of crystalline surfaces. Clearly, an understanding of the physical mechanisms by which biological systems use macromolecules to control the crystallization of inorganic compounds will provide insight into the control of synthetic crystals and enable us to produce a new array of tailored, crystalline microstructures for application across a wide range of technologies (Davis and Dove, 2000).

Calcium carbonate minerals,  $\text{CaCO}_3$ , are ubiquitous in biomineralizing systems. They are naturally occurring in marine and fresh water minerals most commonly as the polymorphs of calcite, aragonite and vaterite nucleated and grown in the exoskeletons and tissues of marine and freshwater organisms ranging from simple bacteria and algae to crustaceans, molluscs, or sponges.  $\text{CaCO}_3$  biomineral formation occurs in the oceans on such a large scale that it influences many aspects of seawater chemistry and results in sequestration of carbon in the form of carbonate sediments. In this manner, the products of biomineralization are preserved in the rock record and serve as an extensive chronicle of the interplay between biota and the earth system environment. Research has shown that the soluble fraction associated with mineralizing parts of organisms plays a primary role in biogenic carbonate formation and that this fraction is distinguished by the near-universal presence of peptide chains rich in acidic amino acids, especially polyaspartate. It is also known that carbonates exposed to different polyamino acids exhibit different bulk growth morphologies. This and related evidence suggests that systematic relationships between crystal morphology and surface interactions

with the reactive groups of the organic molecules must exist, but these relationships are unclear (Teng and Dove, 2000).

In addition to organic growth modifiers, certain inorganic impurities - in particular, magnesium and strontium - play a primary role in regulating the biomineral formation. The incorporation of  $Mg^{2+}$  has been shown to modify the morphology, solubility, and polymorphic expression of  $CaCO_3$  biominerals. Furthermore,  $Mg^{2+}$  is the principal inhibitor of calcite growth in natural waters, thereby influencing the size and reactivity of the biogeochemically-significant carbon reservoir. However, the fundamental mechanistic interactions of  $Mg^{2+}$  with the calcite surface remain controversial because investigations of the effects of  $Mg^{2+}$  on calcite have traditionally focused on macroscopic measurements of thermodynamic and morphological changes (Davis and Dove, 2001) (Teng and Dove, 1998).

The minor and trace element compositions of biogenic carbonates also reflect the chemical and physical environments in which they formed, resulting in their use as paleoclimate indicators. In particular, the Mg/Ca and Sr/Ca ratios in  $CaCO_3$  have emerged as invaluable paleotemperature proxies due to their reduced susceptibility to changes in salinity and polar ice volume relative to isotopic indicators. Besides providing critical information on crystal growth history, minor and trace elements also behave as impurities that regulate biomineral properties and formation rates. Indeed, magnesium is a principal modifier of calcite morphology and growth in natural waters. The collective influences of biological processes on the elemental composition of biominerals, termed 'vital effects', have seriously impeded efforts to unambiguously interpret biogenic mineral compositions. Further complications arise from the non-ideal partitioning behaviour observed in studies of inorganic calcite precipitation. For instance, the incorporation of  $Mg^{2+}$  and  $Sr^{2+}$  into calcite has been shown to be a function of growth rate and solution composition. Determining the thermodynamic and kinetic controls on the incorporation of trace elements in the absence of such 'vital effects' is essential to understand how organisms influence the elemental composition of biominerals (Davis and Dove, 2001).

## **2. Introduction to the Molluscs**

The total number of living mollusc species ranges from 50,000 listed by Brusca & Brusca (1990), to 60,000 mentioned by Ruppert & Barnes (1994) and to 100,000 by Kozloff (1990). Depending on the source you check, and which school of thought you prefer, the classification and taxonomy of the molluscs can vary widely. This is probably a gross underestimate of the total number of mollusc diversity, however, because there are many

underscribed species found every year in underexplored regions such as the deep and arctic seas, and both terrestrial and freshwater habitats in the tropics.

In total, there are eight classes of molluscs. There are the three major and very familiar groups: 1) clams and mussels (Bivalvia), 2) snails and slugs (Gastropoda) and 3) squids and octopuses (Cephalopoda). Then there are the less familiar chitons (Polyplacophora), and four other groups like: 1) Scaphopoda, 2) Monoplacophora, 3) Aplacophora, and 4) Caudofoveata (and the relationships of this last group are still the subject of some debate).

### Some of the general characteristics of molluscs

The name of the Phylum Mollusca itself derives from the Latin term mollusc, meaning soft, supposedly in allusion to the similarity of some snails and clams to the "mollusca" (which is a soft nut, with a thin but hard shell).

The classification of living groups of molluscs (after Brusca & Brusca 1990) is given below :

#### Living classes of Molluscs:

Class Caudofaveata (no common name – deep sea)

Class Scaphopoda (tusk shells)

Class Aplacophora (= Solenogasters) (no common name – most > 200m depth)

Class Monoplacophora (no common name – most > 200m depth)

Class Polyplacophora (chitons)

Class Bivalvia (= Pelecypoda, = Lamellibranchiata) (all the 2-shelled critters)

Class Gastropoda (snails, slugs & their kin)

Class Cephalopoda (= Siphonopoda) (cephalopods)

### **3. Class Gastropoda (snails, slugs & their kin)**

Gastropods are very diverse molluscs, occupying marine, freshwater and terrestrial environments. The most commonly known gastropods are the snails and slugs. They possess a head, foot, visceral sac, and mantle (Lehmann, 1983). The foot is flattened and termed the head-foot mass. Most gastropods have an external shell usually coiled into a corkscrew helix. The visceral mass is contained in the univalved shell which provides a shelter into which the animal can withdraw if threatened. A characteristic feature of gastropods is torsion, a process

by which the posterior mantle cavity and anus are rotated laterally and anteriorly by 180 so that they come to lie above the head. The shell then coils backwards away from the head in an endogastric position. This rotation of the mantle cavity to the front of the organism allows for better positioning of various organs (Peel, 1987). Torsion allows the sensitive head of the animal to be first into the protection of the mantle cavity, with the tougher foot forming a barrier to the outside (Hickman, 1967). The gastropod head can be moved independently of the rest of the body. Gastropods are very ecologically diverse and marine species can be found at all latitudes from the intertidal zone to 8,000 meters (Pojeta, 1987). On land, gastropods have habitats of all sorts - woodland, pastures, under rocks, underground, in trees, in small ponds or large bodies of water, and in warm springs. Factors such as the mineral content of the soil and extremes of temperature, dryness, and acidity restrict them on land. Gastropods are usually sluggish, sedentary animals. This is due to heavy shells and slow locomotory organs. Respiratory, excretory, digestive, reproductive, and nervous systems are all present in the Gastropoda. The radula is also present, with teeth varying in number from a few to many thousand (Hickman, 1961).

### 3.1. Morphology

#### Soft Parts

Soft parts of gastropods are divided into two groups; those that extend outside the shell and those that are retained within it. The head-foot protrudes outside, the visceral mass and mantle cannot (Peel, 1987). The head usually bears one or two pairs of tentacles and is connected to the visceral sac by the mobile neck. Eyes, if present, are located at the tips of the tentacles or at the bases. The foot of most gastropods is elongated, flat, muscular, and fitted for creeping. The foot is extended by blood pressure turgor with the cooperation of muscles; retraction is by powerful muscles (Hickman, 1967). The foot also possesses a mucus gland that produces a trail of slime to facilitate progress. Some species use ciliary locomotion, but in most, waves of muscular contraction pass over the foot from anterior to posterior and provide the locomotion power (Peel, 1987). The mantle secretes and lines the inside of the shell. In some, the left side of the dorsal mantle is drawn out into an inhalant siphon, which brings water into the gill. The visceral mass consists of the gonad, digestive gland, heart, and excretory organs. The mantle cavity, located near the shell aperture, contains the gill(s), osphradium(ia), hypobranchial gland(s), and openings of the digestive, excretory, and reproductive systems. The osphradium is a chemical and sediment sensitive organ. The hypobranchial glands are concerned with trapping particles that enter the mantle cavity with the respiratory current. Most species have

an internal gill used for respiration. Land snails and slugs have evolved the mantle cavity into a vascularized air-breathing lung. Some species have fleshy external gills through which they respire (Peel, 1987).

### Hard Parts

Gastropod shells consist of an outer and inner layer. The outer horny layer is termed the periostracum. The inner layer, the proper shell, is normally composed of aragonite. The shell is basically an elongate cone, rarely septate, which may be coiled in a number of ways (Clarkson, 1993). The apex is the first formed part, and the aperture is where the head-foot mass protrudes. The operculum closes the aperture when the head-foot mass is withdrawn into the safety of the shell. The shell is usually coiled around an axis of coiling. A whorl is 360° of coiling. Several shell forms are noted (after (Peel, 1987)):

- 1) Helical or conspiral - shell has form of a corkscrew helix. The apex is drawn out to one side, and is therefore three dimensional.
- 2) Planispiral - shell coils in one plane, and is two dimensional.
- 3) Isotrophic - planispiral shells that are bilaterally symmetrical about the plane in which they coil.
- 4) Anisotropic - asymmetric planispiral and helical shells.

Shell colour and pattern can also vary greatly in the gastropods (Hickman, 1967).

### **3.2. Classification**

Gastropod taxonomy is based largely on soft parts. Gills, osphradia, the heart, kidneys, and reproductive system morphologies are all important (Clarkson, 1993). The subclass names are derived from respiratory systems (Peel, 1987). This classification is based on that in the “Treatise on Invertebrate Paleontology”, by Clarkson(1993) in brief summary:

Class Gastropoda - Early Cambrian to Holocene. Asymmetrical helically coiled shell with apex pointed posteriorly away from the head. Head can be moved independently of the rest of the body. Foot sole-like and used for creeping. Visceral mass torted so that the anus and organs of the mantle cavity are above the head (Pojeta, 1987). Radula located on the floor of the mouth (Lehmann, 1983). Eyes and other sensory organs present on the head in Clarkson(1993). Gastropods live on land, and in marine and fresh waters. In marine waters, they can be found at all latitudes from the intertidal zone to 8,000 meters (Pojeta, 1987).

1. Subclass 1. Prosobranchiata - Early Cambrian to Holocene. Fully torsted gastropods with anterior mantle cavity. Mantle cavity with two gills, right gill lost in most. Principally marine, with some freshwater and terrestrial. More than half of all gastropods belong to this subclass (Peel, 1987)
  - Order 1. Archeogastropoda - Early Cambrian to Holocene. Aspidobranch gills - filaments are arranged in a double comb on either side of the axis and free at one end. Shells normally helical spires. Nearly all marine (Clarkson, 1993)
  - Order 2. Mesogastropoda - Ordovician to Holocene. Pectinibranch gills - permit free flow of water through the mantle cavity, very efficient (Clarkson, 1993)
  - Order 3. Neogastropoda - Cretaceous to Holocene. Pectinibranch gills, inhalant siphon present (Clarkson, 1993).
2. Subclass 2. Opisthobranchiata - Mississippian to Holocene. Usually strongly detorted gastropods. Shell commonly concealed in mantle or absent. One internal gill, or in shell-less forms, with external gills (Peel, 1987).
3. Subclass 3. Pulmonata - Mesozoic to Holocene. Detorted Gastropods with conspiral shell commonly present, sometimes reduced and concealed in mantle (Peel, 1987).

Land dwellers and secondary freshwater dwelling snails and slugs. Gills are lost and entire surface of the mantle cavity is modified as a lung. The pulmonates are the only group of molluscs that have made the successful transition to land (Clarkson, 1993).

### **3.3. Ecology**

The gastropods are a very diverse ecological group. Most are aquatic, in both marine and freshwater, but many are terrestrial. Dodd (1981) divides them ecologically into five groups based on locomotion and attachment:

- 1) Crawling - moving about on a hard substrate, including other organisms.
- 2) Burrowing - moving through the soft substrate.
- 3) Cemented - attached to substrate by secreted shell material.
- 4) Foot attached - attached to one place, often on the shell of another organism.
- 5) Planktonic - suspended in the water.

Gastropods can be found at all depths of the ocean from intertidal to abyssal, and at all latitudes. They are most common in the sea in the littoral zone (Hickman, 1961). An amazing adaptive radiation has allowed them to move into most kinds of ecological niches and into

nearly every area on earth. Gastropods can even be found at mountainous altitudes of 4.6 km to 6 km (Hickman, 1967).

Species number between 35,000 and 40,000. Sizes can range from 1 millimeter to more than 2 feet long, with fossil forms much larger even still (Hickman, 1967).

Gastropods take on a variety of feeding habits. They are provided with a radula, a belt of serially arranged teeth within the mouth. This makes them adaptable as herbivores, carnivores, or scavengers.

Some carnivores can rasp away at the shell of another gastropod or bivalve to reach the flesh. They drill a neat, round hole over a period of 14-20 hours and inject a muscle relaxant which opens up the shell to dinner (Clarkson, 1993). Suspension feeders produce ciliated currents to circulate water containing suspended plankton and organic matter through the mantle cavity, where it is trapped on the gills. Many are scavengers on dead organisms, while others are herbivores, feeding on algae or other higher plants by use of the radula (Dodd (1981)).

### **3.4. Stratigraphy**

The gastropods are not as important for dating terrestrial rocks as are some of the other molluscan classes. However, they are extremely useful in the reconstruction of the conditions of the past, i.e. paleoenvironment. Gastropod forms have changed very little since the beginning of the Cenozoic. Therefore, by knowing the present day way of life of gastropods, and assuming a similar pattern for the fossil species, conclusions of paleoenvironment can be drawn (Pinna, 1973). Dodd (1981) uses this method, and refers to it as "taxonomic uniformitarianism". Tertiary-Pleistocene gastropods have numerous living representatives, and it is possible therefore to relate present habitat to the fossil record (Tasch, 1973).

## **4. Biomineralization mechanisms (Carter, 1990)**

### **4.1 Introduction**

Biomineralization is a complex process (Weiner, 1986) that involves the controlled nucleation and growth of ceramics from aqueous solutions.

Biomineralization has been divided into two fundamentally different types based on the degree of biological control (Lowenstam 1981): The secondary precipitation of mineral as result of interactions between biological activity and the environment was considered as "biologically-induced" mineralization. In this type, the biological system exercises little control over the type and habit deposited although biological surfaces may be important in the

induction of the mineral. In the second type of biomineralization termed “organic matrix-mediated” mineralization, the genetically programmed organic matrix controls the nucleation, growth and microarchitecture of the mineral deposited. The initial stages of mineral induction is probably very similar in the two types of biomineralization.

If each of the large variety of minerals deposited by organisms are formed by a unique process, then the possibility of understanding the mechanisms by which these minerals are formed is remote. A more fruitful approach is to assume that the basic processes of mineral formation are common to all systems and may diverge from the common pathway. This means that comparison between systems can be made to good advantage.

#### **4.2. The mineralization medium**

For mineral formation to occur, the local site must be sufficiently supersaturated. In most system, the locus of mineral deposition is isolated from the environment. However, the extent of isolation may vary from that of incrusting marine algae where diffusion may be restricted by the viscosity and environment only slightly different to that of the external medium, to an intracellular site where the composition at the locus is very precisely regulated.

For mineralization to proceed there must be mechanisms for the continuous supply of lattice ions to and the removal of hydrogen ions, generated by mineral deposition, from the locus of mineral deposition. The net ion transport must be such that there is no charge separation. In those simple systems where no cellular membrane separates the locus from a sufficiently supersaturated fluid, the required ion movement can be accomplished by diffusion. The transport of lattice ions across membranes is more complex. Generally, control of the transport of anions, such as phosphate and carbonate or bicarbonate, is indirect and contingent on the transport of cations. (Sachs 1977).

In calcium carbonate-forming systems, the inorganic carbon may reach the locus as carbon dioxide because the rate at which this gas diffuses through membranes is several orders of magnitude that of bicarbonate or carbonate. In fact, respiratory CO<sub>2</sub> produced by some metazoans may supply some or all the inorganic carbon for mineralization (Sikes et al., 1981). Of course, the supply of inorganic carbon as CO<sub>2</sub> instead of bicarbonate or carbonate calls for the removal of more hydrogen ions. The removal of hydrogen ions from the mineralization locus in molluscs seems to be a function of carbonic anhydrase bound to the outer membrane of the mantle (Wheeler, 1975). Another proposed mechanism is an exchange of two hydrogen ions for each calcium ion actively transported to the mineralization locus. (Niggli et al., 1982).

Coccolithophorids appear not to generate hydrogen ions during mineral formation because inorganic carbon enters the cell as bicarbonate (Crenshaw, 1964; Sikes et al., 1981 and Wheeler, 1983). The overall reaction for the process,



is electrically neutral. Part of the driving force for this reaction is the removal of  $\text{CO}_2$  by its fixation in photosynthesis. (Crenshaw, 1964).

Analyses of molluscan extrapallial fluids were made for the purpose of describing the physiochemical environment at the locus of shell formation specifically and as a general model for metazoan mineralization. (Crenshaw, 1972b; Wada and Fujinuki, 1976; Misogianes and Chasteen, 1979). This fluid also contains proteins and complex carbohydrates (Kobayashi, 1984a,b), some of which bind calcium. (Crenshaw, 1972b; Misogianes and Chasteen, 1979). The pH of the extrapallial fluid and therefore, the degree of saturation, varies with the metabolic state of the mollusc (Crenshaw and Neff, 1969; Crenshaw, 1972b; Wijnsman, 1975; Gordon and Carriker, 1978). When inorganic composition was corrected for calcium binding by macromolecules, inorganic complex formation, and ionic strength it was supersaturated with respect to both calcite and aragonite when the molluscs were aerobic (Greenfield, 1987).

The experience with the molluscan extrapallial fluid illustrate the difficulties in obtaining a clear definition of the physical parameters at the locus of mineral deposition at the time of mineral deposition. Another approach is to work with model systems. The effects of putative promoters and inhibitors of mineralization, individually and in combination, can be studied in these model systems which can be made increasingly complex as knowledge advances. In order that comparison can be made, the conditions of each system must be precisely identified, especially the degree of saturation. The degree of saturation ( $\Omega$ ) is usually expressed as the ratio of ion activity product (IAP) of the solution to the thermodynamic solubility product of the mineral. ( $K_{so}$ ). Calculations of the ion activity product must take into account the total ion concentrations, complex formation, mass balance, electrical neutrality, pH and ionic strength. Ion activities can be calculated from known concentrations using available computer programs. (see Nordstrom et al., 1979 for some examples).

Although the degree of supersaturation describes the thermodynamic driving force for mineral precipitation, precipitation may be determined to a greater extent by kinetic factors. In order that a nucleus or crystal grows, lattice ions must be transported to the surface, absorbed,

migrate on the surface to a growth site and be integrated into the structure. At some stage, the ions must be dehydrated. The slowest of these steps will be the limiting one. (Nielsen and Christoffersen, 1982).

Transport control of mineral formation was demonstrated by comparing the spontaneous precipitation of calcium carbonate from unstirred and stirred solutions ( $\Omega_{\text{calcite}} > 450$ ) (Reddy, 1986). Precipitation from the unstirred solutions leveled off after sixty minutes at  $\Omega \cong 25$ . In the stirred solutions, mineral formation continued through 100 minutes when the  $\Omega$  was  $< 2$ . Mineral formation in biological systems is probably transport controlled to a significant extent because the solution at the locus of mineralization is not well mixed.

The effect of some foreign ions is another example of kinetic factors that control mineral formation. Magnesium ions have a significant influence on calcium carbonate formation, slowing calcite and vaterite formation while favoring aragonite precipitation. (see Kitano et al., 1976 for review). This ion reduces or inhibits, depending on the Mg concentration, the precipitation of calcite from stirred, metastable solutions ( $\Omega < 10$ ) that are seeded with calcite crystals. This effect appears to be caused by the magnesium ion's blocking the growth sites on the seed (Reddy, 1986).

The precipitation of mineral will change the composition of the solution and thus, the degree of saturation. The changes in saturation may favor the precipitation of different phases and the dissolution of the initial mineral phases during an experiment. If only the initial stages of mineral formation are being studied, these changes can be ignored, but only in a first approximation. For example, the initial decrease in pH has been used often as an indicator of the start of mineral formation. If the observations are extended into subsequent growth, some provision must be made for maintaining a constant solution composition. (Nancollas, 1982b).

Generally, the rate of reaction is a function of the degree of supersaturation and the concentration of active sites added to induce mineral formation. When the inducing substance (seed) is a mineral, relatively large concentrations of active sites and therefore, lower levels of supersaturation can be used. Here the active sites are imperfections on the crystal surface, and their concentration is proportional to the surface area of the seed. When organic molecules provide the active sites, the number of the active sites undoubtedly varies from one macromolecule to another and is probably related to the number and configuration of certain side chains instead of the surface area. Also, it is very difficult to prepare large quantities of putative macromolecular seeds. Higher levels of supersaturation may overcome this preparative problem. However, the induction time (time elapsed from the addition of the seed until mineral first is detected) is proportional to the degree of supersaturation, and induction

time is a parameter used to describe the relative potency of putative seeds. Thus, the higher levels of supersaturation used to overcome the preparative problems could be self-defeating. Spontaneously precipitation solutions certainly cannot be used to differentiate mineral putative nucleation among the components of a matrix.

### 4.3. Nucleation

The solution at the locus of mineral formation in a biological system is supersaturated with respect to the mineral formed. Otherwise, the mineral would not precipitate nor grow. However, the condition of supersaturation, alone, is not sufficient for a mineral to begin to precipitate. In order that this new solid phase forms in the solution, energy barriers (activation energy) must be overcome. This process is termed nucleation.

There are two types of primary nucleation, homogeneous and heterogeneous. Homogeneous nucleation is the spontaneous formation of nuclei in a supersaturated solution. This type of nucleation is rarely observed because it is almost impossible to prepare solution free from foreign surfaces, like impurities. Heterogeneous nucleation involves the formation of nuclei on a foreign surface and requires a much lower degree of supersaturation. The principle second type of nucleation is secondary nucleation which occurs because of the presence in the solution of crystals of the mineral being precipitated.

Although homogeneous nucleation is rarely observed, the essential elements of the process are applicable to mineral nucleation in biological systems. In a given supersaturated solution, clusters of aggregates of ions form. The driving force for the formation of the clusters is the free energy of the phase change from liquid to solid. These clusters are unstable because they have a high surface free energy, i.e., the clusters are so small that the ions of molecules are held together by relatively weak bonds and the specific surface area is large. Therefore, the clusters are much more soluble than the mineral that may be precipitated from the solution. The free energy of the clusters is the sum of term for energy of formation and the surface energy term. As these clusters grow to reach a critical size, the free energy of these clusters undergoes a maximum, the activation energy. The rate at which clusters exceed the activation energy barrier is the rate of nucleation. Each cluster in the solution tends to change its size to decrease its total free energy. Therefore, clusters smaller than the crystal size will dissolve rapidly, and clusters larger than the crystal size are nuclei and will grow as long as the solute concentration exceeds the solubility product (Garside, 1982).

The growth of the larger clusters or crystals at the expense of smaller clusters or crystals is known as Ostwald ripening. Clusters and nuclei also grow by agglomeration when two

particles approximate so closely that surface migration can contribute the transport of mineral to the growing centre. The presence of a substrate (e.g. an organic matrix) in the solution significantly reduces the activation energy for nucleation by reducing the surface free energy. Therefore, heterogeneous nucleation occurs at lower levels of supersaturation and at faster rates of any given level of supersaturation (Nielsen and Christoffersen, 1982).

Estimates of the size of the crystal nucleus vary from a general value of 10-1000 ions (5-20 angstroms; Mann, 1983) to 4 ions calculated for the calcium carbonate monohydrate nucleated on a sulfonated polymer surface (Dalas et al., 1988): The structure of the initial nucleus is largely unknown because of its small size, hydration and unknown nature. The degree of hydration of the initial nucleus is particularly important in the determining the initial mineral phase deposited on the surface of an organic substrate. The model used in classical nucleation theory considers that the initial nucleus resembles the structure of the bulk crystal. The ions are assumed to be dehydrated, and they interact strongly. At the other extreme, the initial nucleus is a cluster of hydrated ions that interact weakly. In this model, movement of the ions is less restricted, and its structure can be quite different form that of the mineral subsequently formed (Mann, 1983).

The empirical observation known as the Ostwald-Lussac rule of stages predicts that, from a solution supersaturated with respect to more than one mineral, the initial mineral formed is the one with the highest solubility. Since amorphous and hydrated minerals tend to be more soluble, the Osrwald-Lussac rule predicts that these would be formed first.

The presence of substrate may alter the phases formed. Using low levels of supersaturation ( $\Omega = 1.0-2.25$ ), Dalas et al., (1988) found that calcium carbonate monohydrate was the first crystalline phase deposited on sulfonated polystyrene and polystyrene divinylbenzene polymers from calcium bicarbonate solutions at constant composition. Later this initially-formed phase transformed into the thermodynamically stable polymorph, calcite.

#### **4.4 The organic matrix**

The organic matrix has been assigned several functions including, nucleating the mineral, determining the mineral phase deposited and controlling crystallographic orientation and growth. Any understanding of the mechanisms of biomineralization depends upon knowing 1) which functions actually are carried out by the organic matrix, 2) which components of the matrix have primary roles in each function, and 3) whether the entire matrix assembly is required for each function.

Epitaxy is often stated or implied as the mechanism by which a mineral is nucleated by the organic matrix. If the matching at atomic dimensions of the surface of the organic matrix with the lattice of the mineral deposits obtains as this mechanism requires, that the mineral phase deposited and its crystallographic orientation are determined by the nucleation process. However, nucleation of the mineral by the matrix can be accomplished by other mechanisms that do not require such a rigid two-dimensional organization of the matrix. Ions or ion clusters in solution could form chemical bonds with oppositely charged groups at the matrix surface. The highly mobile nuclei formed may undergo surface dissolution, and the translocated ions be epitaxially deposited on the unoriented, possibly cryptocrystalline, nuclei. If this mechanism occurs, the matrix may not be directly involved in processes subsequent to nucleation. Alternatively, the rearrangement of initial nuclei may be controlled by chemical interactions between the crystallites and the matrix surface. In either case, the final mineral formed may be different from that initially deposited (Mann, 1983).

#### 4.5. Molluscan shell

While investigations related to the mechanisms of mineralization in the collagen-based systems are just beginning, some progress has been made in the study of molluscan shell formation. Recent investigations have focused on the actual mechanisms of mineralization and have provided exciting results.

The insoluble residue from demineralised shell, termed conchiolin, was thought to be the agent responsible for the induction of mineral and control of its subsequent growth. Conchiolin contains varying amounts of several proteins and polysaccharides (Gegoire et al., 1955), including chitin (Goffinet et al., 1977) and glycosaminoglycans (Simkiss, 1965). Conchiolin was analysed to find whether there were initial crystals are formed in stacked nacre (Wise and Hay, 1968a; Erben, 1974). It was concluded that the calciumbinding sites nucleated the mineral (Crenshaw and Ristedt, 1975, 1976). The observation that the calcifying granules initially deposited on substrates inserted between the mantle and the shell of bivalves contained protein, acidic polysaccharides and ester sulfate (Wada, 1980) is consistent with this conclusion.

The matrix from the septal nacre of *Nautilus pompilius* can induce mineral formation from solution having low levels of supersaturation ( $\Omega_{\text{calcite}} = 3,3$ ;  $\Omega_{\text{aragonite}} = 2,5$ ) (Greenfield et al., 1984; Greenfield, 1987; Greenfield and Crenshaw, 1988). The authors stated that mineral induction occurred only when the soluble matrix was fixed *in situ* with a quaternary ammonium salt during decalcification. Interlamellar matrix prepared without a quaternary

ammonium salt or at high ionic strengths, conditions which dissolve the soluble matrix from the interlamellar matrix, did not induce mineral formation, even when the calcium activity was increased eight-fold. An induction time of six to eight hours was required for the deposition of spherulites on the whole matrix. When the calcium concentration in the solution was increased three-fold ( $\Omega_{\text{calcite}} = 11.5$ ), acicular crystals were formed with their long axes perpendicular to the matrix surface. Infrared analysis indicated these crystals were aragonite. The mineralization solutions were kept by the authors at low ionic strength ( $> 0.02$ ) to prevent the solubilization of the soluble matrix-quaternary ammonium complex and contained no magnesium. For this reason, calcite rather than aragonite was expected. The higher saturation might have allowed the initially deposited mineral to undergo a transformation to aragonite. This solution translocation of lattice ions might have been influenced by the aspartic acid-rich proteins of the soluble matrix. Overgrowth onto the oriented conchiolin also may have been a factor. Alternatively, the formation of aragonite simply might have been an expression of the Ostwald-Lussac rule.

Most current hypotheses about the function of the soluble matrix assume that it has primary role in initial crystal formation. However, the soluble matrix obtained from oyster shells and sea urchin tests inhibited calcium carbonate nucleation and crystal growth from spontaneously precipitating solutions (Wheeler et al., 1981; Wheeler and Sikes, 1984; Swift et al., 1986). When added to cultures of sea urchin embryos these soluble matrices also inhibited calcium carbonate deposition by the embryos (Sikes and Wheeler, 1986; Swift et al., 1986). The added soluble matrix was incorporated into the formed mineral in both, the in vivo and in vitro studies. The habits of the calcite crystals precipitated in the presence of soluble matrix were quite different from the habits of crystals formed from control solutions (Wheeler and Sikes, 1984;). Such a morphological change may be caused by the adsorption of an inhibitor to the growth sites (Mann, 1983). The control by the organic matrix of the habit of the crystals deposited is one of the characteristics of matrix-mediated biomineralization (Lowenstam 1981).

The influence of fractions of the soluble matrix on the habit of spontaneously precipitating crystals was examined more thoroughly by Addadi and Weiner (1985; 1986) as described below.

Aspartic acid-rich fractions from the calcitic and aragonitic layers of *Mytilus californianus* adsorbed onto specific faces of spontaneously precipitating calcium dicarboxylates. As the crystals grew, the faces into which protein was adsorbed became more prominent. This stereochemical effect was confined to those faces with one set of

carboxylates approximately perpendicular to the face. Poly(aspartic acid) had the same stereochemical effect on the development of the crystal faces.

The equivalent {001} face of calcite with its planar arrangement of carbonate ions was expressed only 1-3% of spontaneously precipitated calcite crystals deposited on poly(styrene) films in the absence of protein. When the aspartic acid-rich fraction first was adsorbed onto poly(styrene), the calcite crystals formed in contact with the container surface had the normal rhombohedral habit of calcite, but 5.30% of them had a small well-developed {001} face. The {104} faces of remaining crystals were in contact with the container surface. The absorption of protein on {001} face was demonstrated with a fluorescent antibody to the protein fraction. Adsorbed poly(aspartic acid) alone did not induce {001} face of calcite although the adsorbed polymer can assume  $\beta$ -pleated sheet domains detectable by infrared analysis Addadi and Weiner (1985; 1986). An aspartic acid-rich glycoprotein adsorbed onto poly(styrene) also caused an increase in the fraction of oriented crystals (Addadi et al., 1987). It was concluded that calcite crystals were nucleated by an epitaxial matching of the lattice spacing of carbonate on the {001} face of calcite by the calcium bound by the carboxylate groups of the protein. The  $\beta$ -pleated sheet structure of proteins was considered as rigid in these studies. Other proteins with this conformation are not (Creighton, 1984). Thus, the conformation required for the proteins to interact with specific faces could have been induced by the structure of the crystal face.

The sulfonation of poly(styrene) films increased the fraction (up to 60-65%) of spontaneously precipitated calcite crystals having the {001} face in contact with the surface without adsorbed protein (Addadi et al., 1987). Less dramatic increases in calcite crystal orientation were found when the aspartic acid-rich fraction of the soluble matrix or poly(aspartic acid) were adsorbed onto poly(styrene) films sulfonated to such an extent that an optimal number of crystals and fraction of oriented crystals were no longer precipitated. The reported results are difficult to interpret because of the changes in the surface of poly(styrene) films that occurred with increasing sulfonation. The surface area and the topology of the substrate were undoubtedly changed so that non-specific surface effects may have influenced the results. In this series of studies, calcium carbonate was precipitated by slow diffusion of ammonium carbonate into a solution of calcium chloride. Only the initial calcium concentration were given.

Rieke (1988a,b) also studied the deposition of calcium carbonate onto the surface of polymers and glass. He also used the slow diffusion of ammonium carbonate into calcium chloride solutions to precipitate calcium carbonate. Mineral formation was observed when the

solutions reached a pH of 11-12 non-typical for biosystems. Bore calcium carbonate crystals were deposited on horizontal surface than on vertical surface of glass and poly(styrene) suspended in the same vessel. This difference was caused by the sedimentation of crystal precursors from the solution onto the horizontal surface. He concluded that nucleation occurred in solution and that those nuclei which became attached to a surface converted to a crystalline motif, calcite on glass and vaterite on poly(styrene).

Stearic acid monolayers have also been used to investigate specific compositions associated with the different mineral polymorphs, calcite and aragonite, and with the different shell structures (see Wilbur and Simkiss, 1968 and Gregoire, 1972a for review). Any differences in amino acid composition associated with the polymorphs deposited or with the different shell layer types are less than the variations between taxonomic groups (Gregoire, 1972a; Creshaw, 1982). Now conchiolin is thought to provide the organizational framework for the shell, and acidic macromolecules associated with this network are thought to nucleate and regulate mineral deposition.

Nacre is a simple molluscan shell structure, and the microstructure of the several types of nacre is well known (Carter, 1980b; Carter and Clark, 1985). The polyhedral to rounded aragonitic tablets are arranged in lamellae parallel to the inner shell surface. The b-axis is aligned approximately perpendicular to the growing edge of nacre (Wada, 1961b). The aragonite tablets were determined to be single crystals or twins by x-ray diffraction (Wada, 1965). In the stacked nacre of *Nautilus*, the a- and b- axes of adjacent tablets in a lamella and in successive lamellae are aligned. In archeogastropod stacked nacre and in pelecypod nacre, there is no such alignment of the a- and b-axes of adjacent tablets.

The structural organisation of nacreous conchiolin is complex and not as well understood as that of collagen. The mineral lamellae alternate with sheets of interlamellar matrix. The individual nacreous tablets within a lamella are separated by intercrystalline matrix which circumscribes each mineral tablet and extends between two successive sheets of the interlamellar matrix. The structure of nacreous conchiolin has been studied extensively (see Gregoire, 1976; 1972a for review). Sheets of interlamellar matrix are obtained by peeling the sheets off as the nacre is demineralised. The intercrystalline matrix collapses as cords on these sheets to form outlines of the tablets ("crystal imprints") that were present before demineralisation. The sheets of interlamellar conchiolin form lacey networks of trabeculae delimiting a series of pores. The patterns and structure of the trabeculae and pores are characteristic of the molluscan family. In cephalopods the aragonite b-axis was found to be oriented parallel to the long axis of the trabeculae (Gregoire, 1962).

More precise study of the correspondence between the structure of nacreous conchiolin and the axes of the overlying aragonite crystals was carried out by X-ray diffraction (Weiner and Traub, 1980). Only the nacreous conchiolin of cephalopod *Nautilus repertus* shows orientation of the specimen. The  $\beta$ -chitin fiber axis and that of polypeptide in  $\beta$ -pleated sheet conformation, like silk fibroins, were parallel to the plane of the interlamellar matrix. The two fiber axes were perpendicular to one another. It was found that the a-axis of aragonite was aligned with the b-axis of chitin and the a-axis of protein; and the c-axis of aragonite was aligned with the side chain direction (c-axis) of protein which is perpendicular to the plane of interlamellar matrix. Eith electron diffraction tha nacre conchiolin from the archaeogastropod *Tectus detatus* and the pelecypod *Pinctada margaritacea* also were found to have the aragonite b-axis aligned with the  $\beta$ -paleated polypeptide chains (Weiner et al., 1983). However, this highly oriented substrate may not function as a template for mineral deposition for the mineral because of the poor match between the Ca-Ca distance in the aragonite crystal lattice and potential binding sites in the polypeptide chain (Weiner, 1981).

#### **4.6. Concluding remarks**

The up to now still rudimentary understanding of the mechanisms of biomineralization can be summarized from literature briefly as follows:

- 1) The supersaturation at any mineralization locus probably varies with the time. Knowing how biological systems control saturation will enhance the understanding of the driving force for mineral formation. Currently the mechanisms for the control of lattice ion transport and regulation of pH have been described only to a limited extent in only a few systems.
- 2) Significant initial progress has been made in determining mechanisms by which the organic matrix can regulate crystal growth. Some of this control seems to be exercised by face-specific adsorption of certain matrix polyanions onto growing crystals.
- 3) An understanding of mechanisms of crystal nucleation by the organic matrix remains a goal. The frequent use of spontaneously precipitating solutions might have hindered progress on this front.

In spite of an overwhelming number of publications and support devoted to research on vertebrate mineralised tissues, most of the progress toward an understanding of biomineralization has been made from research on invertebrate systems, especially molluscan shell formation. Therefore, any hypothesis on the mechanisms of biomineralization is based primarily on that system.

Weiner and coworkers (Weiner et al., 1983, Weiner and Traub, 1984; Weiner, 1986) focused attention on the progress of biomineralization and the features of this process common to many systems. They proposed that the crystals are deposited on a pre-formed matrix template by epitaxy. This template is formed by the aspartic acid-rich proteins of the soluble matrix which are assumed to adopt a  $\beta$ -pleated sheet conformation alignment with the fibroin-like polypeptide chains of the insoluble matrix. At the nucleation site, anionic groups of the aspartic acid-rich proteins are ordered so that, there is an atomic matching of these groups with crystal lattice. When the local concentrations of the lattice ions are sufficiently high, oriented crystals are formed at the nucleation sites.

One feature of the template model proposed (Weiner et al., 1983, Weiner and Traub, 1984; Weiner, 1986) seems untenable. If the pre-formed matrix includes stacks of unmineralized compartments having their full complement of nucleation sites, then the compartments nearer the supply of lattice ions from the tissues would mineralize first. The pre-formed compartment hypothesis was taken from the work of Bevelander and Nakahara (cf. Nakahara, 1983 for review). The pre-formed compartments have been challenged as decalcification artefacts (Erben, 1972, 1974; Crenshaw, 1980; Watabe, 1981a; Wilbur and Saleuddin, 1983).

Current information indicates that the mineral may not be nucleated by structural match between ionic groups of the matrix and those of the crystal lattice. There is no compelling evidence that any one molecule or group of molecules nucleate a specific crystalline phase. It seems more probable that quasi-amorphous, hydrated nuclei are formed at or are attracted to the charged surface of the matrix and that these nuclei, with the addition of lattice ions from solution, are reorganized to form crystals. The habit of the crystals is determined by face-specific adsorption of acidic macromolecules. Polymorph selection also may be determined by stereochemical parameters. The highly organized insoluble matrix, where it exists, undoubtedly exerts some control over crystal formation. This control may be expressed in the components of the soluble matrix. The topography of conchiolin also may directly influence the morphology of overgrowing mineral.

## **Chapter II. The Carbonates**

The carbonates, related nitrates and borates are common constituents of the earth's near-surface crust. The minerals are a structurally-related as well as chemically-related group. The basic anionic (negatively charged) unit consists of a triangle where a carbon, a nitrogen or a boron atom resides at the centre. At every corner of the triangle an oxygen atom is positioned. The threefold symmetry of the triangle explains the symmetry that many corresponding minerals possess. As long as the triangles of the anionic group are in a plane parallel to the plane of the triangle and all other bonds in the structure, when viewed perpendicular to this plane, are multiples of three and are evenly separated from each other, the mineral displays a trigonal symmetry.

### **1. The Calcite Group of Minerals**

The calcite group is composed of minerals of the general formula  $ACO_3$ , where "A" can be one or more positive two-charged metal ions particularly calcium, cobalt, iron, magnesium, zinc, cadmium, manganese and/or nickel. The symmetry of the members of this group is trigonal,  $\bar{3}2/m$ . The structure consists of layers of metal ions A alternating with stacks of carbonate layers. The carbonate layers are composed of flat triangle-shaped carbonate groups ( $CO_3$ ), with a carbon atom at the centre of the triangle and the three oxygens at each corner. This triangular structural element is the key group in the trigonal symmetry of this group. Besides, the metal ions must fall into place within the symmetrical arrangement in order to preserve the trigonal symmetry.

The calcite group is an interesting contrast to the aragonite group of minerals. The structure of the calcite group is stable at normal temperature and pressure only when including smaller metal ions than the aragonite group. In case the ion is larger than calcium, the mineral's structure will be of the aragonite group, and if the ion is smaller than calcium than the mineral's structure will be of the calcite group. The mineral aragonite is dimorphous with the mineral calcite relating the same calcium carbonate chemistry, but they have different structures.

All members of the calcite group are important minerals. Calcite's importance is beyond discussion since it is used in cements, steel industry, chemical industry, optical uses, etc. The

others in this group have their various uses, but all are used as ores for their respective metal content. Only otavite and gaspeite are considered rare.

Minerals belonging to the calcite group:

Calcite ( $\text{CaCO}_3$ )

Gaspeite ( $\{\text{Ni, Mg, Fe}\}\text{CO}_3$ )

Magnesite ( $\text{MgCO}_3$ )

Otavite ( $\text{CdCO}_3$ )

Rhodochrosite ( $\text{MnCO}_3$ )

Siderite ( $\text{FeCO}_3$ )

Smithsonite ( $\text{ZnCO}_3$ )

### 1.1. The mineral calcite

#### 1.1.1. General Information (Duda, 1990)

Origin: Named in 1845 after a Greek word, meaning to reduce to powder by heat (also Latin calx, burnt lime).

Chemical Formula:  $\text{CaCO}_3$

Composition:

Molecular Weight = 100.09 gm

Calcium 40.04 % Ca 56.03 % CaO

Carbon 12.00 % C 43.97 %  $\text{CO}_2$

Oxygen 47.96 % O

\_\_\_\_\_      \_\_\_\_\_  
100.00 %    100.00 % = TOTAL OXIDE

Environment: Found in sedimentary, igneous, and metamorphic rocks.

### 1.1.2. Crystallography (Roberts, 1990)

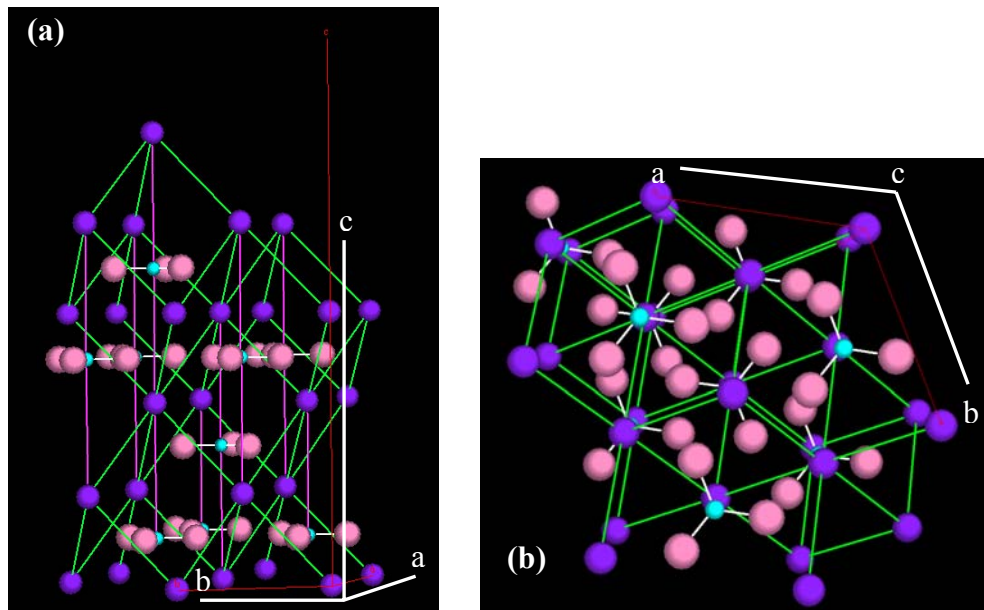


Figure 1: Atomic structure of calcite (a) c-axis lies in the plane of view and is at vertical position (b) c-axis is perpendicular to the plane of view.

Crystal System: Rhombohedral Scalenohedral H-M Symbol ( $\bar{3}2/m$ )

Space Group:  $R\bar{3}c$

Axial Ratios: a:c = 1:3.41992

Cell parameters: a=4.989, b=4.989, c=17.062

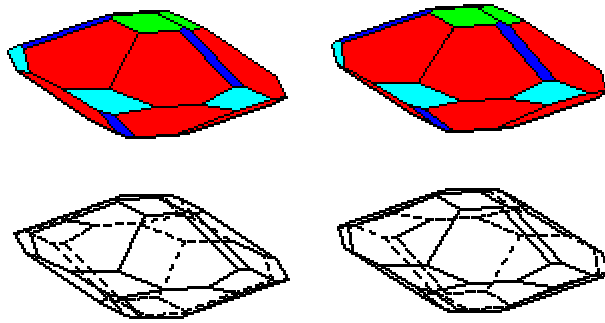
Z = 6 unit/cell; V = 367.78 Å<sup>3</sup>

	Wyckoff	X	Y	Z
Ca	6b	0	0	0
C	6a	0	0	0.25
O	18e	0.2593	0	0.25

System	Class Name	2-Fold Axes	3-Fold Axes	Planes	Centre	Hermann Maugin Symbols
Trigonal	Hexagonal Scalenohedral	3	1	3	yes	$\bar{3}2/m$

Forms:  $[2\ 1\ \bar{1}]$   $[0\ 1\ 1]$

Example of the Trigonal - scalenohedral class symmetry



**TRIGONAL**  
**Class =32/m**  
**Scale =1**  
**a = 1**  
**b = 1**  
**c = 1**  
**Scale step=1**  
**Cut step=10**  
**Rotation step=10**  
**[2 1 4]: 76%**  
**[1 0 4]: 73%**  
**[0 2 4]: 75%**  
**[1 0 0]: 30%**

### 1.1.3. Physical Properties (Roberts, 1990)

Cleavage: {1011} is perfect

Colour: colourless, white, pink, yellow, or brown.

Density: 2.71 g/cm<sup>3</sup>

Diaphaniety: Transparent to translucent to opaque

Fracture: Fracture is uneven. Brittle - Conchoidal - Very brittle fracture producing small, conchoidal fragments.

Habits: Crystalline - Coarse - Occurs as well-formed coarse-sized crystals., Stalactitic - Shaped like pendant columns as stalactites or stalagmites (e.g. calcite)., Massive - Uniformly indistinguishable crystals forming large mass

Hardness: 3 - Calcite

Luminescence: Fluorescent.

Luster: Vitreous (Glassy)

Streak: White

### 1.1.4. Optical Data (Roberts, 1990)

Uniaxial (-),  $e=1.486$ ,  $w=1.64-1.66$ , birefringence=0.1540-0.1740

### Other Information

Calcite is a most common mineral. It is one of the most common minerals on the face of the Earth, comprising about 4% by weight of the Earth's crust and is formed in many different geological environments. Calcite can form rocks of considerable mass and constitutes a significant part of all three major rock classification types. It forms oolitic, fossiliferous and massive limestones in sedimentary environments and even serves as the

cements for many sandstones and shales. Limestone becomes marble from the heat and pressure of metamorphic events.

The unique optical property of calcite, the birefringence occurs when a ray of light enters the crystal and, due to calcite's unique optical properties, is split into fast and slow beams. As the two beams exit the crystal they are bent at two different angles (known as angles of refraction) since the angle is affected by the speed of the beams. Watching through the crystal one sees the images splitted. There is only one direction in which the beams are of the same speed and that is parallel to the c-axis or primary trigonal axis. The direction perpendicular to the c-axis displays the greatest separation. The extremely high refraction index of calcite which causes the easily observable birefringence is also responsible for the interference colours (pastel rainbow colours) seen in calcites of small fractures.

Calcite is intricately tied to carbon dioxide. Many sea organisms such as corals, algae, diatoms and molluscs make their shells out of calcite, they pull carbon dioxide from the sea water. Environmentally then, calcite is very important and may have been quite important to the successful development of our planet in the past. By pulling carbon dioxide out of the sea water, this biological activity allows more of the air carbon dioxide to dissolve in the sea water and thus to act as a carbon dioxide filter for the planet.

A significant amount of calcite precipitate in sea water is undoubtedly inorganic, but the exact contributed amount is not well known. Calcite and other carbonate minerals are very important minerals in the ocean ecosystems of the world.

Calcite is not the only calcium carbonate mineral. There are three minerals or phases of  $\text{CaCO}_3$ . Aragonite and vaterite are polymorphs with calcite, meaning they have the same chemistry but different crystal structures and symmetries. Aragonite is orthorhombic, vaterite is hexagonal and calcite is trigonal. Aragonite is a common mineral, but is vastly out distanced by calcite which is the more stable mineral at widest range of temperature and pressure values. Vaterite on the other hand is extremely scarce and rarely seen. Aragonite will at ambient conditions over time convert to calcite and calcite pseudomorphs after aragonite are not uncommon.

## **2. The Aragonite Group of Minerals**

Aragonite minerals are carbonate minerals that have an orthorhombic symmetry;  $2/m\ 2/m\ 2/m$ , and the formula  $ACO_3$  where A can be calcium, barium, lead and/or strontium.

The structure of the Aragonite Group minerals is composed of triangular carbonate ion groups ( $CO_3$ ), with a carbon at the centre of the triangle and the three oxygens at each corner. Unlike the Calcite Group the carbonate ions do not lie in a single plane pointing in the same direction. Instead they lie in two planes pointing in opposite directions; destroying the trigonal symmetry that is characteristic of the Calcite Group. To illustrate this, imagine the symmetry of an equilateral triangle; a three fold rotation with three mirror planes that cross in the centre. Now join two of these triangles together at their bases and you have a diamond-shaped figure with the symmetry of a two fold rotation with one mirror plane in the middle. This is the effect of the two carbonate planes with opposite orientations on the symmetry of this structure. The metal ions on the other hand, are arranged in what is called hexagonal closest packing. It is responsible for this groups pseudo-hexagonal tendencies. The aragonite structure is responsible for the similar properties in these minerals. Dissimilar properties are then the responsibility or the result of the differing metal cations.

The Aragonite Group minerals are relatively common, with the exception of witherite. Aragonite is valuable in cements and in other uses. The other members of this group are used as minor ores of their respective metal components.

### **Minerals belonging to the aragonite group**

Aragonite ( $CaCO_3$ )

Cerussite ( $PbCO_3$ )

Strontianite ( $SrCO_3$ )

Witherite ( $BaCO_3$ )

### **2.1. The mineral aragonite**

#### **2.1.1. General Information** (Duda, 1990)

Origin: Named in 1790 after the original locality in Aragon, Spain.

Chemical Formula:  $CaCO_3$

Composition:

Molecular Weight = 100.09 gm

Calcium	40.04 % Ca	56.03 % CaO
Carbon	12.00 % C	43.97 % CO <sub>2</sub>
Oxygen	47.96 % O	
	100.00 %	100.00 % = TOTAL OXIDE

### 2.1.1. Crystallography (Roberts, 1990)

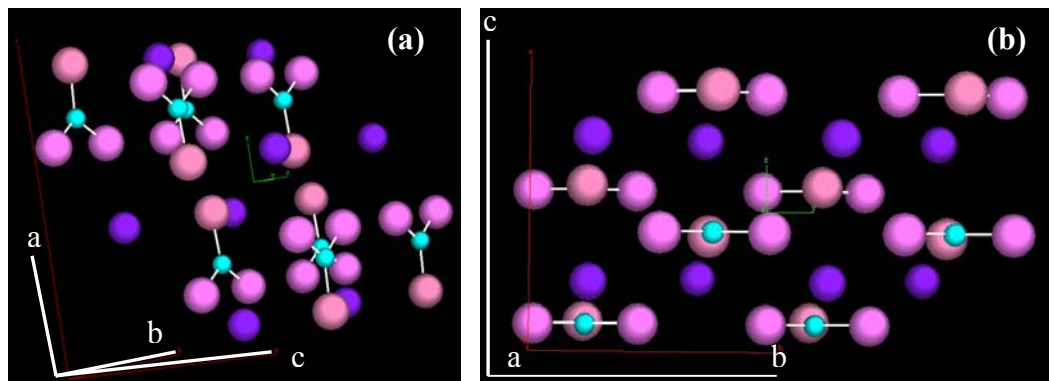


Figure 2: Atomic structure of aragonite (a) a-axis lies almost vertical in the plane of view and c-axis lies almost horizontal, (b) a-axis is perpendicular to the plane of view and c-axis is at vertical position.

Axial Ratios: a:b:c = 0.6223:1:0.7205

Cell parameters: a=4.9614, b=7.9671, c= 5.7404

Z = 4 unit/cell, V = 226.85 Å<sup>3</sup>

	Wyckoff	X	Y	Z
Ca	4c	0.25	0.41508	0.24046
C	4c	0.25	0.76211	0.08518
O(1)	4c	0.25	0.92224	0.09557
O(2)	8d	0.47347	0.68065	0.08726

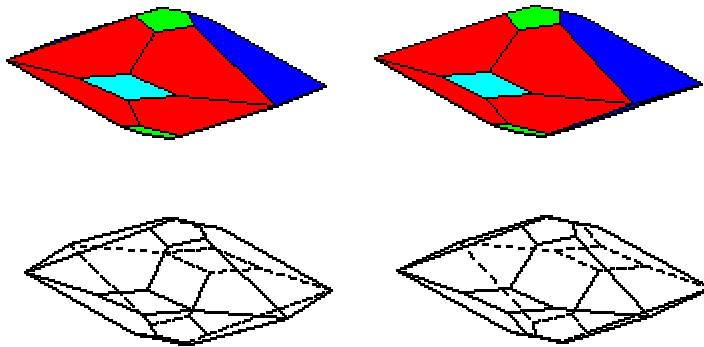
Crystal System: Orthorhombic - Dipyramidal H-M Symbol (2/m 2/m 2/m)

Space Group: Pmcn

System	Class Name	2-Fold Axes	Planes	Centre	Hermann Maugin Symbols
Orthorhombic	Dipyramida	3	3	yes	2/m 2/m 2/m

Forms: [0 0 1] [0 -1 -1] [0 1 0] [1 1 0]

Example of the Orthorhombic dipyramidal class symmetry:



**ORTHORHOMBIC**  
 Class =  $2/m2/m2/m$   
 Scale = 1  
 a = 1  
 b = 1  
 c = 1  
 Scale step = 1  
 Cut step = 10  
 Rotation step = 10  
 [2 1 4]: 76%  
 [1 0 4]: 73%  
 [0 2 4]: 75%  
 [1 0 0]: 30%

### 2.1.2. Physical Properties (Roberts, 1990)

- Cleavage: {010} is distinct and {110} is indistinct
- Colour: colourless, white, gray, yellowish white, or reddish white.
- Density: 2.93 g/cm<sup>3</sup>
- Diaphaniety: Transparent to translucent
- Fracture: Sub Conchoidal - Fractures developed in brittle materials characterized by semi-curving surfaces.
- Habits: Pseudo Hexagonal - Crystals show a hexagonal outline., Columnar - Forms columns, Fibrous - Crystals made up of fibers.
- Hardness: 3.5-4
- Luminescence: None
- Luster: Vitreous (Glassy)
- Streak: White

### 2.1.3. Optical Data: (Heinrich, 1965)

Biaxial (-), a=1.529-1.53, b=1.68-1.682, birefringence=0.1560, 2V(Calc)=16-18°, 2V(Meas)=18-19°. Dispersion weak, r < v.

### Other Information

Aragonite is technically unstable at normal surface temperature and pressure. It is stable at higher pressure, but not at higher temperature, therefore in order to keep aragonite stable with increasing temperature, the pressure must also increase. If aragonite is heated to 400 degrees C, it will spontaneously convert to calcite if the pressure is not increased as well. Under certain conditions of formation, the crystallization of calcite is somehow discouraged and aragonite will form instead. The magnesium and salt content of the crystallizing fluid, the turbidity of the fluid and the time of crystallization are decidedly important factors, but perhaps there are others as well. Biomineralization allows significant amounts of aragonite to form. Also metamorphism that includes high pressures and (relatively) low temperatures can form aragonite. After burial, given enough time, the aragonite almost certainly alters to calcite.

Aragonite's most common crystal habit is to produce the twinned pseudo-hexagonal prismatic crystals. Twinning is the result of a fault during the growth of the crystal. It occurs when the atomic layer stacking, in a sequence such as ABCABCABCABCABC etc, makes a mistake and a C layer instead of a B layer is placed next to an A layer. The result is an ABCABCABCACBACBACBA stacking sequence. Where the mistake occurs, a mirror plane is produced that was not there before. This has the effect of increasing the apparent symmetry of the crystal. The error in aragonite's structure causes a bend in the crystal of exactly 120 degrees. If three bends or twins occur, then a 360 degree crystal, called a cyclic twin or trilling, can form. In this case, aragonite can appear hexagonal (six sided). These crystals can be thought of as a "triple twin" where one crystal takes up one third (or 120 degrees) of a hexagon.

## **Chapter III. The structure of the shell of *Patella crenata***

### **1. Collection and sampling of *Patella crenata* shells**

The docoglossan archaeogastropod *Patella crenata* was collected from the Canary Island where the molluscs live on the rocky shore. To study the structure, composition as well as elemental ratios and distribution, samples were made by perpendicular slicing of the shells into pieces of width 2 mm and by consequent cross section and lateral section processing (lapping and mechanical polishing). The individual shell has a convex shape and radially arranged ribs.



Figure 3: *Patella crenata* shell at two sites. (1) Calcitic crossed lamellar structure, (2) Aragonitic myostracum, and (3) Aragonitic hypostracum, the inner crossed lamellar structure.

Figure 3 shows the inner site (at the left) and the outer site (at the right) of the shell of *Patella crenata*. For our analyses, the principal directions within the shell were determined by an optical microscope. We decided to use the following macroscopic sample reference frame for texture descriptions:

**G** is the growth direction, perpendicular to the margin of the shell (Fig. 3), beside this growth direction there is also one direction of growth, which is perpendicular to the inner surface of the shell parallel to **N**.

**N** is the normal of the plane tangent to the shell surface.

**M** is the direction of the layers.

## **2. Shape, mesoscopic structure and development of the shell**

The morphological characteristics of *Patella crenata* were previously studied by Bandel and Geldmacher (1996). Major topological features of such complex structured molluscs can be summarized as follows. The cap-like shell is convex in frontal and lateral view and its apex is usually corroded (Fig. 3). The ornament consists of radial ribs with a prominent rib usually accompanied by two less prominent ones. In individuals that lived in a calmer environment there are more main and minor ribs than in those that have grown in more turbulent water. The shell margin is wavy reflecting the end of main and minor ribs on the apertural lip. The outside near the margin is the only place where a thin brown periostracum (Fig. 3, region 4) is preserved, while further back it is usually corroded and worn off.

In the inner shell surface of *Patella crenata* there are several layers that may be distinguished on the basis of luster, colour, and shape. The layer closest to the margin is composed of the outer calcitic crossed lamellar structure (Fig. 3, region 1) and represents the largest portion of the shell. It has shiny luster and light to dark bluish colouration. Towards the centre of the inner shell surface a dark, grayish-blue band follows which represents the prismatic myostracum (Fig. 3, region 2). Only here was the soft body of the limpet attached to its shell, forming a horseshoe-shaped scar that is thickened at both ends, representing the area above the head. The prismatic layer of the myostracum forms a row of scars of variable number up to fourteen. The ring muscle connecting shell and animal with each other was, thus, organized into about 14 bundles of muscle fibres. The prismatic myostracum is surrounded by a light gray ring that becomes wider in the frontal area and represents the spherulitic myostracum.

The central portion of the inner shell of *Patella crenata* is covered by a porcelain - grey to yellow shiny layer of the mainly aragonitic hypostracum (Fig. 3, region 3). In the posterior shell portion the hypostracal layer lies approximately parallel to the outer shell margin. In the frontal region above the head it forms two sinuses. Within the hypostracal layers fully grown shells have more or less extensive zones with a vitreous luster and yellow to brown

colouration. These are not organized according to the symmetry of the shell and consist of calcite (calcitic hypostracum).

#### Calcitic crossed lamellar layer

The outer calcitic crossed lamellar layer (Fig.3, region 1) is situated between the periostracum (Fig. 3, region 4) on the outside and the myostracum (Fig.3, region 2) formed at the tissue shell attachment zone on the inner side. It consists only of calcite with the structure composed of piles of thin leaves approximately parallel to each other and arranged concentrically. Within these lamellae of the first order thinner sheets are the lamellae of the second order which are then composed of lamellae of the third order. Orientation of the lamellae of the first order is such that they form an angle of about  $150^\circ$  with the interior of the shell. Lamellae of the second order, in contrast, form an angle of about  $15^\circ$  with the inner shell surface. The height of the lamella of the first order represents the shell thickness and can reach up to 3 mm. Its width, which is also the width of the lamellae of the second order, is about 40  $\mu\text{m}$  while its length is several mm when measured on the inner side of the shell. Lamellae of the second order are parallel to each other formed by narrow and elongated crystallite-like but structurally non-heterogeneous particles representing the lamellae of the third order. These are about 0.6  $\mu\text{m}$  wide, about 0.2  $\mu\text{m}$  high, and as long as the lamellae of the second order. They are usually arranged side by side. They may, however, also be arranged like tiles in a corrugated roof pattern. This structure is transected by fine growth increments. Lamellae of the third order in their outcrop on the inner shell surface form a radial oriented zigzag pattern with corners forming an angle of  $119^\circ$ .

On the surface of the shell collabral growth lines coincide with the lamellae of the first order. Thus, concentric growth lines represent lamellae of the first order. The sculpture of the growth lines consists of the heads of the lamellae of the second order. The orientation of the lamellae of the first order depends on the shape of the shell edge. After secretion of the first mineral layer within and below the organic layer of the periostracum the shell growth continues further away from the shell margin. Here external particles like grains of sand may become cemented which causes only minor confusion of the crossed lamellar pattern. Within the muscle attachment area such inclusions of foreign particles are rare, and behind this zone they occur exceptionally.

The number of lamellae of first order decreases from the shell surface to shell interior. Also their width differs with ontogeny. Second order lamellae in juvenile shells measure

approximately 22  $\mu\text{m}$ , and they are 35 microns wide in fully grown individuals. Increase in width of lamellae of the first and second order is accomplished by more and more elements of the third order added to them. Growing lamellae of the second order seen on the inner side of the shell are not homogeneous. Here every element of the third order ends as a rhombic rod and grows by periodic additions.

#### *Aragonitic Myostracum*

The deposits of the muscle scar form a circular band that succeeds the outer calcitic crossed lamellar layer in the inward direction (Fig. 3, region 2). Here the mantle is attached to the shell just below the onset of the ring-shaped ribbon of the retractor muscle. The myostracum consists exclusively of aragonite and is of variable thickness. Fully grown individuals have a 90 to 230  $\mu\text{m}$  thick layer, but in juvenile shells this layer may only be as thin as 4  $\mu\text{m}$ . Large shells with 7 cm length in radial section reveal up to three concentrically oriented zones of greater thickness of the myostracal layer. Most probably these zones reflect stunting in growth of the shell, and thicker portions of the myostracal layer represent slowed shell formation during winter.

The myostracal layers of the fully grown shell are subdivided in two structurally differentiated sections. The first is that layer which succeeds the calcitic crossed lamellar layer on the outside and consists of spherulite sectors, and the second develops from it and is composed of a prismatic structure. The layer of spherulite sectors consists of fine needles arranged in an inclined way around a common axis. The needles with the same angle of inclination are united within cones with circular or elliptical bases and orientation vertical to the shell surface. Fully grown spherulite sectors are about 20  $\mu\text{m}$  high, and the angle of the cone opening is about  $108^\circ$  and, their base rests immediately on the crystallite heads of the lamellae of the second order of the calcitic crossed lamellar layer.

On top of the spherulite sector layer a prismatic layer appears by a change of growth of the needle-like crystallites into vertical orientation. The transition from one to the other occurs without interruption. With continued growth these needle-prisms increase in diameter, and their acute triangular shape changes into a more massive columnar, rectangular, to almost quadrate shape.

Aragonitic crossed lamellar layer

The inner aragonitic crossed lamellar structure (Fig. 3, region 3) is formed below the apex of the shell and the interior of the attachment between tissue and shell. Here the predominantly aragonitic hypostracum (“callus”) is present with fine lines oriented almost radially to the plane of symmetry of the shell near the head of the animal, and oriented concentrically in the posterior part of the shell. These fine lines represent lamellae of the first order. The lamellae of the second order compose lamellae of the first order and show two patterns. The one that runs parallel to the margins corresponds to lamellae of the third order that are 0.24  $\mu\text{m}$  wide. The other consists of dark perpendicular stripes which are oriented parallel to the inner shell surface and represent growth increments with distance of about 0.9 to 2.8  $\mu\text{m}$ . They occur because of varying amount of organic material contained within the mineral shell. Lamellae of the third order in neighboring lamellae of the first order form an angle of about  $109^\circ$  with each other and form an angle of about  $35^\circ$  with the surface of the shell interior

The crossed lamellar structure is like that commonly found among molluscs and in most gastropods (Bandel, 1990). A comparison of the aragonitic with the calcitic crossed lamellar structure shows two major differences besides crystallographic modifications of the calcium carbonate. The angle formed between neighboring lamellae of the second order in the aragonitic layer is about  $109^\circ$  and, thus, almost rectangular, while that of the calcitic crossed lamellar layer follows a rhomboidal pattern and is about  $149^\circ$ . In addition, lamellae of the first order in the aragonitic crossed lamellar structure split and bifurcate much more commonly than in the calcitic crossed lamellar structure.

In *Patella crenata* the aragonitic crossed lamellar layers often contain prismatic intercalations with a high content of organic material which are absent in the calcitic crossed lamellar structure. The diameter of the aragonitic prisms is usually around 0.27  $\mu\text{m}$ . The length of the prisms and, thus, the thickness of a prismatic layer varies considerably. In juvenile individuals the average thickness is 2.2  $\mu\text{m}$  while fully grown individuals have about 6  $\mu\text{m}$  thick interlayers. Transition into prismatic arrangement of the needles lamellae of the third order occurs without break forming an angle of  $129^\circ$  with each other. The organic components of the prismatic layers within the crossed lamellar structure also dissolve when the mineral part is dissolved. This differs from the prismatic layers of the myostracum indicating a higher content of organic material and a different composition of that material in

the latter. Here the fibres of the mantle attachment to the shell have become integrated between the aragonitic crystallites.

In the shell of adult animals calcitic hypostracal layers are deposited within the callus. They form areas of irregular outline that may cover an area up to 2 x 3 cm with a deposit that is up to 0.5 cm thick. As in the aragonitic crossed lamellar deposits right next to them these calcitic layers contain prismatic intercalations. Therein lamellae of the second order are almost parallel to the inner shell surface and are either flat or have an undulating surface. Undulation is caused by alternating inclination of elements of the third order. Elements of the second and third order resemble closely those of the outer calcitic crossed lamellar layer. The width of elements of the third order has an average of 0.64  $\mu\text{m}$  also resembling those of the outer shell layer that have an average of 0.61  $\mu\text{m}$ .

The calcitic portions of the interior callus are not homogeneous in construction, but show spindle shaped or plait-like inclusions composed of fine needle-like spherulite sectors with an apical angle of 70° to 105°. Increments of growth continue across the border between prismatic layers and these inclusions without interruption being arranged vertical to the plait or spindle-cones and parallel to the growth surface.

Calcitic and aragonitic deposits were produced at the same time, side by side with the spherulite sectors within the calcitic layer. Most of the callus or hypostracal deposits of *Patella crenata* is formed by the aragonitic crossed lamellar structure with prismatic aragonitic intercalations, and it is within this aragonitic callus of older individuals of the gastropod that the flat sheets of calcitic construction are deposited.

## Chapter IV: Polarized Light Microscopy (PLM)

### 1. Introduction

The polarized light microscope is designed to observe and photograph specimens that are visible due to their optically anisotropic character. In order to accomplish this task, the microscope must be equipped with both a polarizer, positioned in the light path somewhere before the specimen, and an analyzer (a second polarizer), placed in the optical pathway between the objective rear aperture and the observation tubes or camera port

In anisotropic crystalline materials, light splits into two beams that travel in different directions at different speeds (birefringence). The beams of light are polarized at right angles to each other. If calcite is observed through a polarizing filter, the doubled images blink in and out as the polarizer rotates, confirming that the two images are due to light polarized in perpendicular directions. These directions are called the *privileged directions*. The two beams travelling at slightly different speeds have slightly different refraction indices. Usually the variation is only a few per cent.

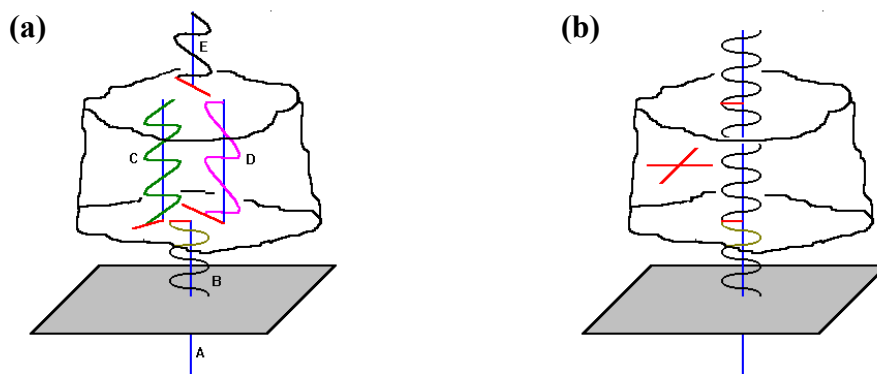


Figure 4: **(a)** Unpolarized light (A) is polarized passing through polarizer (B). When it enters a crystalline material, it splits into two rays: *slow* (C: higher refractive index ( $n_2$ )) and *fast* (D: lower refractive index ( $n_1$ )). When the two rays exit the crystal (E) they recombine into a single one. Their electric field vectors interact and the resulting beam usually has a different orientation than the incident one. **(b)** If a second analyzer is placed above the material perpendicular to the first one, some of the exiting light passes through it, and the material is not black as in the case of two crossed polarizers.

When a privileged direction of the mineral is parallel to the bottom polarizer, the light splits into two components of perpendicular polarizations. The component perpendicular to the incident polarized light is zero. The exiting light has the polarization of the incident light, and is blocked by the upper polarizer.

As the anisotropic specimen is rotated over a range of 360 degrees on a circular microscope stage, it displays a privileged direction parallel to the bottom polarizer at every 90 degrees. No light passes through the upper polarizer and the specimen appears black (extinction).

When the specimen's long axis ( $n_2$ ) is oriented at 45-degree to the polarizer axis, the maximum brightness is achieved, and when the two axes coincide the maximum extinction is observed. During rotation over a range of 360 degrees specimen visibility oscillates four times between bright and dark in 90-degree increments. If the specimen orientation is altered by 45 degrees, incident light is split by the specimen into ordinary and extraordinary components and then united in the analyzer to yield interference patterns.

## **2. Polarized Light Microscope equipment**

Polarized (and brightfield) microscope type Olympus BX61 was used in this study. Polarized light microscope has a lamphouse, which contains a 50 to 100-watt high-energy tungsten-halogen lamp, attached to the base of the microscope. The microscope is equipped with a slot in the body tube above the nosepiece and between the polarizer and analyzer. The purpose of this slot is to house an accessory or retardation plate in a specific orientation with respect to the polarizer and analyzer vibration directions. The slot is oriented with its long axis directed Southeast-Northwest as observed from the eyepieces.

Polarization colours result from the interference of the two components of light splitted by the anisotropic specimen (and may be regarded as white light minus those colours that are interfering destructively). The two components of light travel at different speeds through the specimen and have different refractive indices, or refringences. Birefringence is the numerical difference between these refringences. The analyzer recombines only components of the two beams travelling in the same direction and vibrating in the same plane. The polarizer ensures that the two beams have the same amplitude at the time of recombination for maximum contrast.

### 3. Results and Discussion

Using the optical microscope we have studied the morphology and the optical properties of the investigated *Patella crenata* shell. The used method of polarized light produces enhanced contrast of studied thin cross-section which has anisotropic refractive properties. We use a gypsum retardation plate with optical path length difference 530 nm, which gives instead of black a purple background, i.e. the extinction is at purple colour. Whenever the specimen is in extinction, the permitted vibration directions of light passing through are parallel with those of either the polarizer or the analyzer.

A thin cross section (Fig. 5) and lateral section (Fig.10) specimens are illuminated by polarized light. Contrast of the transmitted light is obtained between sample features that have different optical properties. (Fig. 5 and Fig. 10).

Polarized light investigations show different types of crossed lamellar structures, namely calcitic and aragonitic material separated by the aragonitic myostracum. According to Bandel and Geldmacher (1996) the crossed lamellar structure of both materials is organized in first, second, and third order lamellae which build each layer respectively. The smallest components of the pattern are the elements of the third order.

#### 3.1. Cross section of *Patella crenata*

A thin cross section (Fig. 5) shows that neighbouring calcitic lamellae have different orientation. The directions showing the position of the shell layers in that thin cut are denoted by **M** (see Fig. 3), which is perpendicular to the observation plane of the thin section, **N** - normal to the tangent plane to the shell surface and **G** – indicates the growth direction and the margin of the shell.

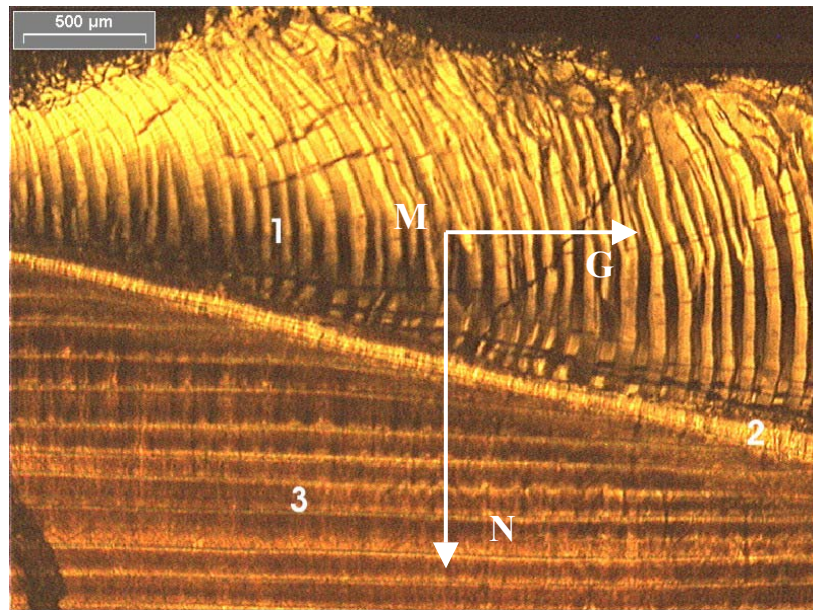


Figure 5: Polarizing microscope image of a thin section of the *Patella crenata* shell (thin section is vertical to the shell surface): (1) Calcitic crossed lamellae, (2) Aragonitic myostracum, and (3) Aragonitic hypostracum, the inner crossed lamellae.

Figure 5, region 1 shows that the ends of the calcitic lamellae are preferentially turned to the left or in the direction of the shell apex. From the different colours within the calcitic lamellae one can conclude, that their building particles are of different orientation along the width of the lamellae (direction N). The aragonitic myostracum (Fig. 5, region 2) appears like a bright strip diagonal through the thin section separating the calcitic and aragonitic crossed lamellae. The third part of the thin cut (Fig. 5, region 3) is the aragonitic crossed lamellar structure. Here we can observe bright lines parallel to the shell surface and to each other.

### 3.2. Lateral section of *Patella crenata*

Figure 6 shows the arrangement of the lamellar structure similar to the indicated in Figure 5. At that lateral section one can observe very clearly the spherulitic character of the aragonitic myostracum (Fig. 6, region 2) that separate the aragonitic and calcitic cross lamellar structure.

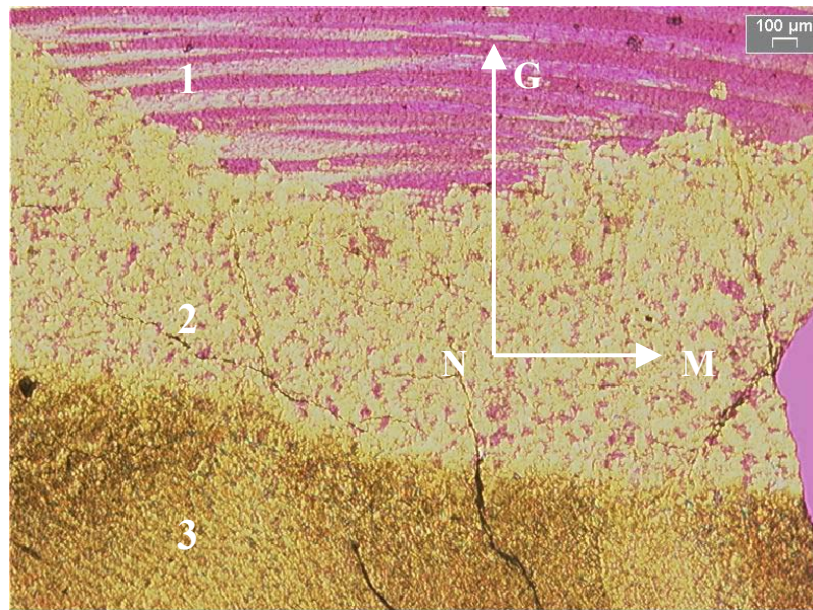
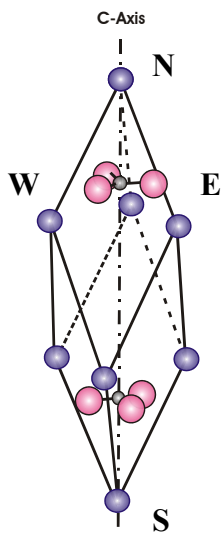


Figure 6: Polarizing microscope image of a thin section of the *Patella crenata* shell (thin section is parallel (lateral) to the shell surface): (1) calcitic crossed lamellar structure, (2) aragonitic myostracum, and (3) aragonitic hypostracum, the inner crossed lamellar structure.

Calcite optical characteristics: (Phillips, 1971)



The crystal structure of calcite is analogous to the simple structure of halite (NaCl), in which  $\text{Ca}^{2+}$  and  $\text{CO}_3^{2-}$  ions replace the alternate  $\text{Na}^+$  and  $\text{Cl}^-$  ions. The carbonate ions are arranged perpendicular to one cube diagonal, which becomes the unique or crystallographic  $c$ -axis, and the cubic cell becomes a rhombohedral. The carbonate ion consists of one small carbon atom surrounded by three oxygen atoms that form the corners of an equilateral triangle. They are held tightly together by strong, largely covalent bonds that are much stronger than any external bond and are highly polarized in the plane of the ion

Crystals showing only one unique crystallographic direction (i.e., tetragonal, trigonal and hexagonal) have only one optical axis (always parallel to the  $c$ -crystallographic axis), and are uniaxial. Thus for uniaxial crystals, like calcite, the relationship between optical and crystallographic directions is well defined. Cleavage planes and crystal faces represent other crystallographic directions that bear some symmetric relation to the optical axis.

A simple quantitative measure of this relationship is the extinction angle, or the angle between inherent vibration direction and an observed crystal face or cleavage plane. Crystal faces and cleavages are limited to basal, prismatic, and pyramidal types in tetragonal, hexagonal and trigonal crystals.

Basal pinacoids and basal cleavages define planes parallel to the optical axis. Reference to the indicatrix shows that when the trace of any of these planes lines either N-S or E-W, the crystal must show extinction with crossed nicols in which case the crystal shows parallel extinction to the cleavage or crystal face.

Pyramidal crystal faces and cleavage planes are inclined to the optic axis and lie at some angle to N-S and E-W cross hairs when the crystal is rotated to extinction between crossed nicols. Symmetry requires pyramidal planes to occur in symmetrically equivalent sets of three, four, six, eight, or twelve such that each plane shows an identical relationship to the *c*-axis. Two or more of these planes or sets of planes should be visible in any section; the crystal extinguishes when the N-S and E-W cross hairs bisect the angle of intersecting pyramidal planes, showing symmetrical extinction. The extinction angle, measured to one pyramidal plane, is equal and opposite in sign to the extinction angle, measured to the neighbouring.

In summary, uniaxial crystals show parallel extinction with respect to basal and prismatic planes and symmetrical extinction with respect to pyramidal planes.

### 3.3. Calcitic crossed lamella

#### 3.3.1. Crossed section

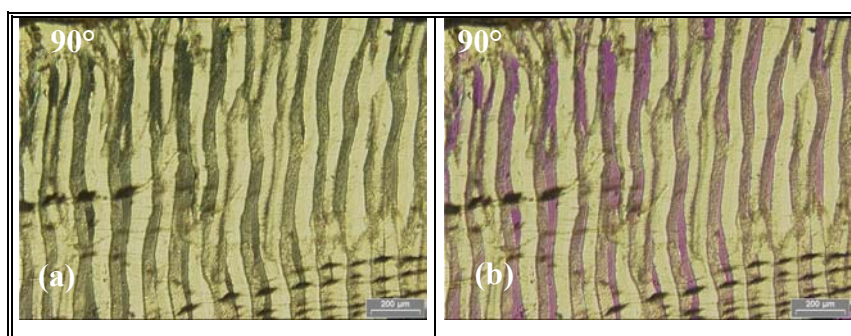


Figure 7: Polarizing microscope images of calcitic cross lamellar structure for *Patella crenata* orientation at  $90^\circ$  to the observation plane: (a) without retardation plate; (b) with retardation plate. The magnification is 10x.

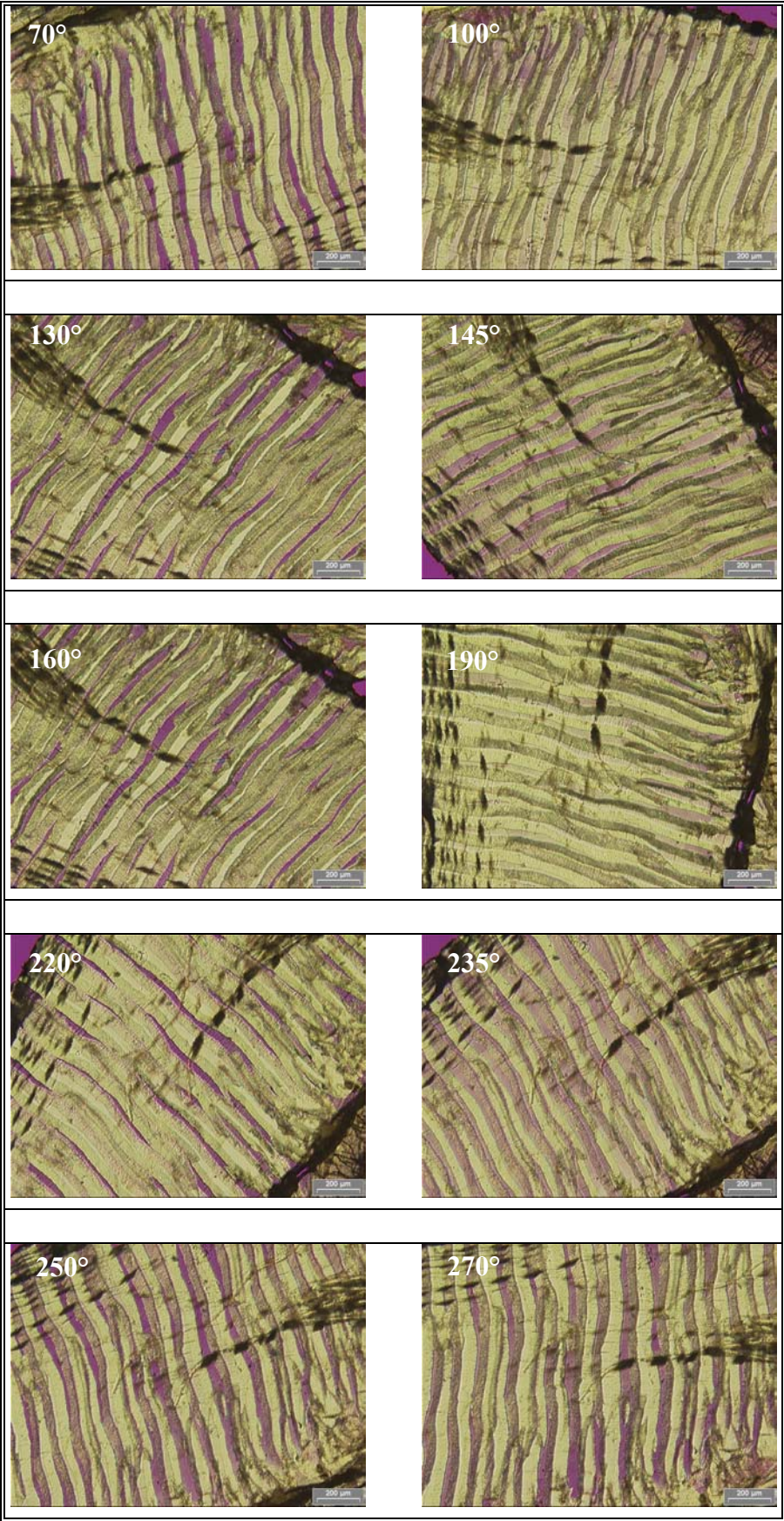


Figure 8: Polarizing microscope images of calcitic cross lamellar structure for *Patella crenata* orientation at various angles to the observation plane. The magnification is 10x.

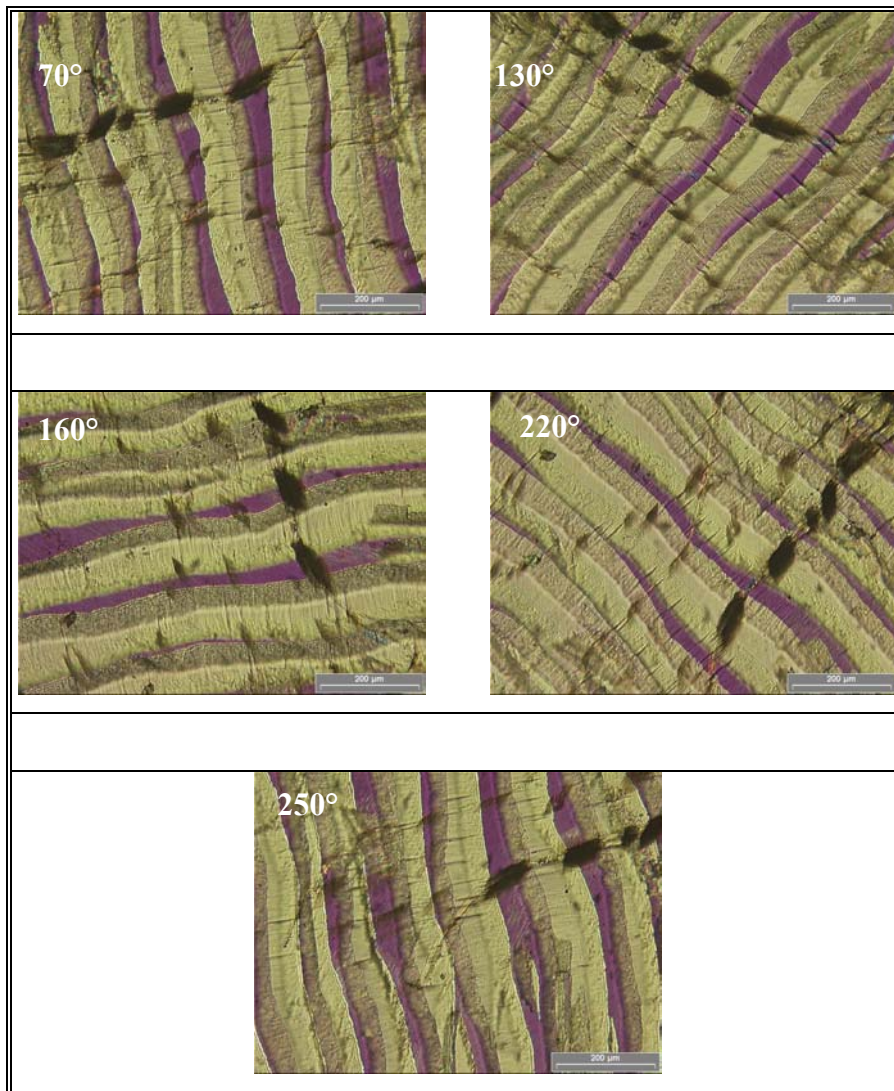


Figure 9: The same as figure 8. The magnification is 20x

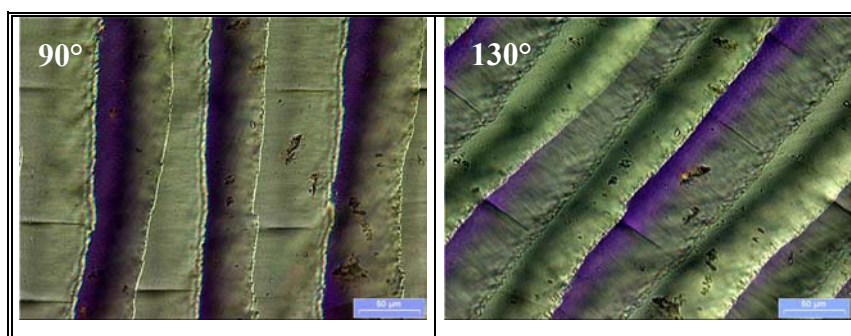


Figure 10: The same as figure 8. The magnification is 50x

The higher magnification in Figure 10 allows to estimate the lamellae at their 3D form. It is seen how the extinction changes from one lamella to another.

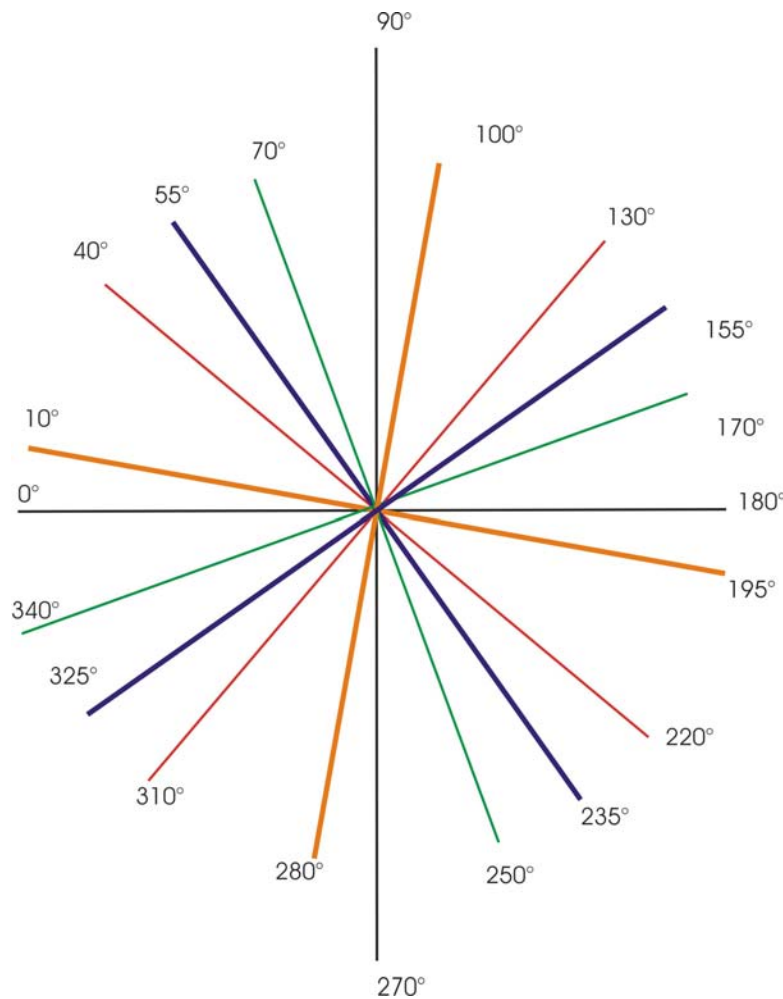


Figure 11: Schematic graph of rotation over a range of 360 degrees of the cross section of *Patella crenata*. The green and red lines are the maximum brightness for one of two neighbouring lamellae. Orange lines mark the bright maxima of all lamellae and the blue lines mark the extinction of all lamellae.

Figure 11 shows the extinctions and maxima of all calcitic lamellae of first order. The maxima of lamellae with one orientation are accompanied by extinctions of their neighbouring lamellae with another orientation.

The extinction of all calcitic lamellae shows that the *c*-axis is parallel to the axis of either the polarizer or the analyzer, i.e. they display parallel extinction. Extinction of all lamellae is observed at 55° and 235° where the *c*-axis is parallel to the polarizer (i.e. to the abscise), and at 145° and 325° where the *c*-axis is parallel to the analyser (i.e. to the ordinate). The maxima for all lamellae are at 10°-190° and 100°-280° respectively. At that position the *c*-axis is oriented at a 45° angle to the polarizer axis.

There are also two symmetrical extinctions of the pyramidal planes. The first one occurs in a lamella at 40°/220° and 130°/310°, while the neighbouring lamella displays a

maximum. The second symmetrical extinction occurs in the neighbouring lamella at  $70^\circ/250^\circ$  and  $160^\circ/340^\circ$ . Hence, two pyramidal planes are mutually oriented at an  $30^\circ$  angle. The angle between the  $c$ -axis and the symmetrical extinction of either neighbouring lamella is about  $15^\circ$ .

### 3.3.2. Lateral section

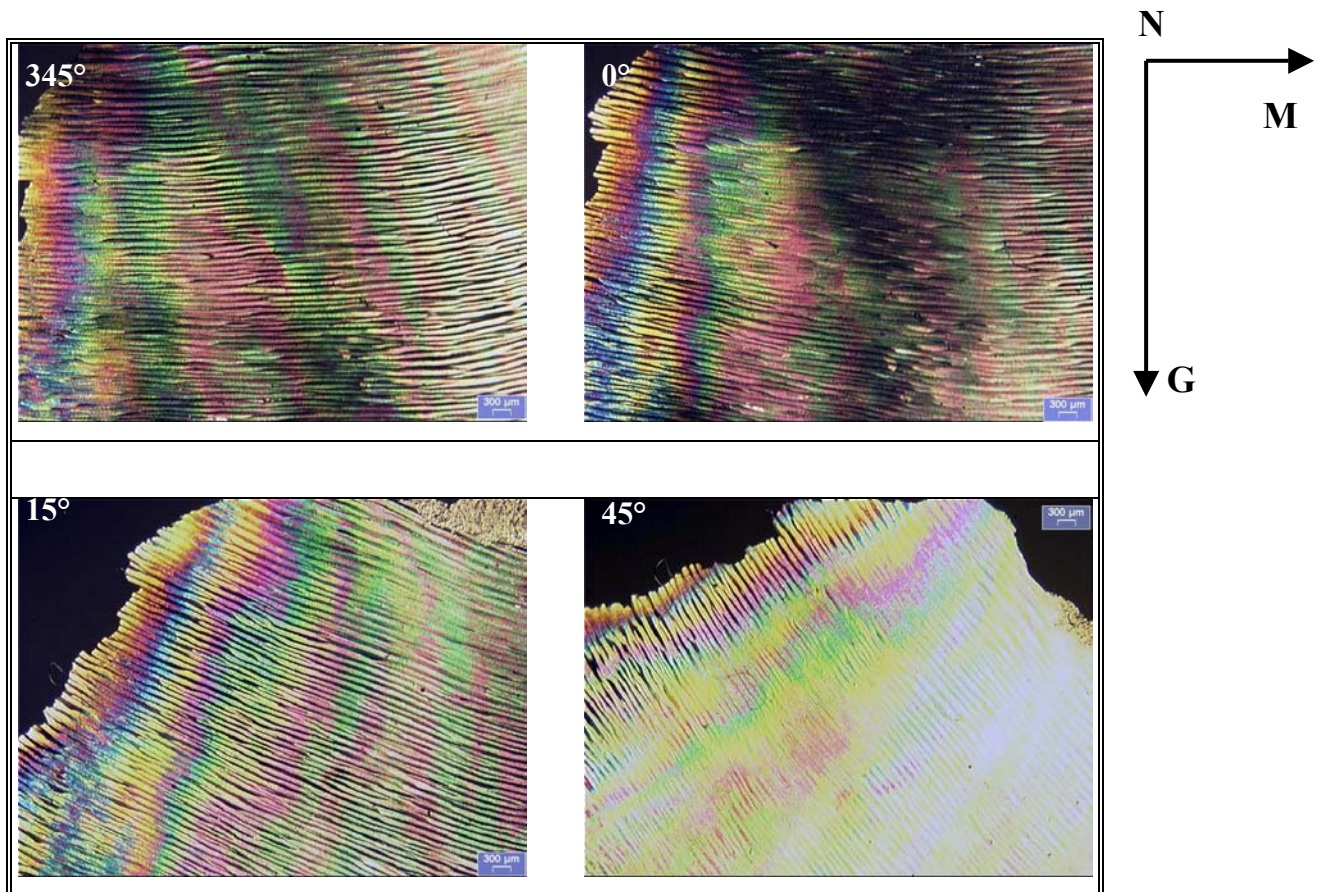


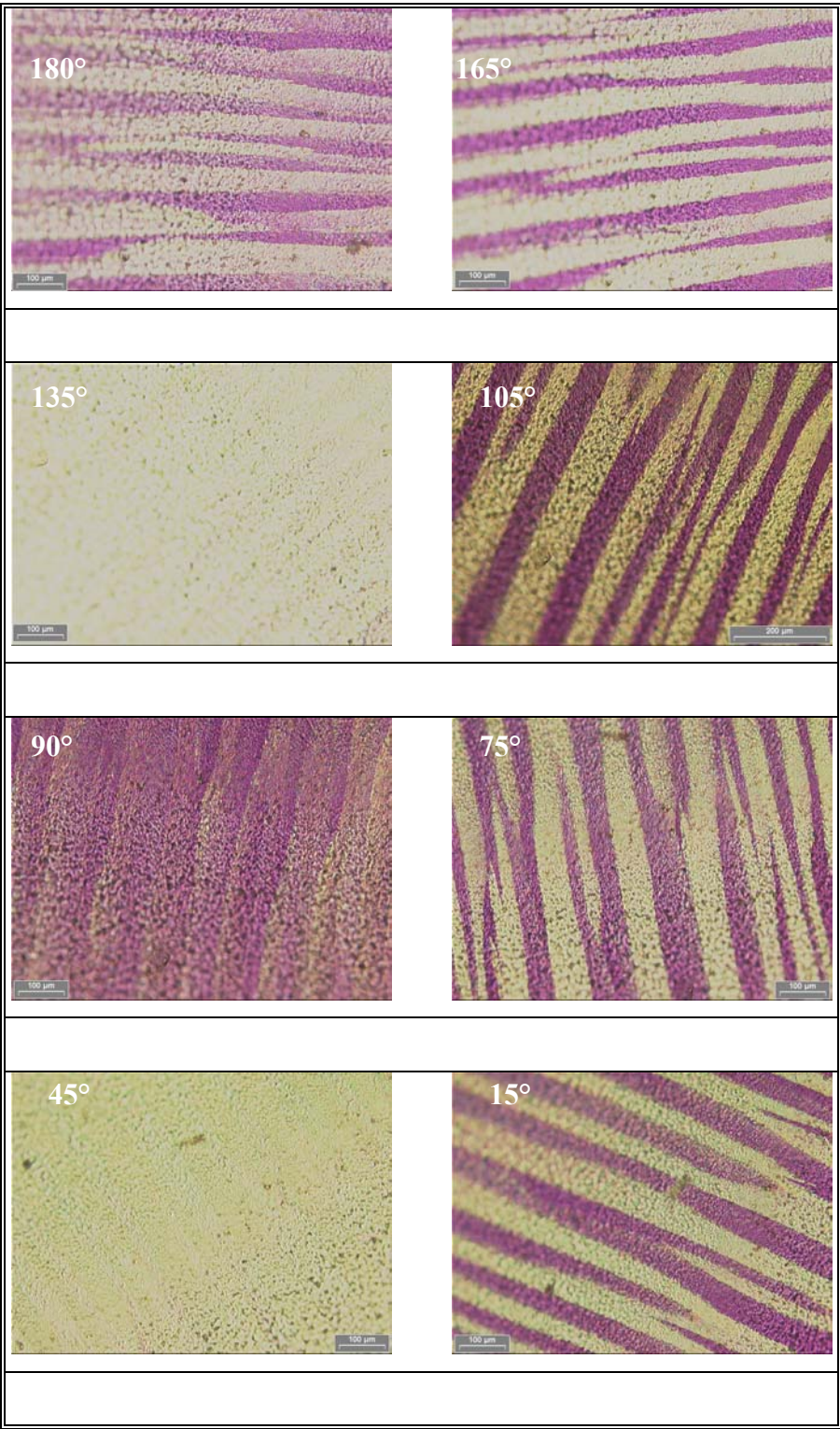
Figure 12: Polarizing microscope images of calcitic cross lamellar structure for specimen orientation at various angles to the observation plane. The magnification is 2x

In figure 12 the interference colour sequence from the calcitic material is observed. Each colour results from a specific retardation, indicated in nanometers [nm]. We know the thickness of the thin cut ( $d = 35 \mu\text{m}$ ) and the birefringence value ( $n_1 - n_2 = 0.172$ ), which are needed to determine the retardation ( $\Delta$ ) (interference colour) under crossed polarizers.

$$\Delta = d(n_1 - n_2),$$

where  $n_2$  is the higher refractive index and  $n_1$  is the lower refractive index. Hence, for the first figure on the left side of Fig. 12 the average retardation  $\Delta$  is 602 nm.

Composed crystallites of varying size and orientation do not allow to estimate the birefringence precisely.



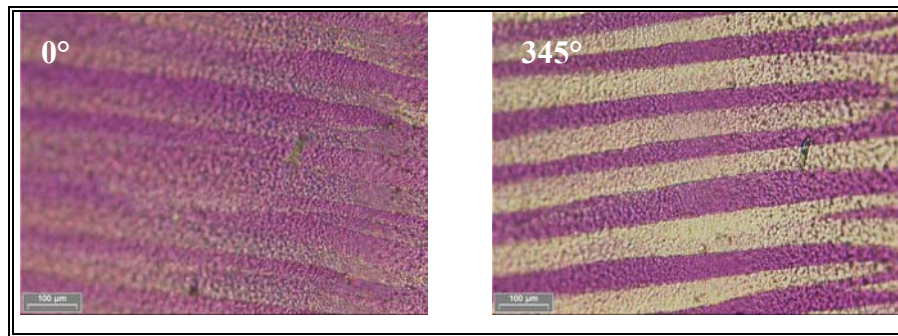


Figure 13: The same as figure 12. The magnification is 20x

Figure 13 shows extinctions and maxima of all calcitic lamellae of first order in the lateral section. The maxima of lamellae with one orientation are accompanied by extinctions of their neighbouring lamellae with another orientation.

#### 3.4. Aragonitic crossed lamellae.

Figure 14 shows the arrangement of lamellae of second order which build the lamellae of first order. They form an angle of mutual orientation of about  $109^\circ$  (according to Bandel, 1996). The bright lines, which cross the aragonitic structure parallel to the shell surface, are very thin layers of different composition with thickness of about  $16\ \mu\text{m}$ .

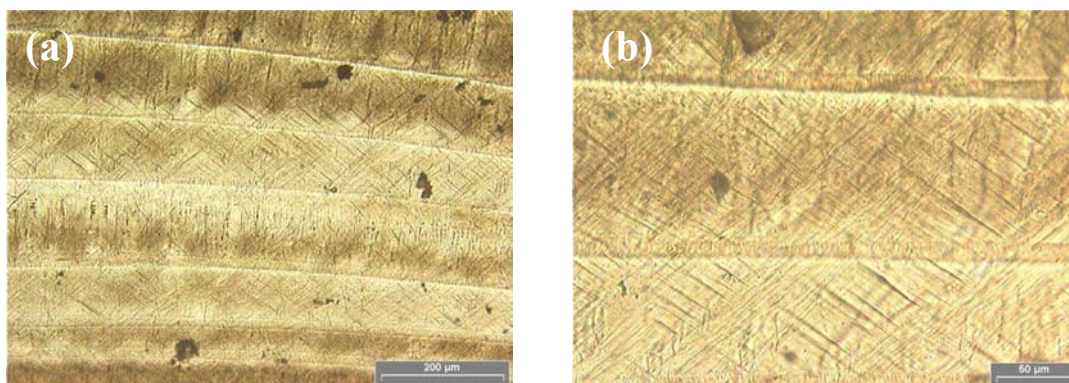


Figure 14: Polarizing microscope images of aragonitic crossed lamellae. (a) magnification 20x; (b) magnification 50x

Aragonite optical characteristics:

Biaxial crystals, like aragonite, have two directions of uniform light transmission. Symmetry planes of the indicatrix (i.e., principal sections) must be parallel to crystal symmetry planes in so far as the latter exist for the normal class of orthorhombic (aragonite), monoclinic and triclinic crystals. (Phillips, 1971)

For orthorhombic (aragonite) crystals, optical directions must be parallel to crystallographic directions, and the biaxial indicatrix has six possible orientations:

$$X=a, Y=b, Z=c; X=a, Y=c, Z=b;$$

$$X=b, Y=a, Z=c; X=b, Y=c, Z=a;$$

$$X=c, Y=a, Z=b; X=c, Y=b, Z=a$$

The angle between an extinction position of a grain or fragment and some crystallographic direction, as indicated by cleavage traces, crystal faces, or twinning planes, is its extinction angle. For uniaxial crystals (calcite), extinction is either parallel or symmetrical. Some biaxial (aragonite) crystal planes also show parallel or symmetrical extinction, but the characteristic extinction for low-symmetry crystal systems is inclined.

Orthorhombic crystals (aragonite) show parallel or symmetrical extinction. The extinction must occur parallel to all pinacoidal planes  $\{100\}$ ,  $\{010\}$ , or  $\{001\}$ ; symmetrical to pyramidal planes  $\{hkl\}$ ; and either parallel or symmetrical to prism  $\{hk0\}$  or dome  $\{h0l\}$  or  $\{0kl\}$  planes.

Orthorhombic minerals most commonly display cleavage parallel to pinacoids or prisms. Each pinacoidal cleavage  $\{001\}$ ,  $\{100\}$ , or  $\{010\}$  is independent, but prismatic cleavage  $\{hk0\}$  requires two cleavage directions.

**3.4.1. Crossed section**

By using crossed thin sections of aragonitic crossed lamellae we can observe (Fig. 15) the symmetrical extinction, which occurs at angles  $20^\circ/200^\circ$  and  $110^\circ/290^\circ$  for the first set of lamellae, and the second symmetrical extinction occurs at  $70^\circ/250^\circ$  and  $160^\circ/340^\circ$ .

The angle between the extinctions of two neighbouring lamellae is  $40^\circ$ .

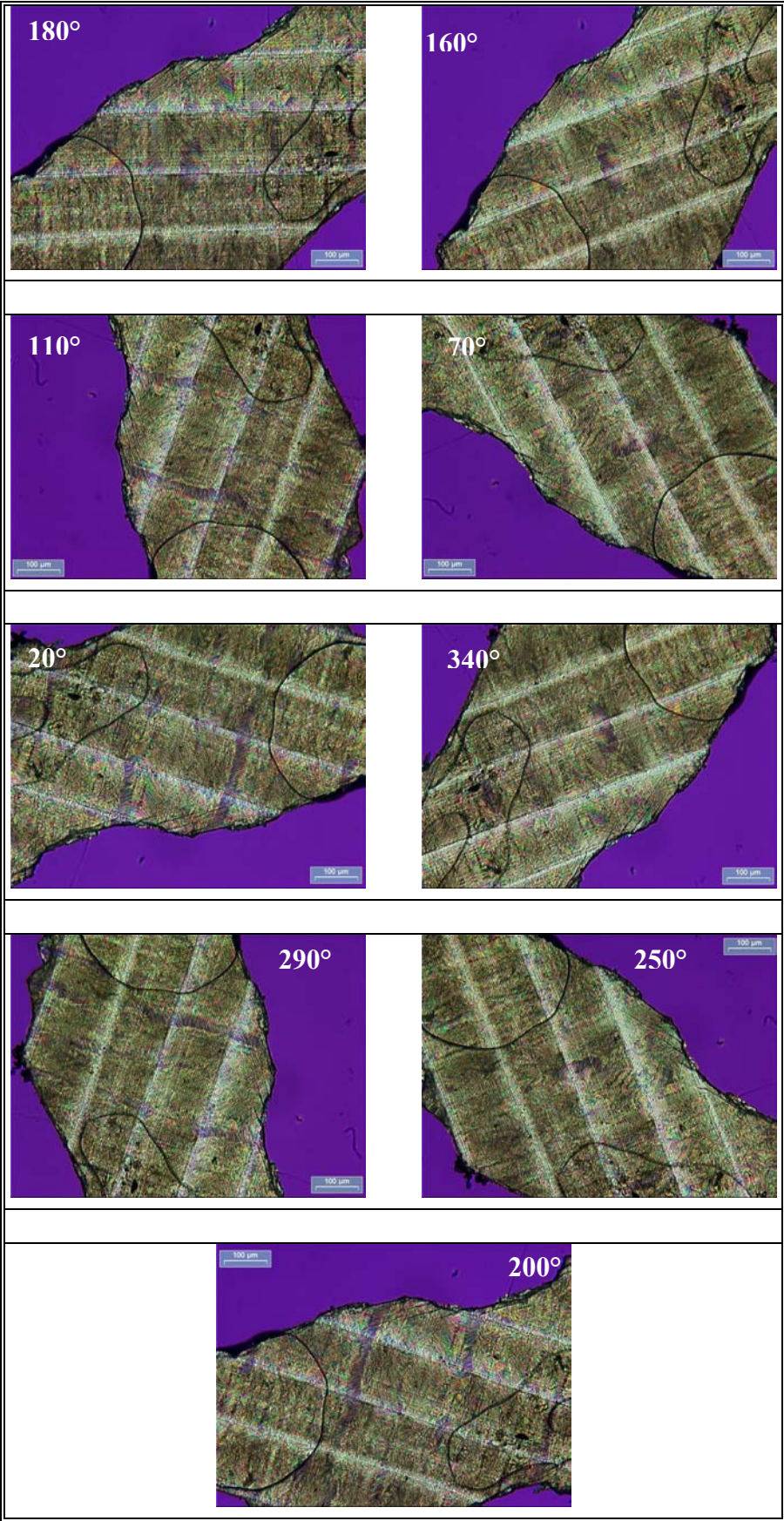


Figure 15: Polarizing microscope images of aragonitic cross lamellar structure at different angles with magnification 20x

### 3.4.2. Lateral section

In Figure 16 one selected orientation of the aragonitic lamellae of first order is shown at different magnification. The different colours indicate different orientations of particles within the lamellae.

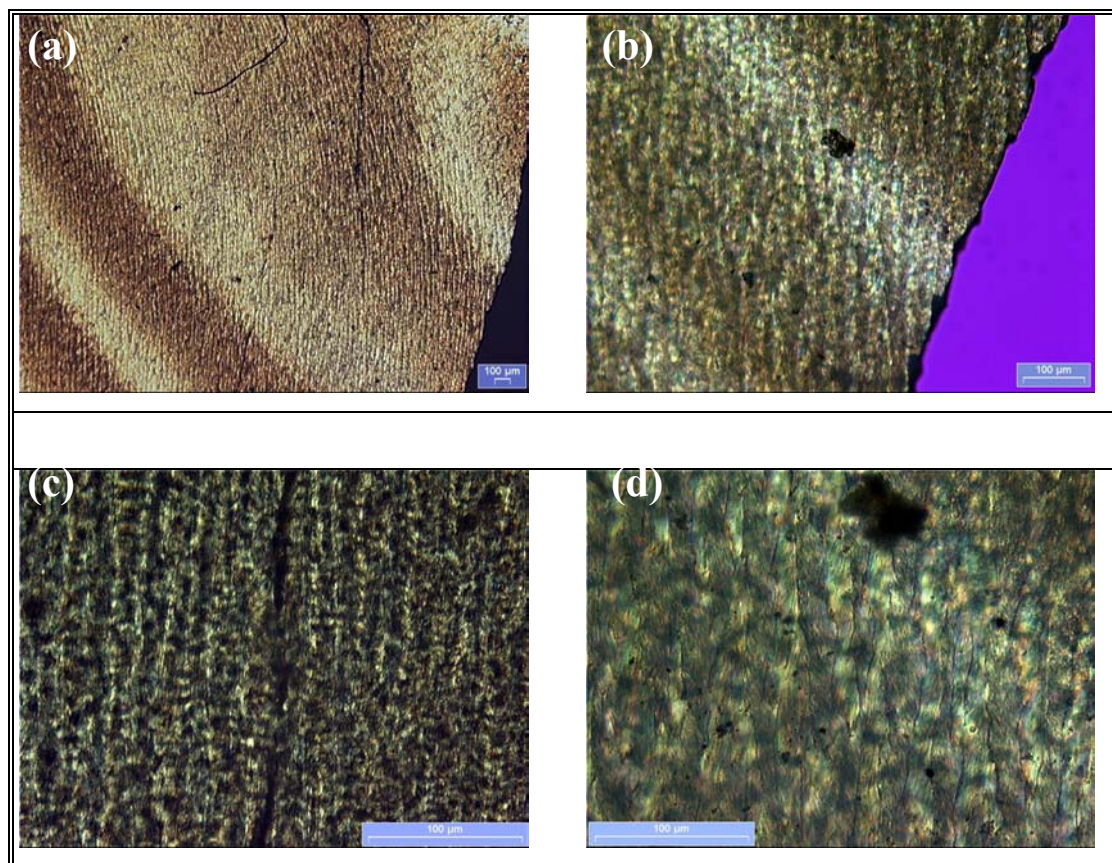


Figure 16: Polarizing optical images of aragonitic crossed lamellae with different magnification (a) 5x, (b) 10x, (c) 20x, (d) 50x.

### 3.5. Aragonitic myostracum

In Figure 17 polarizing optical microscope images of (a) the cross section, and (b) the lateral section of calcitic cross lamellae (1), and the aragonitic myostracum (2) are shown. There is no straight margin between the regions (1) and (2) (Fig. 17, a). A fractal-like line is formed from the roof-like spherulitic ends of the aragonitic myostracum. This type of contact between the minerals seems to be the perfect way to make the connection very stable and tight. In Figure 17, b small spherulitic parts of the myostracum are seen. They might be first seeds where the next epitaxially layer from the myostracum will grow.

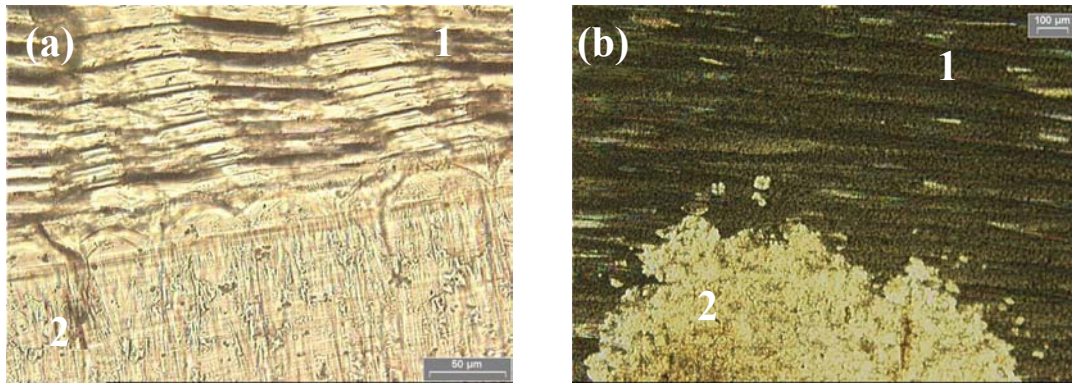


Figure 17: Polarizing microscope images of (a) cross section, and (b) lateral section of calcitic cross lamellae region (1), and aragonitic myostracum (2).

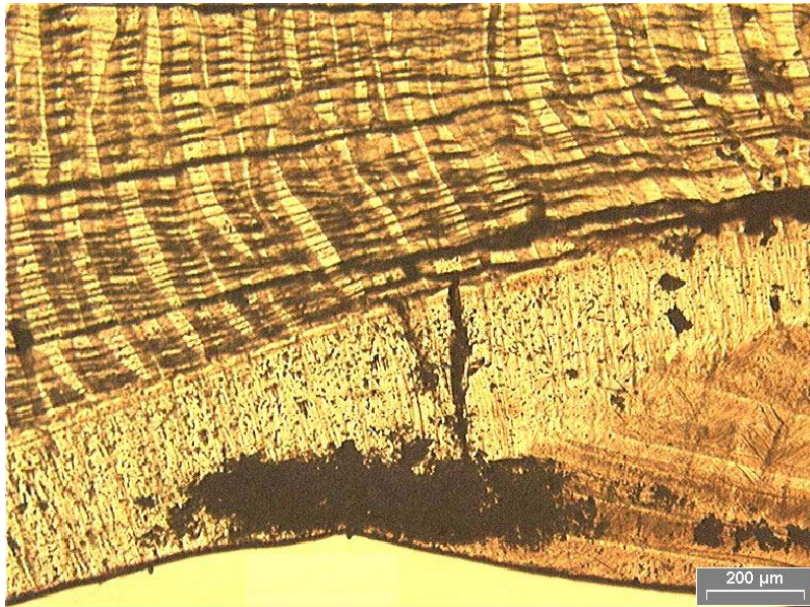


Figure 18: Polarizing microscope image of cross section of calcitic crossed lamellae (1), aragonitic myostracum (2), and aragonitic crossed lamellae (3).

## **Chapter V. X- Ray Diffraction Measurements**

X-rays are electromagnetic radiation of wavelength of about  $1 \text{ \AA}$  ( $10^{-10} \text{ m}$ ), which is about the same size as an atom and the interatomic distance. They occur in the electromagnetic spectrum between gamma-rays and the ultraviolet. X-ray diffraction is in use in two ways, for the fingerprint characterization of crystalline materials and the determination of the details of the crystal structure. Each crystalline solid has its unique characteristic X-ray powder pattern which may be used as a "fingerprint" for its identification. Once the material has been identified, the X-ray diffraction pattern may be used to determine its structure, i.e. where the atoms are located in the crystalline state. (Woolfson, 1970 and Hammond, 2001).

Samples of *Patella crenata* were studied by powder X-ray diffraction (XRD) method, single crystal X-ray diffraction (XRD) method and energy dispersive laue (EDL) diffractometer at F1 in HASYLAB, DESY.

### **1. Powder X-ray Diffraction (XRD) equipment**

X-Ray radiation of the used Philips X'Pert equipment was emitted from a copper tube, whose characteristic wavelength  $K_{\alpha 1}$  radiation,  $\lambda=1.5418\text{\AA}$  equipped with a secondary monochromator. When the incident beam strikes a powder sample, diffraction occurs in all possible orientations of  $2\theta$ . The counter was set to scan over a range of  $2\theta$  values at constant angular velocity. A  $2\theta$  range of 10 to 70 degrees was used, sufficient to cover the most useful part of the powder pattern. The scanning speed of the counter is was  $2\theta$  of 0.02 degrees and therefore, about 2 seconds was needed to obtain a trace.

For the powder XRD technique, a sample of the pulverized calcite or aragonite part of the shell is placed in a holder. The sample is illuminated with x-rays of fixed wave-length and the intensity of the reflected radiation is recorded. This data is then analysed for the reflection angle to calculate the inter-atomic spacing (d value). The intensity (I) is measured using I ratios. Various d spacings are compared to identify possible matches.

<b>Mineral</b>	<b>D1(I<sub>o</sub>)</b>	<b>D2(I/I<sub>o</sub>)</b>	<b>D3(I/I<sub>o</sub>)</b>
<i>Calcite</i>	3.035(1)	2.095(0.18)	2.285(0.18)
<i>Aragonite</i>	3.396(1)	1.977(0.65)	3.273(0.52)

## 2. Single crystal X-ray Diffraction (XRD) equipment

Determination of the atomic structure from X – ray data relies on measurements of the amplitude of scattered interfering waves. Since the wavelength of X – rays is about 1 Å, the phase shift during diffraction by the atoms cannot be determined experimentally. Therefore the electron density distribution in the unit cell will be calculated using Fourier transform techniques. Single crystal X-ray diffraction analysis was performed using a Nonius Kappa CCD diffractometer with MoK<sub>α1</sub> radiation.

The sample (e.g. a small piece of calcite of 20 μm) was mounted in a “fast” glue on a glass holder, which was fixed on a goniometer head.

## 3. Kappa-Diffractometer at F1 in DESY, HASYLAB

The Huber 4-circle diffractometer (in κ-geometry plus second concentric detectors-axis) with fixed vertical diffraction plane was originally designed for white beam applications (Energy-Dispersive Laue-diffractometer). It is equipped with an energy-dependent polarimeter, filter- and shutter-unit, collimator-assembly and solid state Ge-detectors. Alternatively, it can be used with a double-crystal monochromator operating either in the horizontal or in the vertical plane. Various detector arrangements may replace the Ge-detectors like scintillation counters or PSDs both in combination with collimators (Soller slits, capillaries, micro channel plates, analyzer crystals). A 1 K-SMART CCD system mounted on a second detector-axis is also available. The machine is controlled by PC, using CAMAC interfacing and control. Data collection is performed through a MCA counting chain. The control software is based on that developed for the 4-circle diffractometer at D3, with some differences, concerning special energy-dispersive features. A wide-band double-crystal graphite monochromator is available. There is the possibility to use attachments for temperature and pressure dependent work or to measure with other components either on detector or on the additional translation stage (opening perpendicular to the beam).

Instrument Specifications: (Eichhorn, K., 1991) and (Fischer, K. et. al., 1996)

Source (4.5 GeV):	bending magnet, $E_c = 16,6$ keV, positron beamsize $4,6 \times 1,1$ mm <sup>2</sup> FWHM (hor x vert), vert position beam divergence 0,06 mrad FWHM
Flux at the sample:	$10^{11}$ photons mm <sup>-2</sup> s <sup>-1</sup> , 0,1% bw, 100 mA
Monochromator:	RÖMO-type, turnable around incident beam, Si(111) crystals

Energy range:	0,4Å – 2,5 Å, Si(111)
Energy resolution:	$\Delta E/E \approx 10^{-4}$ (Si), $\approx 10^{-1}$ (C) white beam: $0,05$ (5 keV) $\geq \Delta E/E \geq 0,005$ (100 keV)
Diffractometer:	Huber 4-circle plus 2nd concentric detector circle, analyzer crystal optional
Beam size:	3 x 3 mm <sup>2</sup> standard (continuous adjustment), minimal 25 x 25 μm, up to 50 x 10 mm <sup>2</sup> for special purposes only
Angular range:	$-45^\circ \leq 2\Theta_1 \leq 160^\circ$ , $-120^\circ < 2\Theta_2 < 135^\circ$ , $-180^\circ < \omega, \kappa, \phi < 180^\circ$
Stepsize:	0,001° in all circles
Goniometer heads:	standard ACA/IUCr-mount, the $\phi$ -circle (410-Huber Drehkrise) includes a height adjustment. Surface $\phi$ -circle – diffractometer centre = ca. 120 mm
Background:	typically 5 – 50 cps, depending on $2\Theta$ -angle and detector aperture
Detector	solid state Ge-detector, NaI(Tl) scintillation counter, imaging plate, SMART CCD system, PSD, with translation stage. Surface detector arm – diffractometer centre = ca. 200 mm
MCA:	PC-based MCA-system of data collection
Computer:	PC/AT, Ethernet connection to VAX-cluster, PC-CAMAC-Adapter for experimental control
Auxiliary equipment:	collimator, filters and shutters, microscope, laser beam unit, film / imaging plate cassette
Table:	$-2^\circ/-1^\circ$ , 150 mm/-0 mm with regard to white beam

#### 4. Results and Discussion

##### 4.1. X-ray powder diffraction studies

Figure 19 and 20 show a typical X – ray powder diffraction pattern as obtained with the position sensitive detector, for aragonite and calcite lamellar sections of *Patella crenata* respectively.

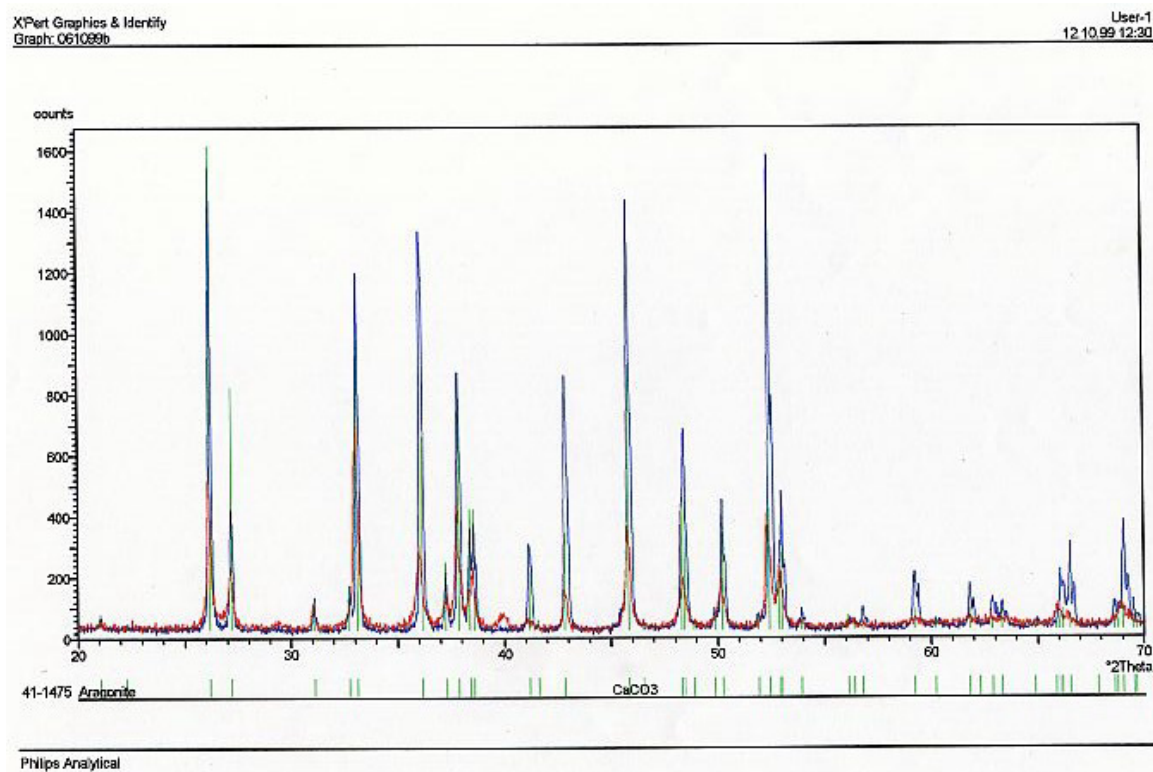


Figure 19: Typical X-ray diffraction pattern of aragonite of *Patella crenata*.

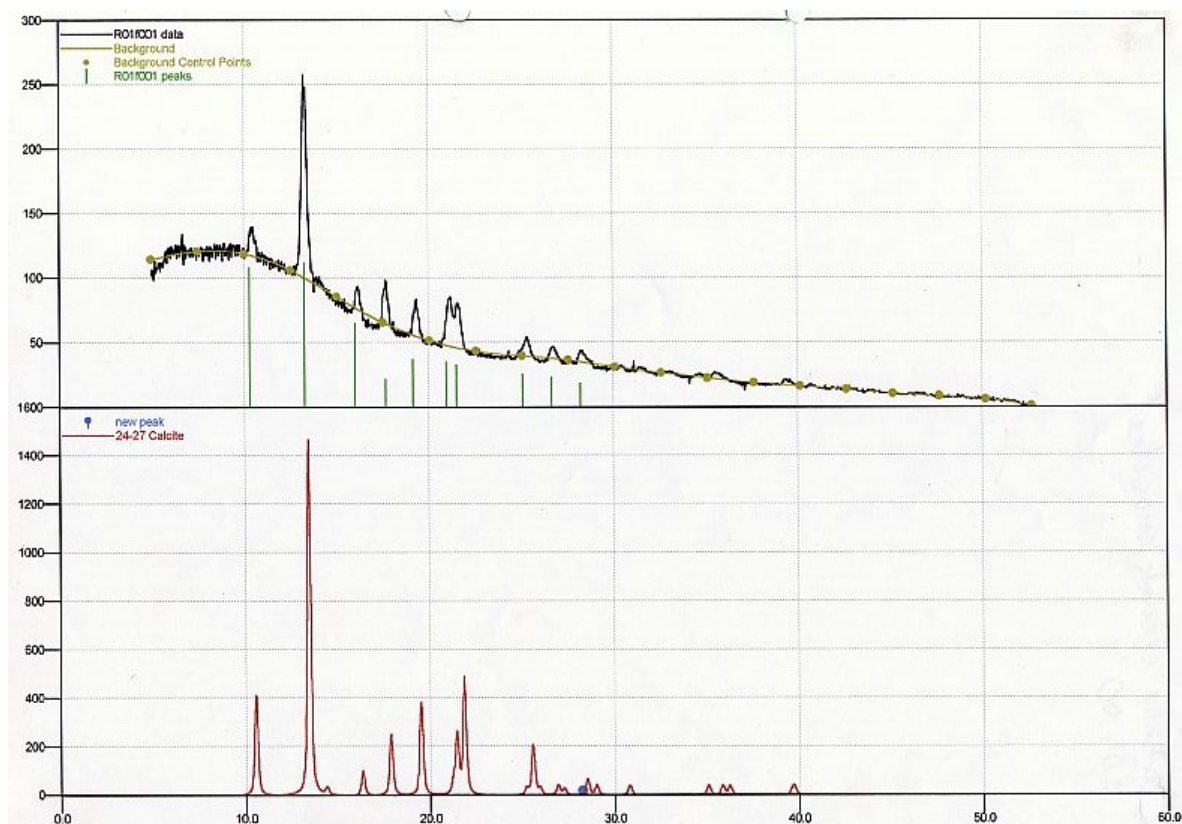


Figure 20: Typical X-ray powder diffraction pattern of calcite of *Patella crenata*.

#### 4.2. X-Ray single crystal diffraction (XRD) studies

In order to study the long-range order in *Patella crenata*, single crystal diffraction studies are performed of parts from the calcite and aragonite lamellar sections (as shown in Fig. 7 position 1 and position 3 respectively). In Figure 21 and 22 corresponding diffraction signals (CCD frame) are shown.

The diffraction patterns show that the calcitic material tends to show considerably higher degree of long-range order compared to the aragonitic material with diffuse features of powder diffraction signals indicating a more amorphous structure. The lattice constants obtained from the orientation matrix corresponding to Figure 21 yield lattice constants  $a = 4.94 \text{ \AA}$  and  $c = 16.80 \text{ \AA}$  for calcite which is within an error of 2 % close to the literature data (please note that the sample is no single crystal). The diffraction behaviour which displays short correlation length confirms earlier observations of Tong et al. (2002).

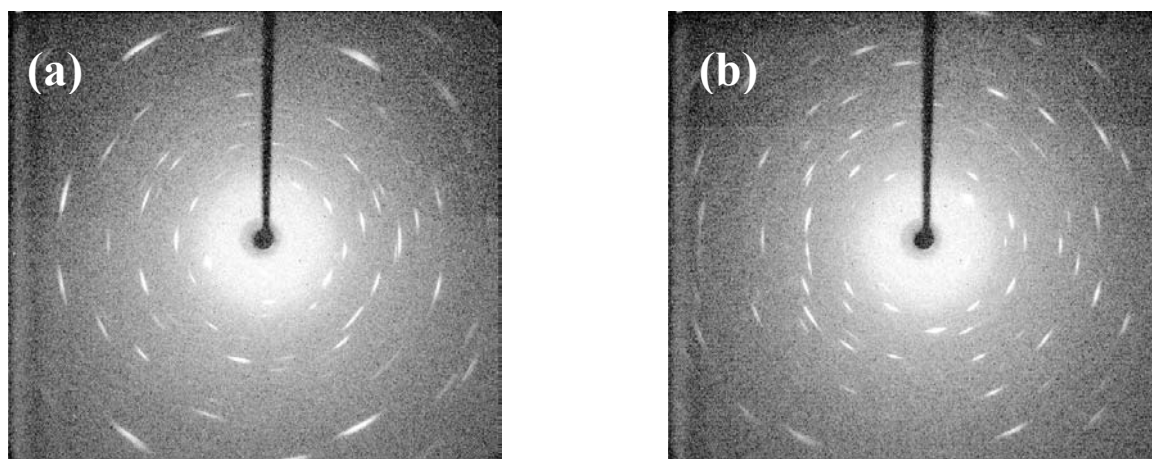


Figure 21: Diffraction studies (CCD frame) of calcite lamellar sections. (a) sample rotation around **a** axis; (b) sample rotation around **c** axis.

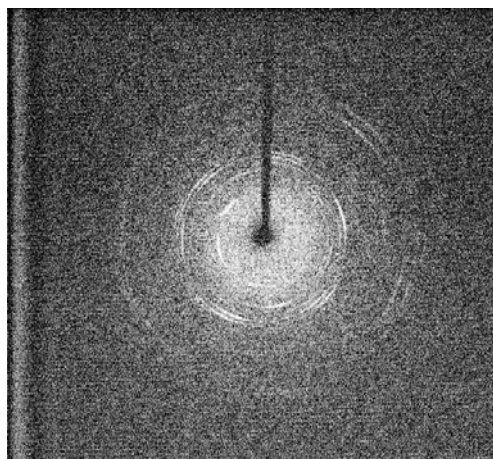
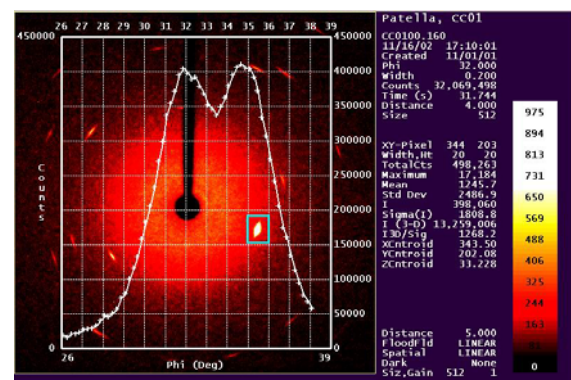
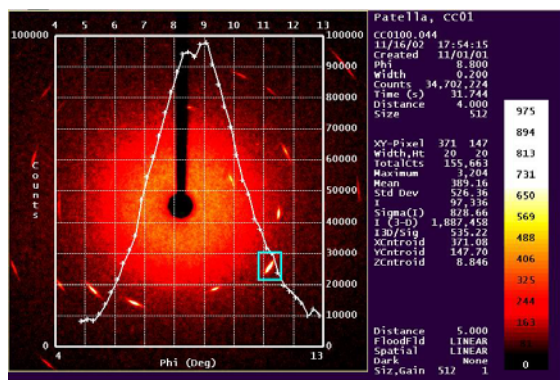
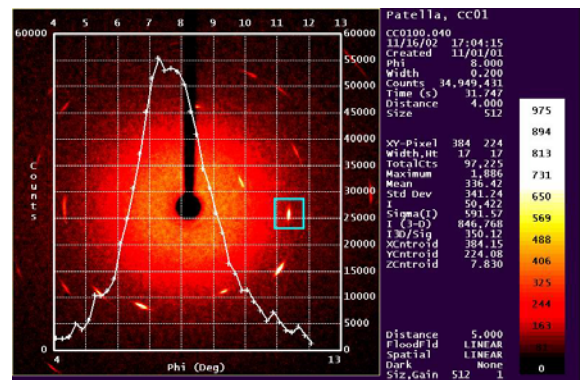
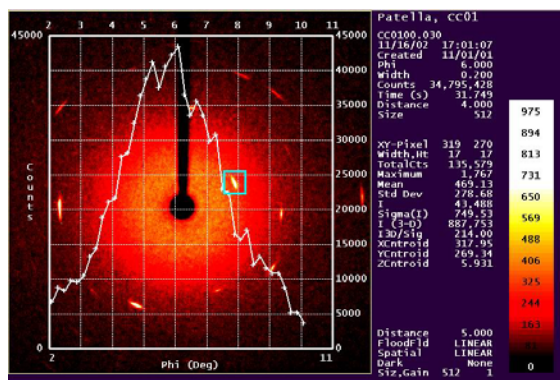


Figure 22: Diffraction studies (CCD frame) of a aragonite lamellar section.

### 4.3. Kappa-Diffractometer at F1, DESY, HASYLAB study

Monochromatic diffractometric (KAPPA-diffractometer) studies of calcite crossed lamellar sections of *Patella crenata* are performed in order to study the short-range order in *Patella crenata*.

Figure 23 shows representative CCD frames of some typical X-ray diffraction patterns of a calcite specimen, obtained at F1, DESY, HASYLAB. It shows the sum of 450 measurements for every position of the sample. With the wide slotted counter set at a known Bragg angle,  $2\theta_B$ , a crystal is rotated through  $\theta_B$ . The resulting intensity versus  $\theta$  (or  $\omega$ ) is known as a rocking curve which is shown in Figure 23. The width of the rocking curve is a direct measure of the range of orientations present in the irradiated area of the crystal, as each sub-grain of the crystal will come into diffraction position as the crystal is rotated.



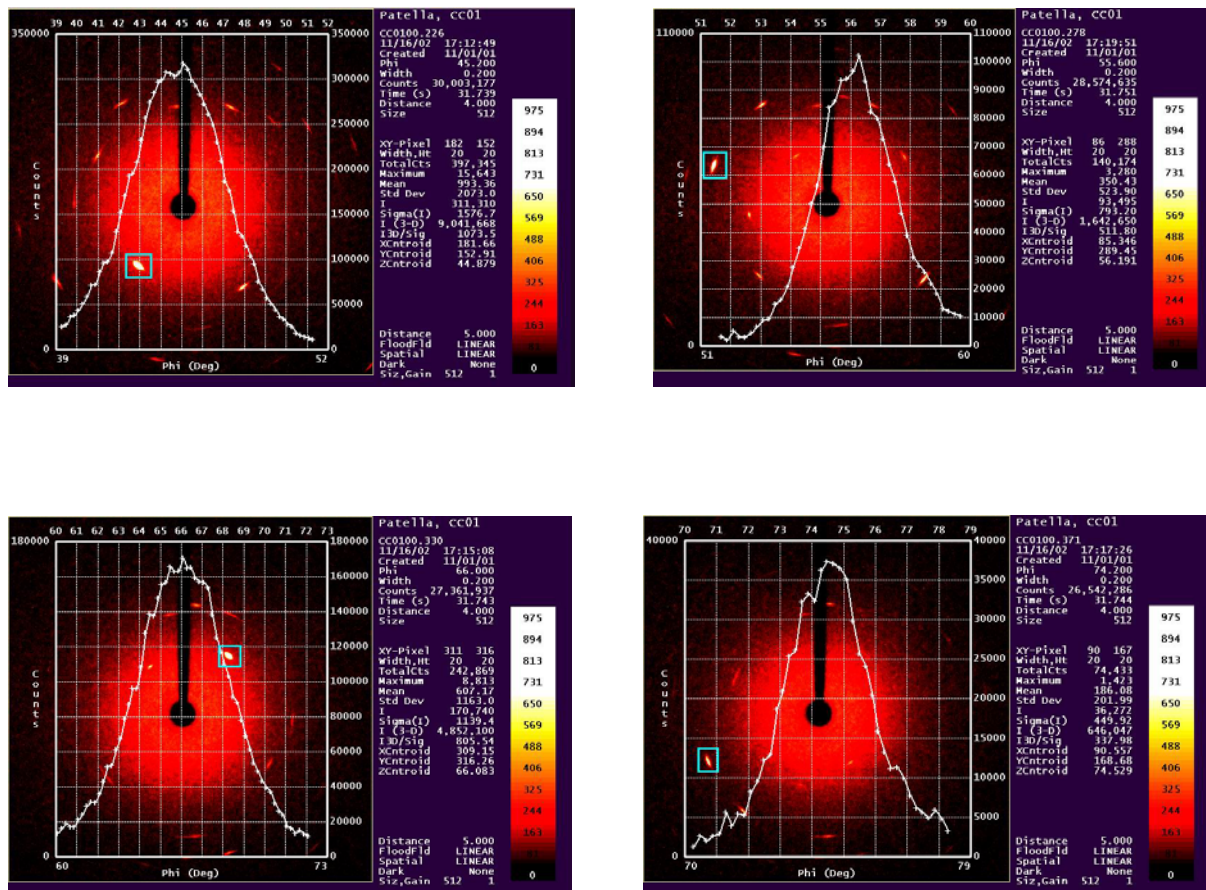


Figure 23: Representative X-ray diffraction CCD frames of a calcite specimen, obtained at F1, DESY, HASYLAB. The intensity versus  $\theta$  (or  $\omega$ ) curve (rocking curve) for a selected reflection is also shown.

For the studied specimen of calcite, the observed diffraction peaks are most probably diffraction of a composite mass, since a very narrow peak is observed for a single crystal. If the size of the individual crystals is less than about  $0.1 \mu\text{m}$  ( $1000 \text{ \AA}$ ), the x-ray signal shows broadening. This is referred to as particle size broadening. As the average size of the crystallites decreases, the angular spread of the reflection from the sample increases. On the other hand the observed diffraction peaks, shown in the Figure 23 have a fine structure which is an image of the examined calcite specimen. The image arises due to particle reorientation. In this case most probably the field of small randomly orientated elements of nanometer size is seen combined to form the composite mass of the studied specimen. A decrease in grain size is well known to accompany an increase in hardness and strength of a polycrystalline material like in ceramics.

## **Chapter VI. Electron Microscopy Investigations**

In the electron microscope a diffraction pattern is obtained in the back focal plane of the objective lens. This is similar to X-ray techniques. The Fourier transform of the electrostatic potential differences in the specimen corresponds to the electron density distribution. In contrast to X-rays, by the electron microscopy, under ideal conditions, one obtains the inverse transform of the diffraction pattern in the image plane without losing the phase information. The *electron microscope (EM)*, also *scanning electron microscope (SEM)* is an ideal instrument to investigate local inhomogeneities in minerals. *Transmission electron microscopy (TEM)* of thin crystals, is also a technique which has had so far the greatest impact on materials research. Through application of *high resolution electron microscopy (HRTEM)* it is possible to record two-dimensional images of the material with a resolution of about 1.5 Å in which single atoms can be recognized.

### **1. Scanning Electron Microscopy (SEM) investigation**

Scanning electron microscopy (SEM) is a method for high-resolution imaging of surfaces. For imaging the SEM uses electrons in the manner a light microscope uses visible light. The electrons are produced by a thermal emission source, such as a heated tungsten filament, or by a field emission cathode. The advantages of SEM over light microscopy include much higher magnification (100,000x) and greater depth of field (up to 100 times that of light microscopy).

#### **1.1.SEM equipment and sampling**

Electron microscopic studies are performed using a LEO VP 1455 equipment with a wolfram emission cathode. Accelerating voltage of 15 keV was applied. For high-resolution secondary electron imaging, the sample environment is at pressure below  $1 \times 10^{-5}$  Torr.

The samples for SEM studies are selected from all the three parts of the cross-section of the shell as shown in Figure 3. The studied nonconductive samples are coated by evaporation with a thin carbon film followed by gold and attached to a copper support grid.

#### **1.2.Results and Discussion**

Morphological observations obtained by the polarized light microscope measurements are confirmed by SEM data (Fig. 24 to 32). Enhanced contrast of studied thin sections (perpendicular to the surface) from calcite (Fig. 24 to 28), aragonite (Fig. 31 and 32), and

aragonitic myostracum (Fig. 29 and 30) show different types of the crossed lamellar pattern. The crossed lamellae of both materials (calcite and aragonite) are organized in first, second, and third order lamellae. Each layer usually shows a heterogeneous lamellar pattern. The smallest components of the pattern are the elements of the third order.

### **1.3. Calcite crossed lamellae.**

Figure 24 shows typical SEM images of calcite crossed lamellae of first order. The studied sample was prepared by thin cutting perpendicular to the shell surface. Close examination of Figure 24, (a) reveals a complex arrangement of the lamellae. Near the shell surface (the upper part on the figure) lamellae ends are curved to the right, in the direction to the apex of the shell. The higher magnification (Fig. 24, (b)) of a selected area shows a common feature in all investigated lamellae - alternating dark and bright lamellae of first order which occur in the same optical plane. The pattern indicates different crystallographic orientations of the crystallites in the lamellae.

Arrows indicate where a new bright lamella starts to grow or ends within a dark lamella.

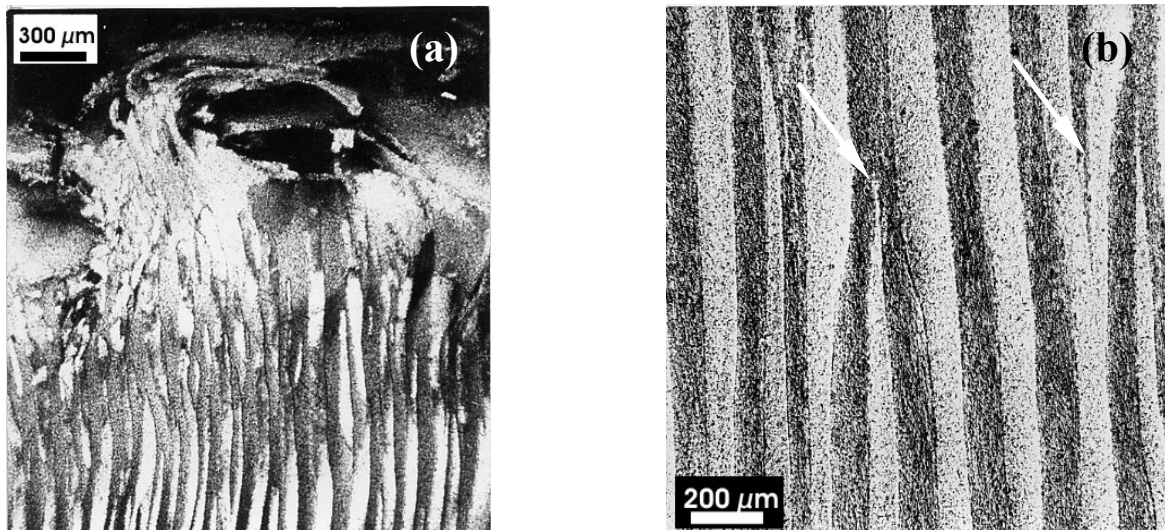


Figure 24: (a) SEM images of calcite crossed lamellae of first order; (b) higher magnification of a selected area in the centre of (a).

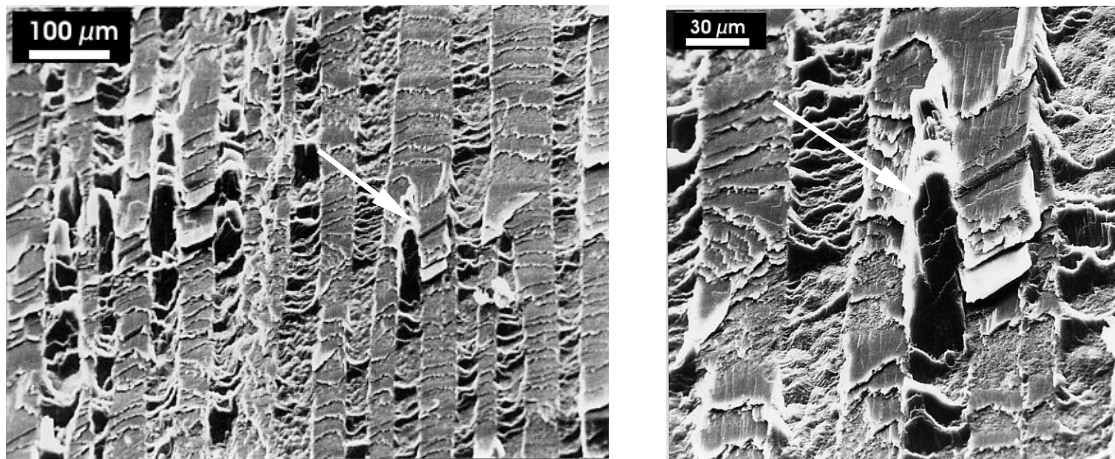


Figure 25: SEM image of (a) calcitic crossed lamellae obtained by breaking of the shell; (b) higher magnification of a selected area of (a).

Figures 25 and 26 show the complex arrangement of calcitic crossed lamellae of samples obtained by breaking the shell perpendicular and slant-wise to the surface, respectively. It seems likely that lamellae particles have one preferred orientation within one lamella and are positioned across each other. The higher magnification image (Fig. 25, (b)) shows the lamellae of second order building the lamellae of first order. Sheets-like arrangement of the second order lamellae can be observed. Arrows mark where a new lamella appears within the multi-lamella pattern. It is seen how one lamella may also influence the arrangement of all other lamella.

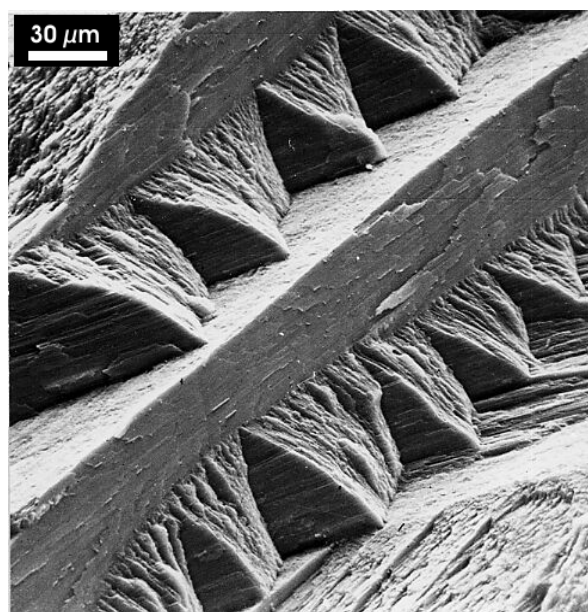


Figure 26: SEM image of calcitic crossed lamellae obtained by slantwise breaking.

Figure 26 shows the complexity of the arrangement of first, second and third order calcite crossed lamellae, obtained by slantwise breaking. Two types of alternating lamellae are seen: the first one is parallel to the broken surface; the other lamella is oriented at an angle of  $15^\circ$  to the first one. The trapezium-like pattern reveals the lamellae of the second order that appear to consist of micro-layers, namely the lamellae of third order.

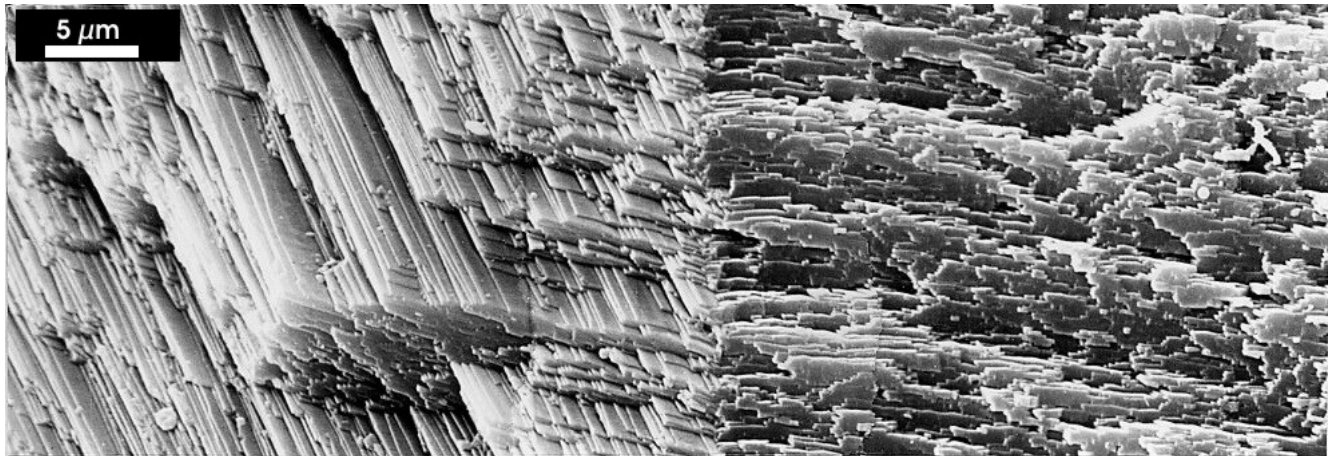


Figure 27: SEM image of two neighbouring calcite crossed lamellae of first order after radial breaking nearly perpendicular to the shell surface.

Figure 27 shows a higher magnification of two neighbouring calcite crossed lamellae of first order obtained after breaking the shell nearly perpendicular to the shell surface. Close examination of Figure 27 reveals the border between two lamellae of first order. On the left side in Figure 27 thin sheet-like lamellae of the second order are occur.

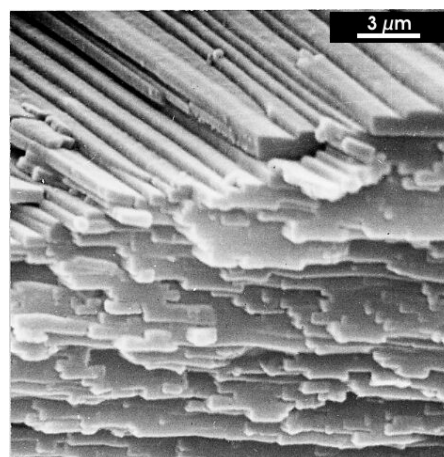


Figure 28: Higher magnification of a selected area from Figure 27.

The higher magnification of a selected area from Figure 27 reveals lamellae of second order (Fig. 28) consisting of sheet-like lamellae of the third order.

#### **1.4.Aragonitic Myostracum.**

Figures 29 (a) and 29 (b) show three different layers running through the shell: the calcite outer layer (1), which borders to with the aragonitic myostracum (2), and finally the aragonite layer (3) overgrowing the myostracum (2) during the ontogeny. The higher magnification (Fig. 29, (b)) reveals several roof-like bulges (indicated by arrows) at the border between the regions (1) and (2). The spherulitic sectors seem to be firmly attached to the calcite crossed lamellae.

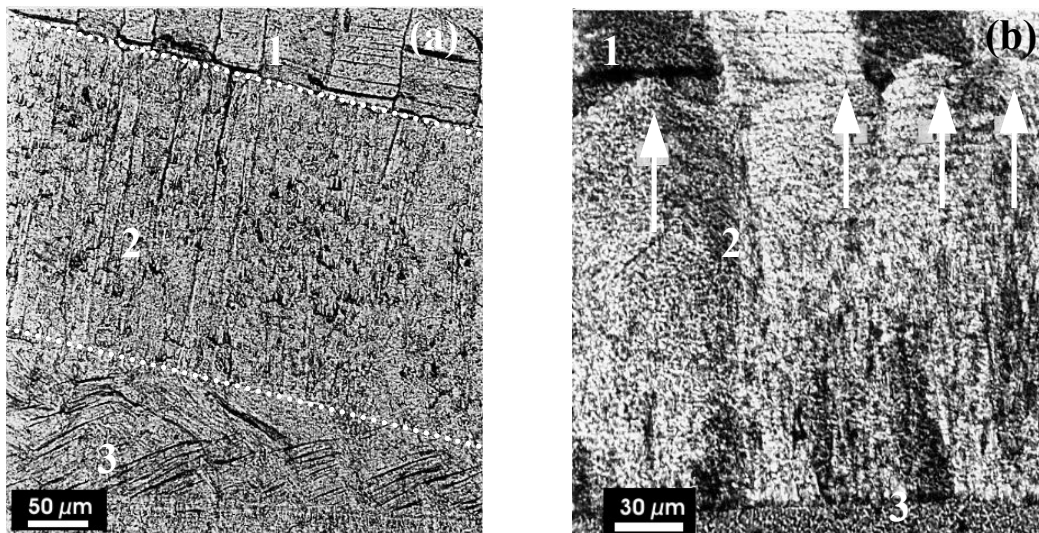


Figure 29: SEM image of the aragonitic myostracum; thin cut from the cross section  
(a) lower magnification; (b) higher magnification.

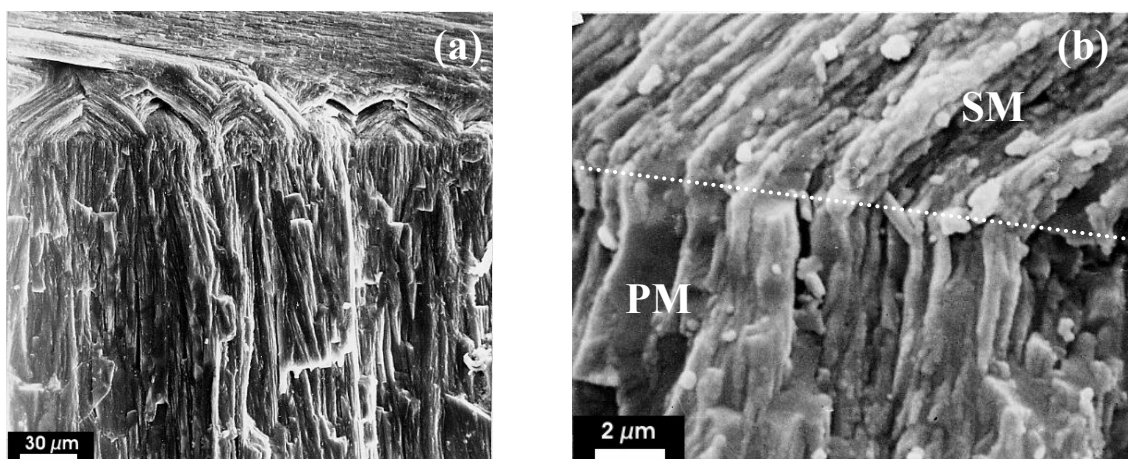


Figure 30: SEM image of the aragonitic myostracum.(a) lower magnification; (b) higher magnification.

Figure 30 (a) shows the aragonitic myostracum which is arranged in two parts: one of the spherulitic region, bordering the calcitic crossed lamellae and the other one consisting of dense layers of prisms. The higher magnification image (Fig. 30, (b)) shows how the crystallites of the spherulitic myostracum (SM) region merge without interruption with crystallites of the prismatic myostracum (PM).

### **1.5. Aragonite Hypostracum cross lamella**

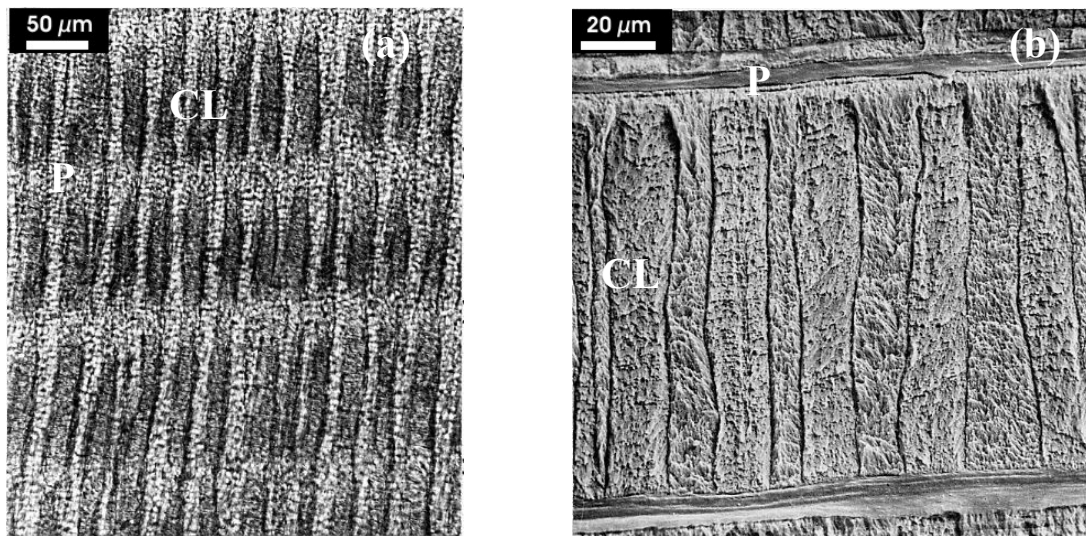


Figure 31: SEM images of a thin cut of aragonitic crossed lamellae (CL) in cross section, slightly etched in KOH (a) at lower magnification; (b) at higher magnification. Aragonitic prismatic interlayer is marked by (P).

Figure 31 shows SEM images of alternating patterns of aragonitic crossed lamellae (CL) and lamellae with aragonitic prismatic interlayers (P). The studied samples are etched in diluted KOH. The higher magnification (Fig. 31, (b)) reveals in distinctly separated lamellae of first order while the lamellae of second order can be distinguished in different orientation.

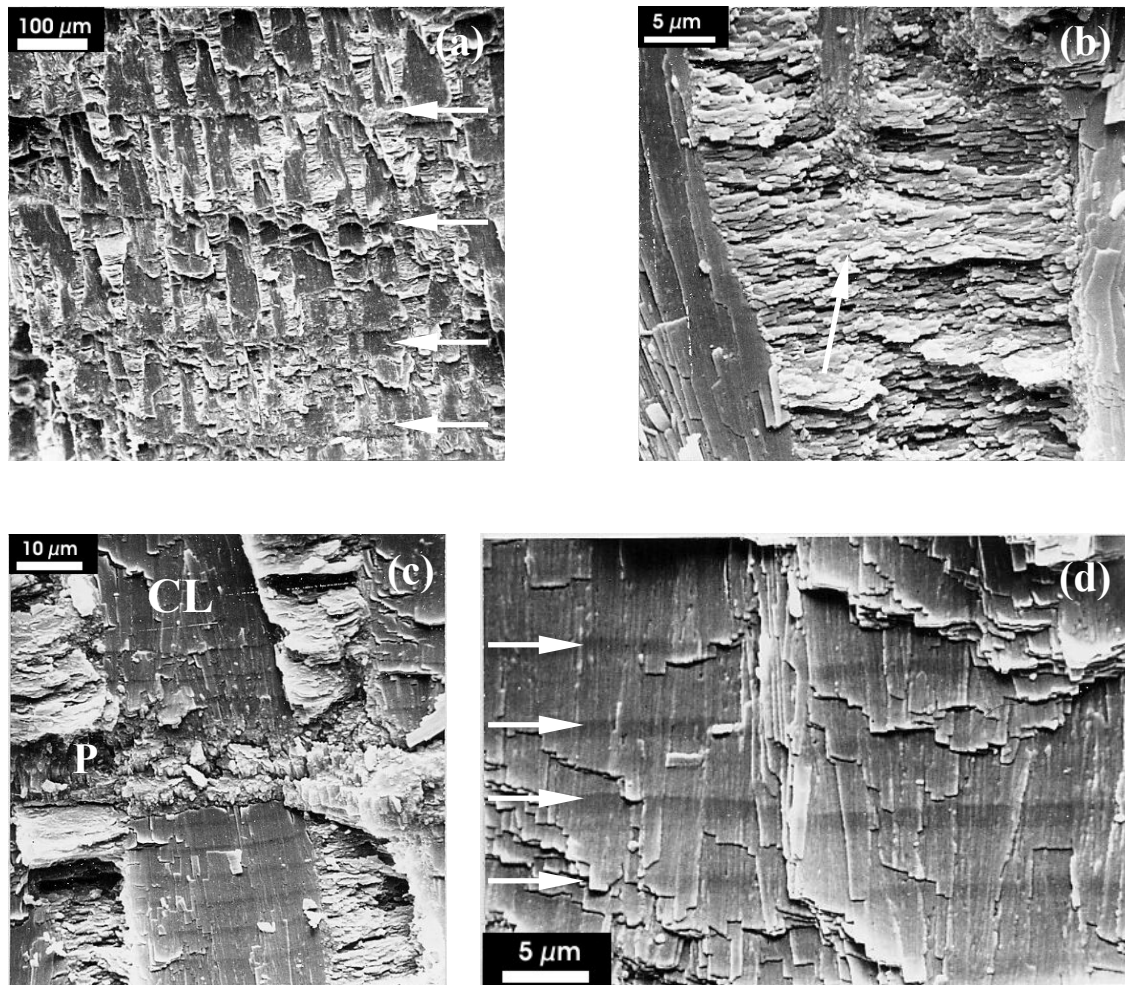


Figure 32 SEM images of aragonitic crossed lamellae (CL) obtained by cross breaking of the shell. (a) lower magnification; (b) higher magnification; (c) lower magnification; (d) higher magnification.

A specific region of aragonitic crossed lamellae, obtained by cross breaking of the shell shows (Figure 32) dark lamellae of the second order that are situated approximately parallel to the figure plane. The arrangement of bright stripes are the lamellae of first order and lamellae of second order are oriented perpendicular. The position of the prismatic interlayer is signed by white arrows on the figure. Closer examination of Figure 32, (c) and 32, (d) reveals some special features of the arrangement of aragonitic crossed lamellae. The prismatic interlayer (P) is situated perpendicular to the aragonitic crossed lamellae (CL) of first order. The vertical dark stripe is a lamella of first order is build of lamellae of second order lying parallel to the plain of the figure. Figure 32, (d) shows fine vertical lines that indicate the position of third order lamellae within a lamella of second order. The dark stripes marked by the arrows are the so called “pulsed growing” stripes. The morphology obtained after cleaving the sample is complex. The irregularities of the studied surface act as (local)

concave or convex mirrors and a collimated light beam reflected from the surface displays perfectly the surface topology. (Riesz, 2000) and (Riesz et al., 2002). Light and dark stripes are also discussed in Fallon, (1999) as related to different shell density and the growth of massive coral porites. In Figure 32 (c) it is seen that the number of the “pulsed growing” strips between two prismatic interlayers is about 30 with a distance of about 4  $\mu\text{m}$ . The thickness of one lamella of third order is about 200 nm (Fig. 32, (d)).

## **2 Transmission Electron Microscopy (TEM) investigation**

In TEM a thin specimen is illuminated with electrons. TE microscopes are constructed after transmission light microscopes and yield similar information. The size, shape and arrangement of the particles building a specimen as well as their mutual relationship on the scale of atomic diameters can be studied. The arrangement of atoms in the specimen and their degree of order, detection of atomic-scale defects can be obtained in areas of nanometers' size. A TEM works much like a slide projector and interaction occurs with the samples electrons. As the light passes through the sample, it is affected by its local structure. The transmitted beam is then projected onto the viewing screen, forming an enlarged image of the object. TEMs work by using a beam of electrons through the specimen. The transmitted part is projected onto a phosphor screen for the user to see. TEM magnification is 100 to 1,000,000 times.

### **2.1. Transmission Electron Microscopy equipment and sampling:**

The TEM measurements of studied aragonite specimens are performed at EMAT, Antwerpen, using a Philips microscope CM200 in a bright field image. The microscope combines a good resolution (0.27 nm) with a range of analytical capabilities. *A bright field image* is formed using light (or electrons) transmitted through the specimen. When the objective aperture is centred about the optical axis and no specimen is present, then a bright background is seen. For high resolution images (HRTEM) a JEOL 4000EX equipment with a maximum acceleration voltage of 1000kW, was used for analysis of the fine structure of samples reduced by the splash ion. Selected area diffraction pattern was used for distinguishing amorphous and crystalline structures. The TEM high-resolution measurements of aragonite specimen is conducted at low-magnification (100,000) and at high-magnification (800,000) at room temperature.

Specimens thin enough for TEM examination were prepared from aragonite (Fig. 24, region 3) by ion-thinning with 5 keV  $\text{Ar}^+$  ions.

## 2.2. Results and Discussion

TEM investigation of the aragonite region of the shell (Fig. 24, region 3) indicates that there are significant differences between zones of the specimen. Using the electron diffraction pattern of the selected area (see inset (a) in Fig. 24) for analysis of the above zone, it is reasonable to assume that the bands of diffracting contrast in aragonite are in a twin relationship. The studied aragonite region of the shell is heavily twinned as can be seen on the low-magnification of the high-resolution image in the Figure 24.

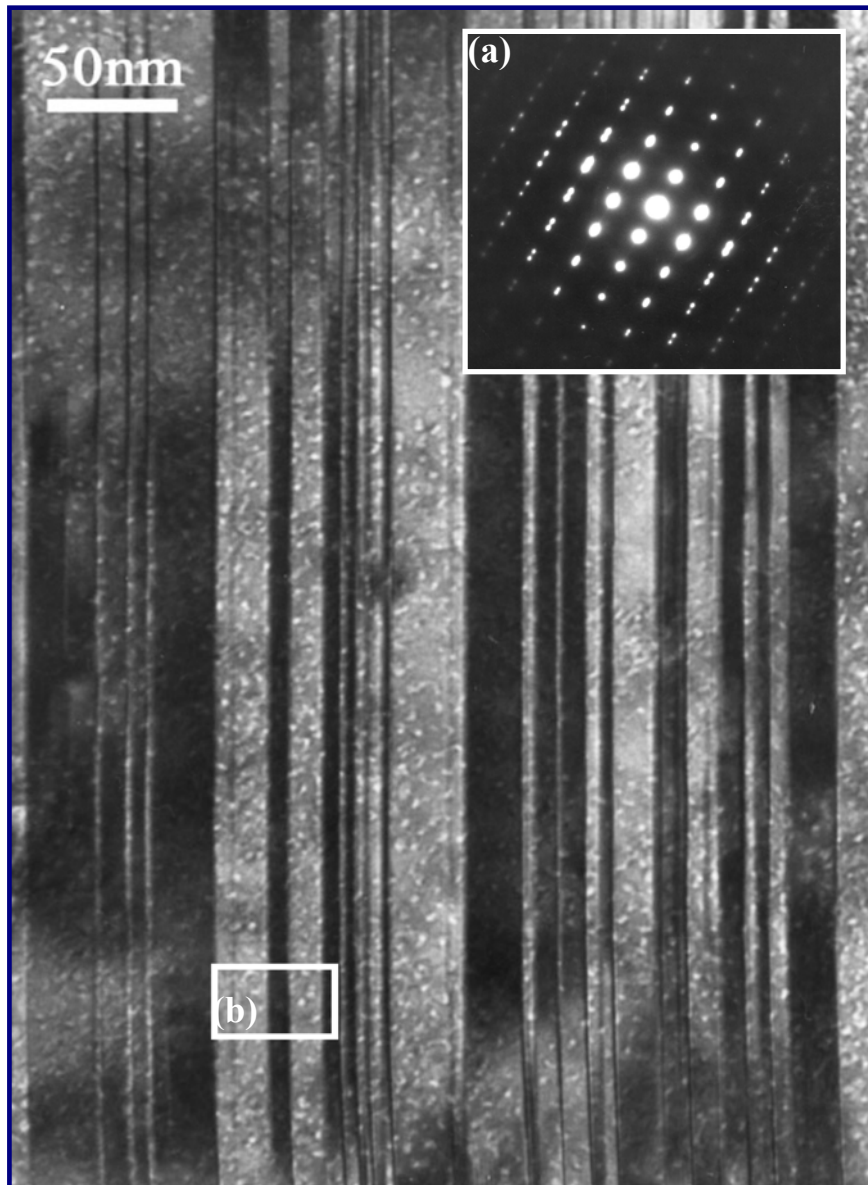


Figure 24: TEM high-resolution image (low-magnification) of twinned aragonite with corresponding electron diffraction pattern (inset-a).

The twins in the studied aragonite can be very small. In Figure 25, the TEM high-resolution image of the area is shown at high-magnification, marked in Figure 24 with an

outline (b). There are characteristic periodic patterns on the atomic length scale as well as variations in darkness from one to the next twin, due to the variation of the short-range order.

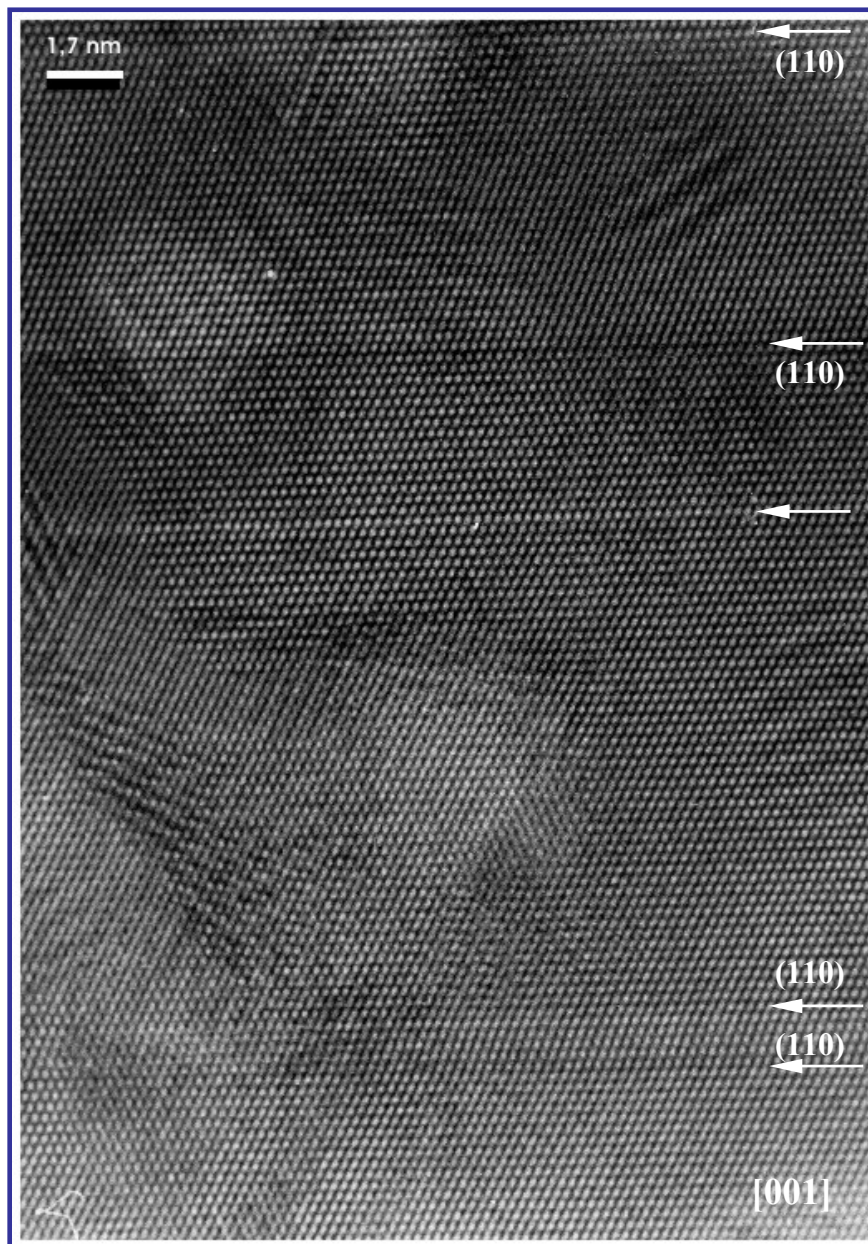


Figure 25: TEM high-resolution image of a selected region, marked in Figure 24 by (b).

Orientation variants of about three 110 - interplanar distances (i.e. about 1.25 nm) are observed. The twin plane is the (110) plane. Besides, in Figure 25 another “defect line” (marked by arrow) is observed. This might be an anti-phase boundary, separating two translation variants and viewed parallel to the boundary. In order to see the defect separating two regions with the same orientation but shifted over half a lattice vector, it would be necessary to observe the sample in the perpendicular direction. This could not be achieved.

Mainly two types of twinning can be distinguish:

Crystal twinning creates boundaries that occur during the crystal growth where the energy state near the twin boundary is slightly higher than that of a single crystal. Most of these twinned crystals grow naturally by the addition of clusters of atoms.

Lamellar twinning is a special kind of crystal twinning (also called 'multiple' or 'repeated' twinning) where there are many twin individuals of tabular or plate-like appearance. Lamellar twinning is common in plagioclase feldspars, in places where two adjoining twin slabs or lamellae are mutually reversed and every alternate twin 'plate' or 'slab' has an identical atomic structure.

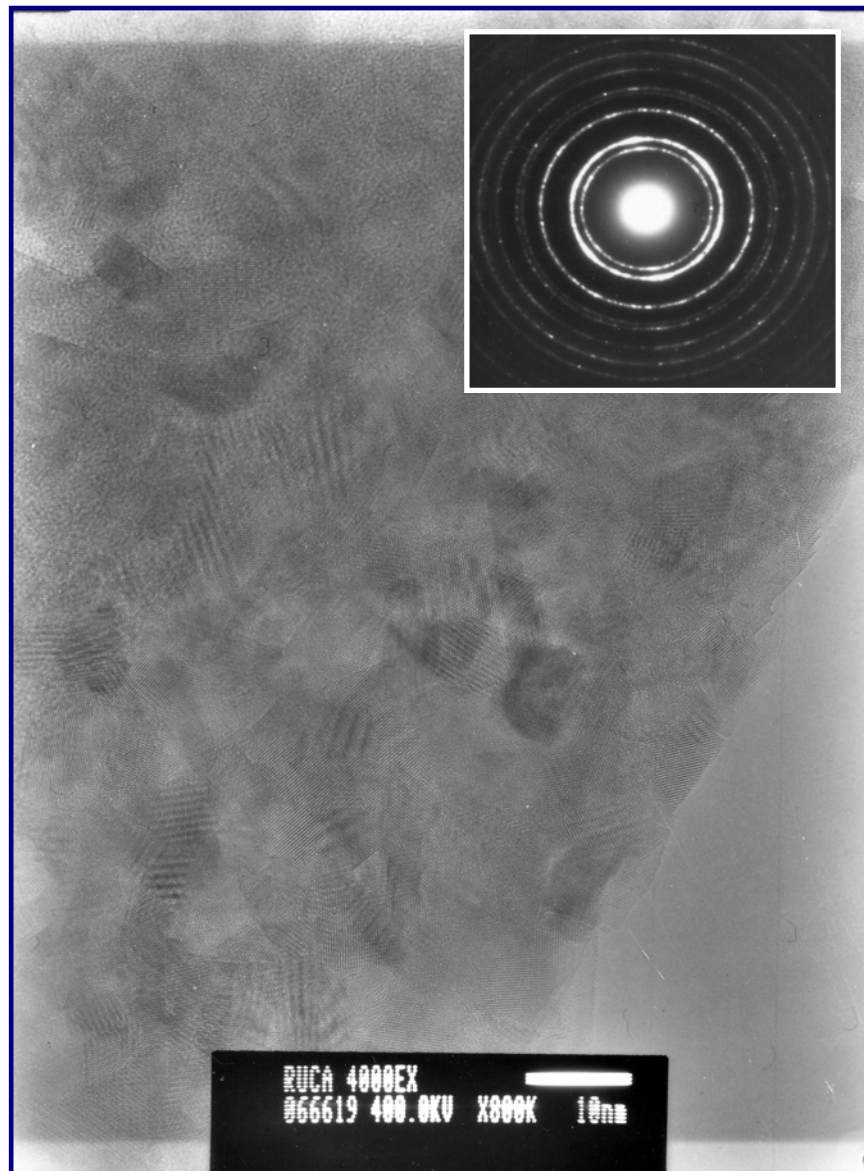


Figure 26 TEM of a high-resolution image (low magnification) of aragonite during transformation into calcite. The inset corresponds to the diffraction pattern of the polycrystalline calcite.

TEM investigation show that the aragonite material is rather beam sensitive. In the electron beam, necessary to obtain high-magnification of high-resolution image, aragonite transforms into polycrystalline calcite. In Figure 26 TEM high-resolution image of the transformation of aragonite is shown at low-magnification. The corresponding electron diffraction pattern of the selected area (Fig. 26) is no longer a spot-pattern (inset (a) of Fig. 24) but consists instead of rings due to the presence of various particle orientations of small size.

Also the calcite is polycrystalline. The fact that aragonite transforms into another crystalline phase supports that the studied aragonite and calcite are close in free energy (at this temperature). The lattice energy of aragonite is less exothermic than that of calcite at ambient pressure which is consistent with the metastability of aragonite at room pressure (Fisher et al., 2000). The phenomenon regarding different sampling techniques and the possibility of spontaneous aragonite to calcite conversion is also discussed in literature (Gill et al., 1995) .

Figure 27 (a, b, c) and (d) shows representative high-resolution images at high-magnification of selected regions from Figure 25 and Figure 26 respectively. Selected clusters of aragonite are seen (a, b, c, d). Clusters extend up to ca. 15 nm diameter and the orientation of those ordered regions seems to vary considerably.

The birth of new dislocations during growth is essential for understanding of biomineral formation (Teng et al., 1998). Experiments with proteins isolated from the calcite region of the red abalone shell (Walters et al., 1997) suggest that the corners between different step edges result from a highly anisotropic step edge speed as a function of direction along the surface (Palocz et al., 1998). Organic material seems to bind non-specifically to the step edges and the terraces ( Smith et al., 2000)

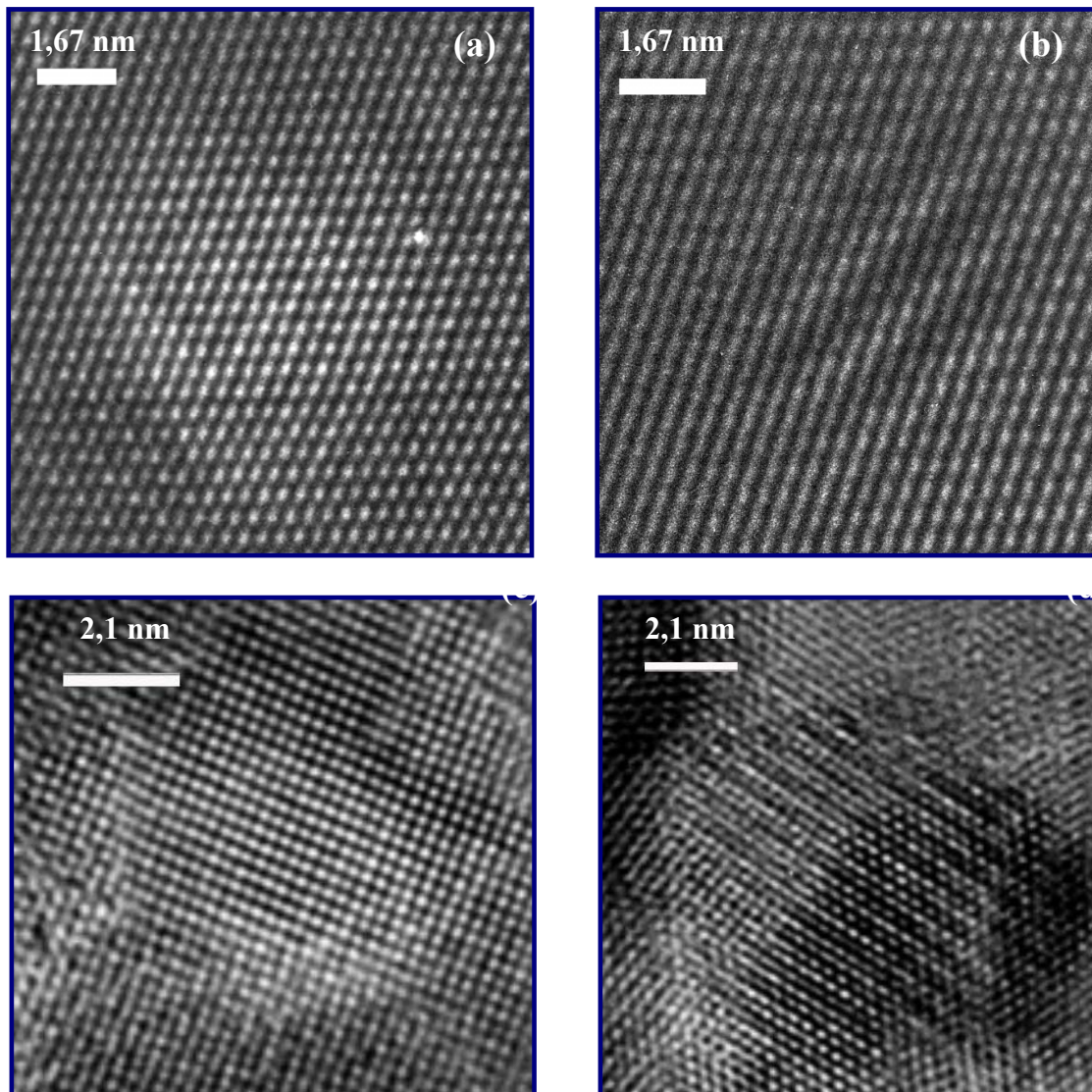


Figure 27: TEM high-resolution image of the smallest building units of aragonitic lamellae; (a) and (b) selected from Fig. 26 regions of aragonite clusters; (c) and (d) selected from Figure 25 regions of aragonite clusters.

From the TEM results, we can assume that such particles of about  $200 \text{ \AA}$  are the smallest regular components building the crossed lamellar structure of the studied specimen. Reorientation of such particles can cause disorder on a short length scale whereas the average orientation on a mesoscopic scale is preserved. Similar effects have been observed in minerals of the metamict state.

## **Chapter VII. Vibrational Spectroscopy**

### **1. Infrared and Raman Spectroscopy**

The Raman effect is an inelastic light scattering effect. In the experiment, an incident monochromatic laser light is focused on a sample. Some of this light may be transmitted or absorbed by the sample. The other part of the light is scattered. Some scattered light is elastically scattered, which is termed Rayleigh scattering, and the other which is inelastically scattered. This very minor component, of the order  $10^{-5}$  to  $10^{-6}$  of the scattered photons (Williams, 1995), forms the inelastic light spectrum. If the scattered light is analyzed using a spectrometer there occurs a strong central peak at  $E_0$ . This is the elastically scattered Rayleigh radiation. It undergoes no change in energy or wavelength. Weak satellite peaks at  $E_0 \pm h\nu_i$  are observed, representing the Raman scattering ( $h$  is the Planck's constant and  $\nu_i$  are the vibrational frequencies of the sample), i.e. the energy of the incident beam has been either raised or lowered ('shifted') by inelastic scattering and changes of the polarizability. The interactions correspond to the energy of the lattice vibrations. Hence the Raman spectrum for a sample is an expression of the atomic movements. Individual peaks of this spectrum may be ascribed to particular atomic displacements. Since the peaks are a function of the energy of the scattered photons they correspond to the energies of the vibrational transitions, or, the frequencies of its vibrational modes. The spectra that can be produced are dependent upon the interatomic forces operating in that molecule. A sensitive measure of the structure and bonding is provided by analysis of the position, symmetries and relative intensities of individual Raman modes.

The vibrational energies of crystals and molecules lie between  $0$ - $5000 \text{ cm}^{-1}$ . Routine analysis of minerals usually concerns those vibrations with frequencies between  $100$ - $1600 \text{ cm}^{-1}$ . For mineral containing  $\text{OH}^-$  group or water the range between  $1600$ - $3800 \text{ cm}^{-1}$  is also of interest. Raman spectroscopy is often compared with IR spectroscopy. The two techniques show many similarities (atomic vibrations) and crucial differences (symmetry behavior of modes).

Infrared absorption and Raman scattering are governed by completely different selection rules. Infrared bands arise from an interaction between light and the oscillating dipole moment of a vibrating molecule. Raman bands arise from an oscillating induced dipole caused by light waves interacting with the polarizability of a vibrating molecule. (It is common to describe the polarizability ellipsoid as the shape of the electron cloud around the

molecule). Thus, symmetric stretches, vibrations involving multiple bonds, and vibrations of heavier atoms typically give rise to strong bands in the Raman spectrum. Asymmetric molecules will have bands at similar frequencies in both the infrared and Raman spectra, but their relative intensities will be very different. In most cases, a chemical species will have strong, indicative bands in both its Raman and IR spectra but they may not coincide. Which technique is superior depends upon the molecule of interest, the concentration level, the matrix or solution, other interfering species present, and the desired sampling method. For many applications, Raman may be the better answer to the spectroscopic identification or monitoring needs basically, due to the higher resolution.

#### Advantages of Raman over IR spectroscopy (McMillan, P. 1989)

1. The energy of interest is generally  $10\text{-}4000\text{ cm}^{-1}$ , which presents experimental problems for IR spectroscopy, namely poor signal-to-noise ratio in the low energy range.
2. It is harder to focus with IR due to the large and varying wavelengths used in micro IR. It is very easy to focus using micro Raman. Much better spectral resolution in Raman spectroscopic measurements than in IR experiments when a microscope is used. They are also additional restrictions to apply IR microscopy to study vibrational modes below  $600\text{ cm}^{-1}$ .
3. Water is a strong absorber of IR which rules out IR spectra of water or species dissolved in it. Water presents no experimental problems in Raman experiments.
4. Raman spectral studies are less affected by powder particle sizes or shape.
5. In Raman studies the dimensions of the particles are large compared to the wavelength of the beam, ca.  $0.5\mu\text{m}$ , so spectra are essentially discrete lines.

#### Vibrational theory of molecules and crystals (McMillan, P. 1989)

There are essentially two ways of describing the theory that allows to produce vibrational spectra. The following are highly simplified summaries.

##### 1. Classical model

This is a well established mechanical model. It considers nuclei as point masses and the interactions between nuclei, the bonds, as springs that obey Hook's Law (the restoring force is directly proportional to the displacement, i.e. they are harmonic in time). Atoms can be vibrationally displaced about their equilibrium positions. Vibrational frequencies,  $\nu_i$ , of these

motions can be resolved from equations of motion for the system. Each of these frequencies corresponding to a particular atomic displacement; a normal mode of vibration.

## 2. Quantum mechanics model

This model was required because the classical model does not explain why vibrational spectra are line spectra and not continuous absorptions, neither does it describe the interactions of vibrations with light. Essentially, the model quantises vibrational energies and vibrational wave functions that describe each vibrational normal mode. The number of normal vibrations for a non-linear molecule is  $3N-6$ , where  $N$  is the number of atoms in the molecule. For crystals the number of normal modes are  $3N-3$ , where  $N$  is the number of the atoms in the primitive cell. The wave functions are determined by constructing differential equations using vibrational coordinates and an appropriate potential energy function and solving the resulting vibrational wave equation (McMillan, P.& Hoffmeister, 1988). Energy level diagrams are used to pictorially represent vibrational level transitions of the system as light (energy) is absorbed or emitted. Rayleigh scattering arises from transitions that start and finish at the same (vibrational) energy level, i.e. the ground state,  $v=0$ , where  $v$  is the vibrational quantum number. The sample is excited to a 'virtual' energy level where it decays with the release of a photon that has the original energy  $E_0$ . Stokes Raman scattering is caused by transitions from the ground state to some virtual energy level, decaying with the release of a photon with energy  $E_0-h\nu$ , to finish at a higher energy level, i.e.  $v=1$ . Anti-Stokes Raman scattering arises from the transition of molecules starting at an elevated energy level and finishing at a lower level with the release of a photon with energy  $E_0+h\nu$ . Since at 'normal' temperatures most vibrations are at the ground state Stokes transitions are far more likely to occur than anti-Stokes and will result in far more intense Stokes Raman scattering. That is why Stokes Raman scattering is routinely analysed.

## Crystal lattice vibrations

Although the number of vibrational modes for a molecule is  $3N-6$  most of these are not seen in the Raman or IR spectrum, i.e. they are not Raman- or IR-active. When a molecule is fixed in a crystallographic site in a crystal, the selection rules of its internal vibrations are different. For crystals,  $N$  may be very large. Lattice vibrations may be longitudinal (LO) or transverse (TO) and can be considered as displacive waves travelling

through the crystal, the nuclear displacements being parallel or perpendicular to the direction of propagation respectively. Displacement of nuclei cause oscillatory dipole moments in the electric field/cloud, the magnitude of which is related to the ease of deformation of the cloud, the molecular polarizability. Easily polarized atoms such as S, Ti and I display strong peaks. Si, C and O are less easily polarized. For light to interact with a lattice vibration, and be Raman active, the wavelengths must be comparable. For Raman experiments this is typically in the blue/green region of visible light. However, since wavelengths of these magnitudes are of order greater than the dimensions of the crystalline unit cells, only very long wavelength lattice modes can interact in Raman experiments. The unit of crystal lattice vibrational excitation is the phonon, analogous to the photon.

Summarized the main areas of study of the vibrational spectra of minerals.

The carbonate minerals with the general formula  $MCO_3$  include the double and single carbonates where  $M = Ca, Ba, Mg, Fe, Mn$  and  $Sr$ . They exhibit a range of structures but share the isolated  $CO_3^{2-}$  group. The vibrational spectra of this ion is well documented and has 6 vibrational modes. These comprise internal vibrations of the ion and external modes (lattice modes) of the carbonate group and vibrations of the metal cation. The peak positions of these modes are quite well constrained. Regions thus far delimited relate to symmetric and asymmetric stretching, in-plane and out-of-plane bending plus some of the overtones. Calcite and aragonite spectra are completely determined (McMillan and Hoffmeister, 1988).

While both infrared and Raman spectroscopy represent useful techniques for characterizing bonding environments, vibrational mode frequencies and the molecular species present within minerals, infrared spectroscopy has been extensively utilized as a quantitative technique for determining the concentration and speciation of volatile components within samples (Williams, Q., 1995).

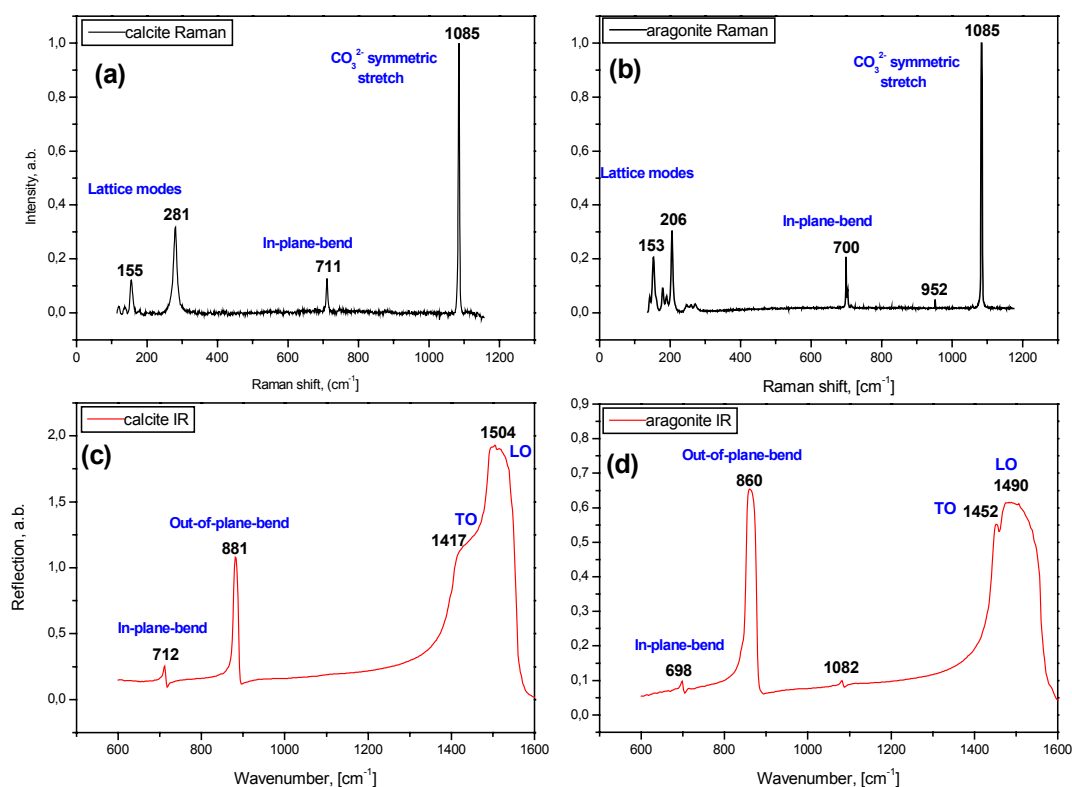


Figure 33: IR unpolarized reflection spectrum of single crystals calcite (a) and aragonite (b), and Raman spectra of single crystals calcite (c) and aragonite (d).

Representative Raman spectra of calcite are shown in Figure 33 (a), along with an unpolarized infrared reflectance spectra of calcite (c). For calcite, such an analysis predicts five Raman active vibrations (one  $A_{1g}$ , and four doubly degenerate  $E_g$  symmetry modes) and eight infrared-active vibrations ( $3A_{2u}$  and 5 doubly degenerate  $E_u$ ). The infrared asymmetric stretching and out-of-plane bending vibrations of the carbonate group occur near 1417 and 880  $\text{cm}^{-1}$ ; Moreover, the LO-TO splitting of the asymmetric stretching vibration of the carbonate group is clearly visible in the reflectance spectrum. Within the Raman spectrum, the most intense vibration of calcite is the symmetric stretching vibration of the carbonate group at 1085  $\text{cm}^{-1}$ . At lower frequency (below 400  $\text{cm}^{-1}$ ), the spectrum of the carbonate has Raman bands associated with external vibrations of the carbonate group relative to stationary calcium ions. At lower frequencies that are shown in Figure 33 (c) in the infrared spectrum, both lattice-type vibrations of the calcium ions relative to the carbonate groups and displacements of the carbonate groups and the calcium ions both against and parallel to one another occur.

## 2. Infrared and Raman Spectra measurements

### 2.1. Polarized IR spectra

Polarized IR-spectra were recorded using a Bruker IFS 55 spectrometer equipped with a microscope and a KRS-5 polarizer; the beam diameter was about 40  $\mu\text{m}$ .

### 2.2. Polarized Raman spectra

Raman measurements were carried out using a triple monochromator system (Jobin-Yvon T64000) equipped with an Olympus BH2 microscope. The spectra were collected in back-scattering geometry using the 514.5 nm line of an  $\text{Ar}^+$  ion laser and a laser beam power on the sample surface of 10 mW. The diameter of the laser spot on the sample surface was approximately 1.6  $\mu\text{m}$ . The spectral resolution achieved was about 2  $\text{cm}^{-1}$ . Polarized Raman spectra were collected of a lateral section of the shell of *Patella crenata*.

Some of the samples were measured using a Raman spectrometer HR800, ( Jobin Yvon Horiba, France ) equipped with a Microscope BX40, (objective 50x ) and a CCD detector. The spectra were collected in back-scattering geometry using illumination of 632.8 nm line of HeNe laser and a laser beam power on the sample surface of 20 mW ; polarized 500:1. The diameter of the laser spot on the sample surface was approximately 2.4  $\mu\text{m}$ . The spectra of calcite ranges from 100-1790  $\text{cm}^{-1}$  and of aragonite from 100 - 1750  $\text{cm}^{-1}$ . Polarized Raman spectra of *Patella crenata* were collected.

## 3. Results and discussion

The vibrational spectra of calcite and aragonite crystals are markedly different, although both have the same composition. This result can be explained if we consider the difference in site symmetry of the  $\text{CO}_3^{2-}$  ion. To analyse the spectra, it is necessary to carry out the site group of factor group analysis. Calcite crystallizes with rhombohedral symmetry in space group  $R\bar{3}c$  and aragonite is orthorhombic with space group *Pn*cm. Group theoretical analysis of vibrational excitations are well known for both materials. (Nakamoto, 1986). According to X-ray analysis, the space group of calcite is  $\text{D}_{3d}^6$  and Z is two. The site symmetry of  $\text{CO}_3^{2-}$  ion in calcite is  $\text{D}_3$ . The space group of aragonite is  $\text{D}_{2h}^{16}$  and Z is four. The site symmetry of  $\text{CO}_3^{2-}$  ion in calcite is  $\text{C}_s$ .

In the case of calcite there are three internal modes ( $\text{A}_{2u}$  and two  $\text{E}_u$ ), three translatory modes ( $\text{A}_{2u}$  and two  $\text{E}_u$ ), and two rotatory modes ( $\text{A}_{2u}$  and  $\text{E}_u$ ) are infrared active, and three

internal modes ( $A_{1g}$  and two  $E_g$ ), one translatory mode ( $E_g$ ), and one rotatory mode ( $E_g$ ) are Raman active.

Vibrational representations for aragonite are:

$$\Gamma_{\text{active}} = 9A_g + 6B_{1g} + 9B_{2g} + 6B_{3g} + 8B_{1u} + 5B_{2u} + 8B_{3u} ;$$

$$\Gamma_{\text{inactive}} = 6A_u ;$$

$$\Gamma_{\text{acoust}} = B_{1u} + B_{2u} + B_{3u}.$$

Representations of calcite are:

$$\Gamma_{\text{active}} = A_{1g} + 4E_g + 3A_{2u} + 5E_u ;$$

$$\Gamma_{\text{inactive}} = 3A_{2g} + 2A_{1u} ;$$

$$\Gamma_{\text{acoust}} = A_{2u} + E_u.$$

Infrared and Raman spectroscopic studies reveal both the presence of aragonite and calcite (Figure 36, 38), which vary in their distribution within the bulk of the shell as seen by naked eye (Figure III- 1) or optical microscope (Figure IV-1). In the Raman spectra of the shell of *Patella crenata* (Figure 38) recorded in the range 100-1800  $\text{cm}^{-1}$  aragonite signals can be distinguished from the excitations of calcite (Salje and Viswanathan 1976). Also from the IR spectra in the range 600-1700  $\text{cm}^{-1}$  (Figure 36) both biominerals can be distinguished.

### 3.1. IR spectroscopy

The IR bands due to  $(\text{CO}_3)^{2-}$  vibrations in  $\text{CaCO}_3$ , display maxima near 1480  $\text{cm}^{-1}$  ( $E_u$ ) and 890  $\text{cm}^{-1}$  ( $A_{2u}$ ). The former is due to the transverse optic (TO) component of the antisymmetrical stretching mode in the  $ab$  plane ( $\nu_a(\text{CO}_3)^{2-}$ , see Figure 34), whereas the latter corresponds to the longitudinal optic (LO) component of the out-of-plane mode (for  $\vec{E} // c$ -axis) (denoted  $\delta_s(\text{CO}_3)^{2-}$ , see Figure 34). The  $A_{2u}$  vibration of calcite near 880  $\text{cm}^{-1}$  (out-of-plane vibration) occurs at higher energies than the related vibration of aragonite (Figure 36). Near 710  $\text{cm}^{-1}$  we observe the antisymmetrical bending mode  $E_u$  in the  $ab$  plane of the carbonate group (denoted  $\delta_a(\text{CO}_3)^{2-}$ ). The absorption bands are listed in Table 1 and assigned according to previous work (Farmer 1974; Decius and Hexter 1987).

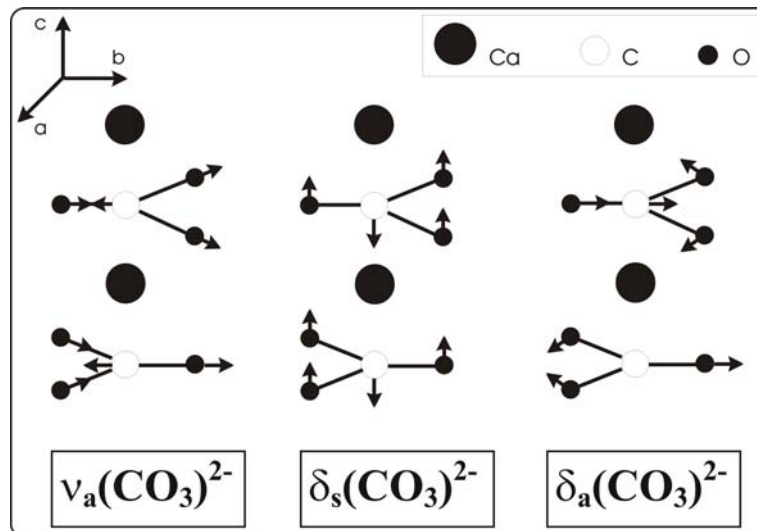


Figure34: Vibrational modes of the carbonate group ( $\text{CO}_3^{2-}$ ), after Farmer (1974).

**TABLE 1.** Vibrational assignment and direction of the transition moments  $M$  for the different IR absorption bands observed in calcite (Farmer 1974; Decius and Hexter 1987):

Observed frequency ( $\text{cm}^{-1}$ )	Assignment and orientation of transition moment $M$ (see also Fig. 34)
1500	$\nu_a(\text{CaCO}_3)^{2-}$ : antisymmetrical stretching, $M$ in $ab$ plane
880	$\delta_s(\text{CaCO}_3)^{2-}$ : out-of-plane bending, $M$ along $c$
710	$\delta_a(\text{CaCO}_3)^{2-}$ : antisymmetrical bending, $M$ in $ab$ plane

### 3.1.1. Unpolarized IR spectra

Unpolarized IR reflection spectra of aragonitic material (Figure 35) show shifted bands compared with excitations in calcite. The aragonite have out-of-plane bending  $\delta_s(\text{CaCO}_3)^{2-}$  at  $860 \text{ cm}^{-1}$  and calcite near  $880 \text{ cm}^{-1}$ . The broad excitation band in the calcitic lamellae consists of two components, namely an excitation near  $1500 \text{ cm}^{-1}$  corresponding to the longitudinal optic (LO) mode and a signal near  $1400 \text{ cm}^{-1}$  corresponding to the transverse optic (TO) mode of  $\nu_a(\text{CO}_3)^{2-}$ . The splitting may be caused by the long-range polarisation field in calcite.

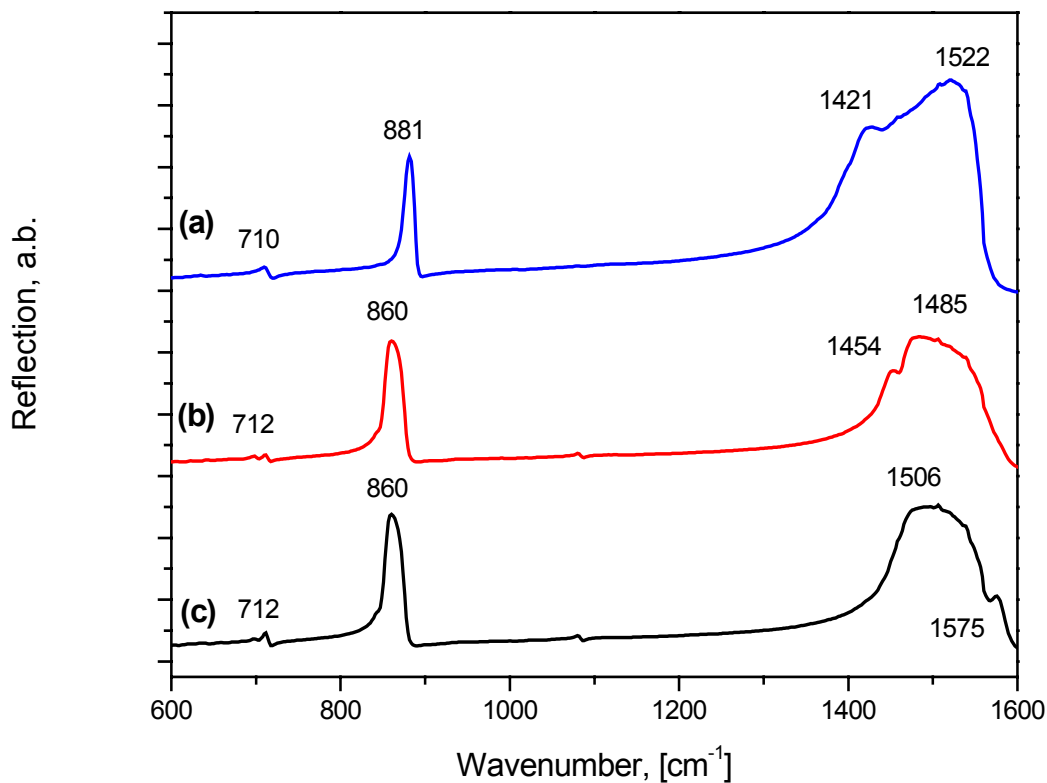


Figure 35: IR spectra from (a) calcitic outer layer, (b) aragonitic myostracum and (c) aragonitic hypostracum.

### 3.1.2. Polarized IR spectra.

Polarised IR spectra were collected within one calcite lamella and are displayed in Figure 36 cross section and Figure 37 lateral section. The (a) lines show the IR reflection spectrum with the field vector  $\vec{E}$  perpendicular to the bright and dark lamella. A high intensity for the band near  $880\text{ cm}^{-1}$  and a weaker signal at  $1500\text{ cm}^{-1}$  are observed when  $\vec{E}$  is parallel to  $c$ -axis. For the (b) lines the field vector  $\vec{E}$  is parallel to the bright and dark lamella direction. The signal near  $890\text{ cm}^{-1}$  vanishes for this orientation of  $\vec{E}$  and the broad band near  $1500\text{ cm}^{-1}$  shows increased intensity.

The both sections investigated by polarized infrared spectroscopy indicate an orientation of the crystallographic  $c$ -axis. The  $c$ -axis runs preferentially perpendicular to the lamellae border.

Those observations indicate that the orientation of  $c$ -axis is the result of the summation from superimposed signals of layered nanocrystals (Fig. 3, 5).

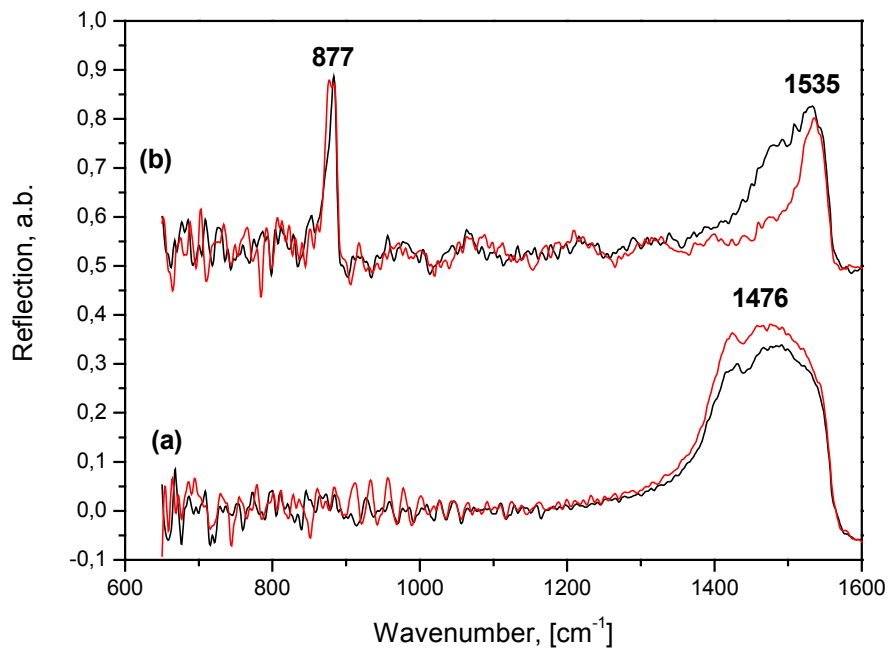


Figure 36: Polarized IR spectra from a cross section of calcitic lamellae. The black line are the measurements of the dark lamella and the red of the bright lamella. (a) polarization parallel to the lamellae and (b) polarization perpendicular to the lamellae.

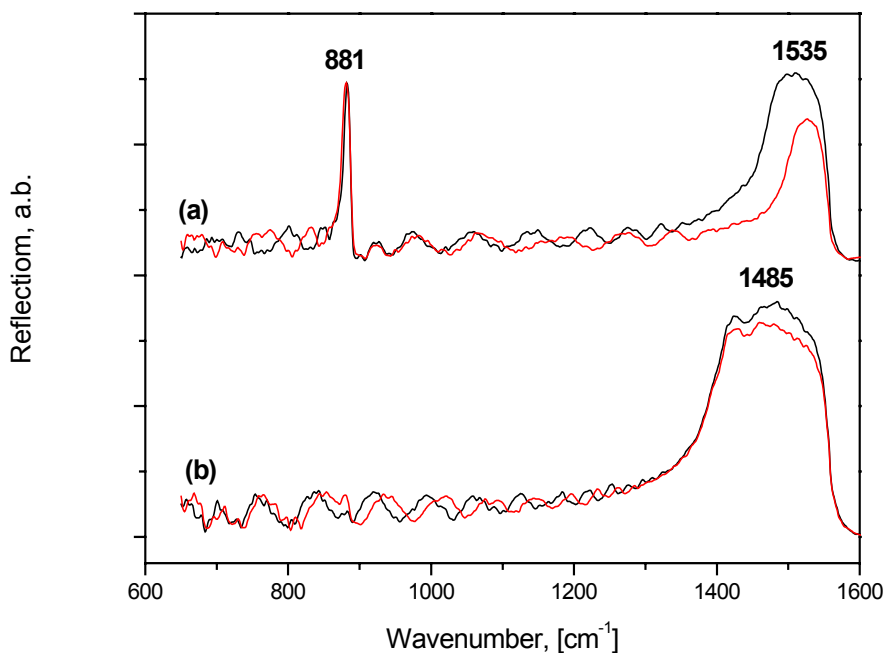


Figure 37: Polarized IR spectra from the lateral section of the calcitic lamellae. Black lines are measurements of dark lamella and the red of the bright lamella. (a) polarization parallel to the lamellae and (b) polarization perpendicular to the lamellae.

### 3.2. Raman Spectra

The layers in the shell of *Patella crenata* were identified by Raman scattering as alternating bands of calcite and aragonite minerals (Fig. 38). The Raman spectra from calcite (Fig. 38(b)) can be distinguished clearly from the aragonite Raman spectra (Fig. 38(a)) in the region 100-300  $\text{cm}^{-1}$ . All Raman spectra shown are normalized to the intensity of the  $A_{1g}$  mode (the peak at 1085  $\text{cm}^{-1}$  arising from the symmetric stretch of the  $\text{CO}_3^{2-}$ ). Therefore comparing the intensity of a certain peak, measured in different scattering geometry we compare actually the intensity ratio between this peak and the peak at 1085  $\text{cm}^{-1}$ .

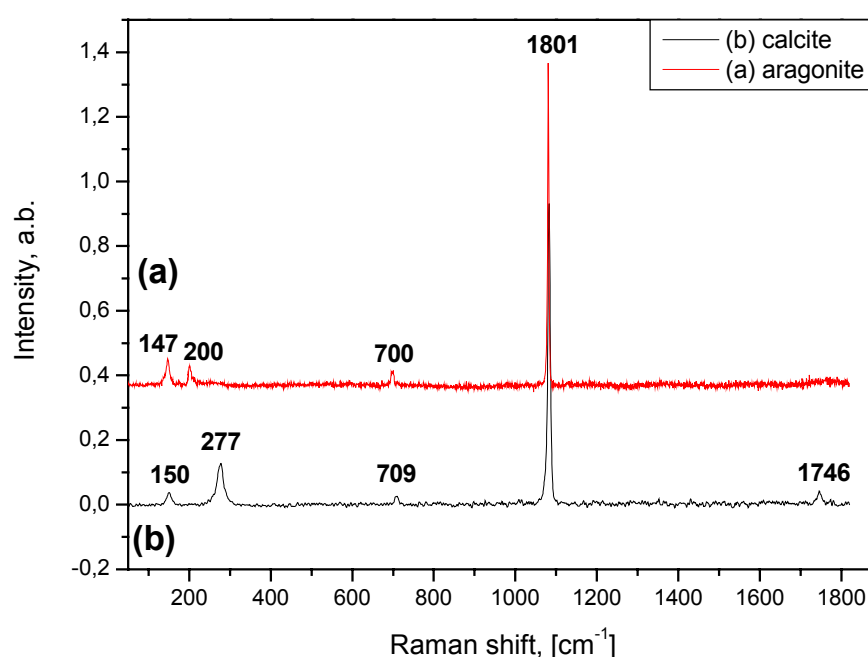


Figure 38: Raman spectra of (a) aragonitic hypostracum, (b) calcitic layer.

#### 3.2.1. Aragonite

Figure 39 shows Raman spectra obtained from different locations of aragonitic crossed lamellae: from strontium (Sr) enrichment (red line) and between the Sr-containing areas (black line) (area 3 in the Fig. 5). The spectra are normalized to the 1084  $\text{cm}^{-1}$  peak intensity.

The ratio of the integrated intensities of the band near 852  $\text{cm}^{-1}$  (typical of a  $c$  axis of aragonite perpendicular to the Sr-containing line) and of the band at the 1084  $\text{cm}^{-1}$  symmetric stretching vibration of the carbonate group (Weiss, 2002), shows weak deviation of the

average value of the  $c$ -axis of the material between the Sr-containing areas and that of the strontium (Sr) poor area.

In addition the Raman spectra collected from the Sr-containing strip (Fig. 39, (b)) shows a weak shift in frequency of the symmetric stretching mode of the carbonate group ( $1084\text{ cm}^{-1}$ ). The absolute value of the frequency is very small, but it is within the experimental accuracy. Such frequency shift is not observed for the other peaks, so it could not be an experimental artifact. Such frequency change of the  $\nu_a(\text{CO}_3)^{2-}$  mode should be related to the presence of Sr. The radius of the strontium cation  $\text{Sr}^{2+} = 132\text{ pm}$  is larger than that of the  $\text{Ca}^{2+} = 114\text{ pm}$ . Hence, one can assume that Sr-O interactions are stronger than Ca-O interactions. This should lead to a slight decrease in the C-O stretching force constant of  $\text{CO}_3$  groups surrounded by Sr.

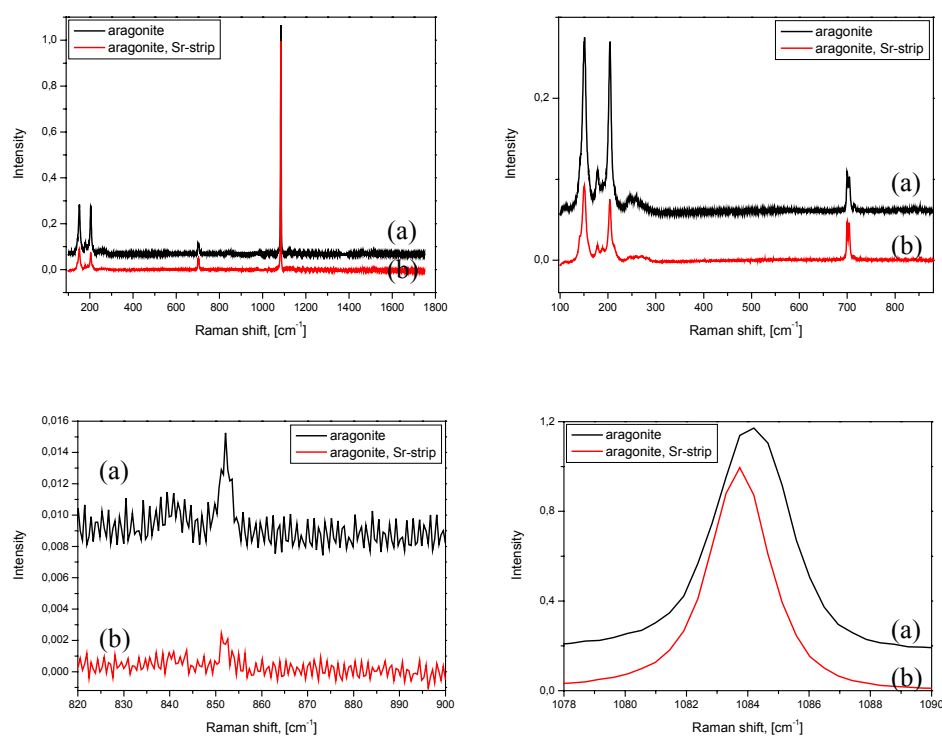


Figure 39: Raman spectra of aragonite cross lamellae normalized to the same  $1084\text{ cm}^{-1}$  peak height. (b) Raman spectrum obtained from the Sr-containing area, (a) Raman spectrum obtained between the Sr-containing areas.

The integrated intensities of the bands at  $152$  and  $205\text{ cm}^{-1}$  which are due to the external translational lattice modes of the carbonate ion (Weiss, 2002) in the spectrum of Sr-containing areas are lower than those in the spectrum of the aragonitic crossed lamellae. Hence, the preferred orientation of the crystallographic  $c$ -axis in the Sr-containing areas differs from that

in the crossed lamellae. This is in accordance with observations by SEM (Fig. 22) where the Sr-rich layer runs across the aragonitic lamellae of first order. This layer has a different orientation in comparison with aragonitic lamellae of first order.

### 3.2.1. Calcite

Polarized Raman spectra often provide more information about the symmetry properties of normal vibrations than polarized infrared spectra (Nakamoto, 1986).

Parallel polarised Raman spectra ( $\vec{E}_i // \vec{E}_s$ , where  $\vec{E}_i$  is the electric field vector of the polarized light and  $\vec{E}_s$  is the electric field vector of the polarized scattered light) were collected from different regions in the thin section. Comparison between the peak intensity ratios in the spectra collected from the centre and from the border of a selected calcite lamella shows that the orientation of the crystallographic *c*-axes in the two regions is only slightly different (Figure 40 and 41). The Raman signal was collected from smaller areas as compared with IR measurements which allowed to estimate local deviations of the crystal orientation.

A weak difference in the intensity ratios is found between the dark and the bright areas of the calcitic lamellae. This is probably due to the orientational difference of the crystallites but also weak chemical variations may influence the scattering intensities.

In Figure 40 the red line yields the intensity ratios at the border of the lamella.

$$I_{150-280} / I_{1085} = 3,06413 / 7,78566 = 0,39356$$

$$I_{711} / I_{1085} = 0,766557 / 7,78566 = 0,09833$$

The black line yields the intensity ratios at the centre of the lamella.

$$I_{150-280} / I_{1085} = 2,28323 / 7,53389 = 0,3031$$

$$I_{711} / I_{1085} = 0,61345 / 7,53389 = 0,08143$$

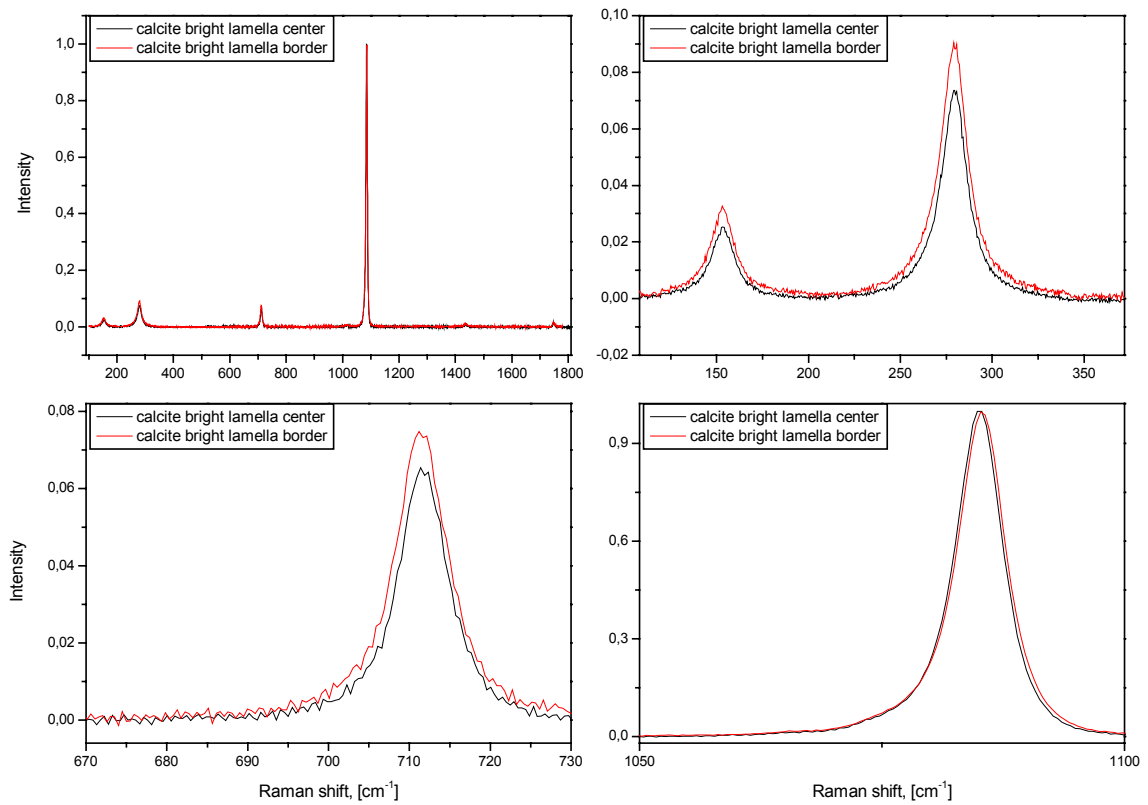


Figure 40: Parallel polarized ( $\vec{E}_i // \vec{E}_s$ ) Raman spectra of calcite at the border and the centre of a bright lamella.

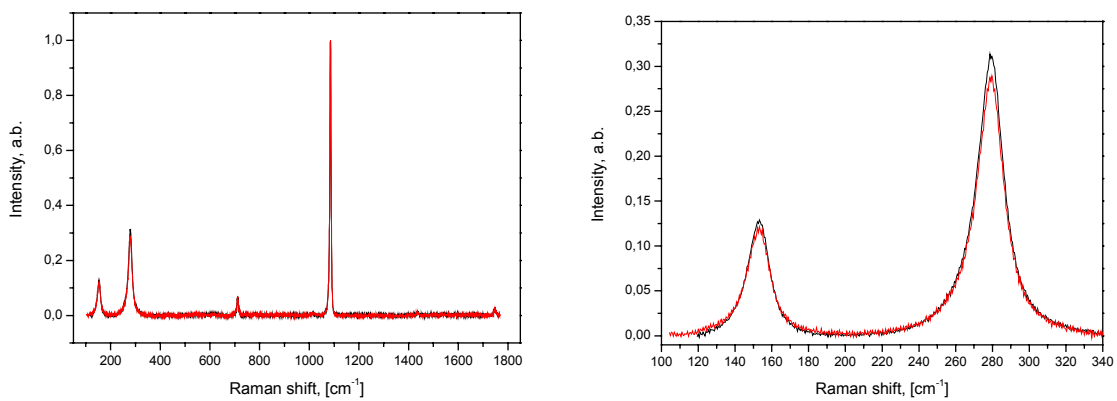


Figure 41: Parallel polarized ( $\vec{E}_i // \vec{E}_s$ ) Raman spectra of calcite at the border and the centre of a dark lamella.

Parallel polarised ( $\vec{E}_i // \vec{E}_s$ ) Raman spectra were also collected from the lateral section in the calcitic lamellae, when the orientation of the scattering in the dark lamella was oriented parallel or perpendicular to the direction of the lamellae.

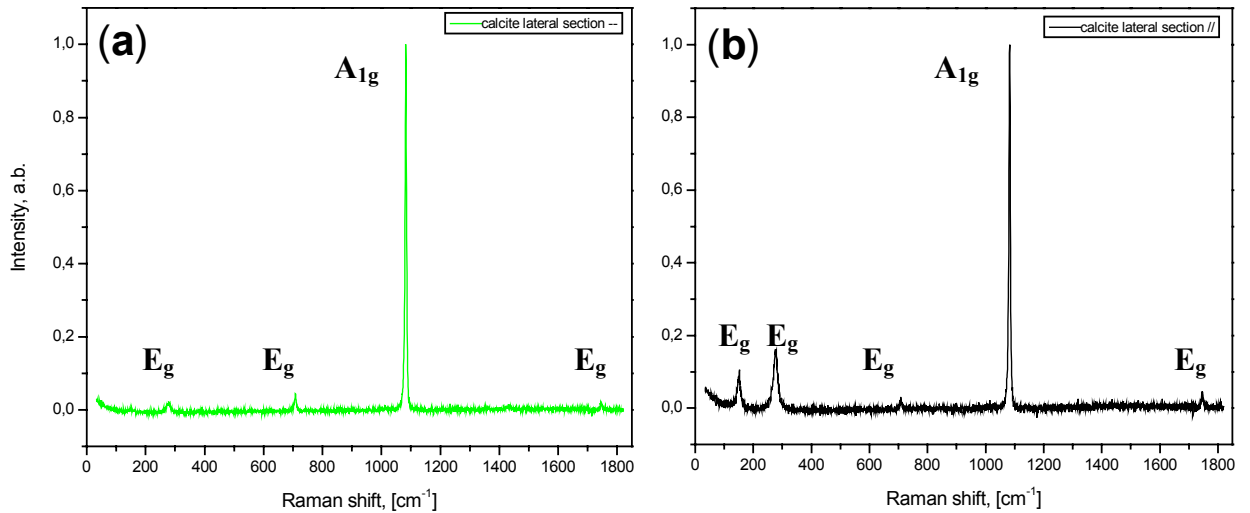


Figure 42: Parallel polarized ( $\vec{E}_i // \vec{E}_s$ ) Raman spectra from the lateral section of the calcitic lamellae. Dark lamella (a) perpendicular to the polarization, (b) parallel to polarization.

For calcite the A<sub>1g</sub> mode has non-zero  $\alpha_{xx}$ ,  $\alpha_{yy}$ , and  $\alpha_{zz}$  components of the polarizability tensor, whereas for E<sub>g</sub> modes only  $\alpha_{xx}$  and  $\alpha_{yy}$  are non-zero components. As seen in Figure 42 (a) the intensities of the peaks generated from E<sub>g</sub> modes are much weaker when the lamellae were oriented perpendicular to the incident light polarization ( $\vec{E}_i$ ) (Fig. 42 (b)).

We use four scattering geometries of the two polarizers to study the relationship between the crystal orientations in the dark and bright calcitic lamellae in the shell of *Patella crenata*. Figure 43 and 44 show polarized Raman spectra respectively from dark and bright lamellae. The scattering geometries are given in the figures caption.

In the case of a perfect oriented single crystal of calcite, only E<sub>g</sub> species is seen in the crossed polarized spectra. As seen in Figure 43, the A<sub>1g</sub> mode also appears in the crossed polarized spectra of the dark lamella (Figure 43 (b) and (c)). Therefore, the crystallites in the biomineral in the dark lamella are not perfectly oriented with respect to the lamellae border. However, there is a large difference in the intensities of the external E<sub>g</sub> modes at 155 and 280 cm<sup>-1</sup> measured in parallel and crossed polarized spectra. In addition, the Raman intensities of

the  $E_g$  modes in the parallel polarized spectrum measured when the lamella is perpendicular to  $\vec{E}_i$  is almost zero.

Comparing the parallel polarized Raman spectra of the thin section (Fig. 43 (a) and (d)) with those of the lateral thin section (Fig. 42) the same behaviour occurs. This is in agreement with infrared investigations (Fig. 36 and 37) where the polarised spectra collected from, crossed and lateral sections are identical.

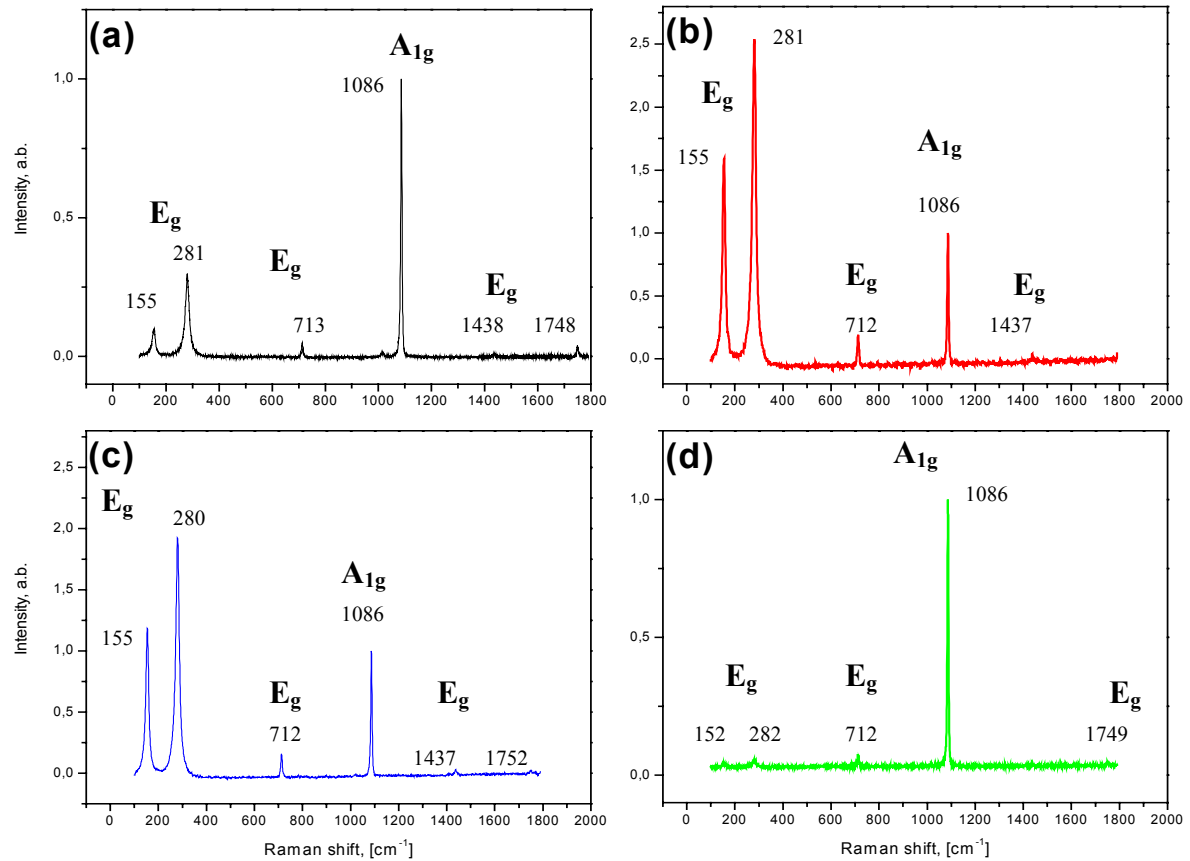


Figure 43: Polarized Raman spectra from dark calcitic lamellae. (a) parallel polarization ( $\vec{E}_i // \vec{E}_s$ ) parallel to the lamellae, (b) crossed polarization  $\vec{E}_i$  is parallel and  $\vec{E}_s$  is perpendicular to the lamellae, (c)  $\vec{E}_i$  is perpendicular and  $\vec{E}_s$  is parallel to the lamellae, (d) parallel polarization ( $\vec{E}_i // \vec{E}_s$ ) is perpendicular to the lamellae.

Raman measurements were performed at differed scattering geometries also for the bright lamella (Figure 44). Only slightly differences in the intensities of the external  $E_g$  modes (lattice mode) at 155 and 280  $\text{cm}^{-1}$  for different scattering geometry occur. This can be explained by the different orientation of the calcite crystals in the lamellae. The dark lamella indicates an orientation of the crystallites with their  $c$ -axis almost perpendicular to the lamella

border, while the bright lamella indicates Raman signals due to very small crystallites orientated almost randomly. However, the parallel polarised spectra measured when the bright lamella is perpendicular or parallel to the incident light are not identical. The intensities of the  $E_g$  peaks at 155 and 280  $\text{cm}^{-1}$  are lower in the spectra (d) than in the spectrum (a). In addition, the intensity of the peak at 711  $\text{cm}^{-1}$  in the cross polarized spectrum (b) is higher than that in the parallel polarized spectrum (a). This indicates that to some extent preferential ordering of the crystals occurs also in the bright lamella. However, the degree of the orientational ordering for the bright lamella is much lower than that for the dark lamella.

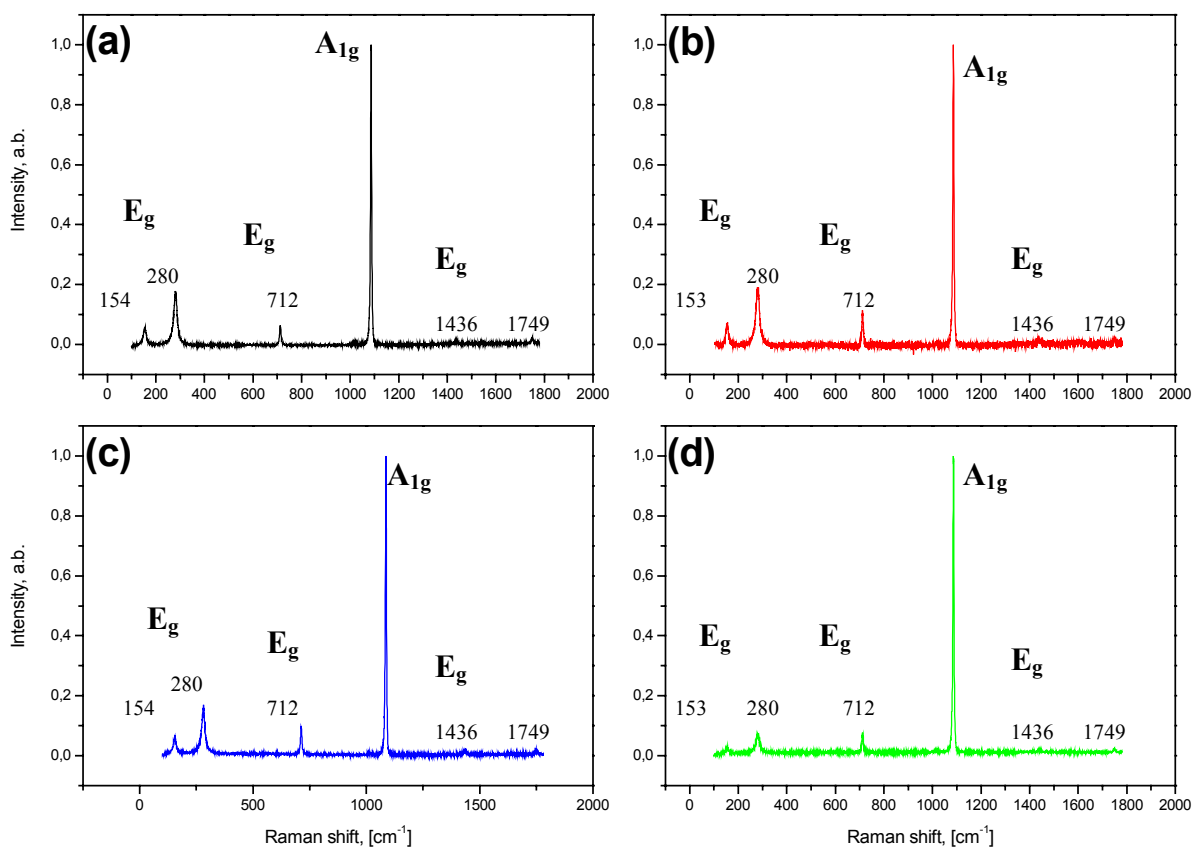


Figure 44: Polarized Raman spectra from the cross section of the bright calcitic lamellae. (a) parallel polarization ( $\vec{E}_i // \vec{E}_s$ ) parallel to the lamellae, (b) crossed polarization  $\vec{E}_i$  is parallel and  $\vec{E}_s$  is perpendicular to the lamellae, (c)  $\vec{E}_i$  is perpendicular and  $\vec{E}_s$  is parallel to the lamellae, (d) parallel polarization ( $\vec{E}_i // \vec{E}_s$ ) is perpendicular to the lamellae.

## **Chapter VIII. Composition and Distribution of Chemical Elements in the Shell**

A number of microbeam techniques have been developed for the analysis of geological materials. There are two destructive techniques like laser-ablation inductively-coupled plasma mass spectrometry (ICP-MS), which uses incident pulsed laser light to volatilize material from the sample, and ion microprobe analysis (SHRIMP) which uses low-energy ions to ablate the sample. Nondestructive techniques are more common. Micro X-ray fluorescence analysis uses an incident X-ray beam to excite characteristic X-rays from the sample. Electron microprobe analysis (EMP), scanning electron microscopy (SEM), and cathodoluminescence microscopy utilize a focused electron beam to produce characteristic X-rays, secondary electrons, and visible light, respectively, from the sample. Proton induced X-ray emission (PIXE) analysis uses a focused beam of high-energy protons to produce characteristic X-rays from the sample.

### **1. Proton Induced X-ray Emission (PIXE)**

A high energy (a few MeV) proton beam is directed onto the sample. The protons cause electrons within the atoms of the target to be excited from core shells. The X-rays emitted when electrons fall back into the core hole can be used to identify each element within the sample. Scanning the proton beam across the surface enables maps of the concentration of each element to be acquired. X-ray is detected by Si(Li) detector. An advantage of PIXE compared to other methods is the speed and sensitivity. Like other spectroscopic techniques used for elemental analysis, PIXE is based upon the physics of the atom involving the excitation of the atoms in the sample to produce characteristic X-rays. It is independent of the type of chemical bonding.

In order to identify and quantify the produced X-ray intensities, known standards are used in conjunction with computer software to establish sensitivities for each element. The X-ray spectrum is initiated by irradiating a sample with a proton beam produced by an accelerator from pure Hydrogen. When a sample is irradiated with the proton beam, the protons interact with the electrons to create inner-shell vacancies in the atoms present in the sample material. The energies of the X-rays emitted upon filling the vacancies are characteristic of the elements from which they originate. The number of X-rays of certain energy is proportional to the mass of the corresponding element found in the sample. A Lithium drifted Silicon

detector is used for data acquisition, allowing for the simultaneous analysis of the elements from Sodium to Uranium. Data reduction is then accomplished using computer software which normalizes the detected sample X-ray intensities against those measured from pure standards for each element. Thus, elements are easily identified and quantified. Proton Induced X-ray Emission (PIXE) has the advantage of a much improved signal/noise ratio when compared to electron induced X-rays. PIXE is sensitive to impurities in the ppm range and requires no particular sample preparation.

### **1.1 PIXE equipment**

Elemental composition of a cross-section of the lamellar aragonitic region is studied by micro-PIXE technique with the nuclear microprobe system at the Forschungszentrum Rossendorf (FZR), Dresden, Germany (Herrmann and Grambole, 1995). A beam spot of ca. 5  $\mu\text{m}$  (beam current of ca. 1 nA) is chosen for line scans and maps. The beam of 3 MeV protons hits the sample perpendicularly. The scanned area was 1.15 x 1.25 mm in 9  $\mu\text{m}$  intervals across the section. The step corresponds to those described by Markwitz et al. (2000). The proton beam was focused to ca. 5  $\mu\text{m}$  in diameter and PIXE analysis is made across the aragonite layers of the shell of *Patella crenata*. The 2-D target area of the shell cross-section of aragonite was a ca. 60  $\mu\text{m}$  thick section mounted on glass in strontium (Sr)-free resin.

### **1.2 Results and discussion**

Bright lines in the aragonitic hypostracum with inner crossed lamellar structure are seen under the polarizing microscope (Fig. 5, region 3). Those lines do not depend on the age of the individual *Patella crenata* sample. In order to clarify their origin, elemental composition and distribution are studied in a thin section of aragonite.

The layers in the shell of *Patella crenata* are identified by Raman scattering as alternating bands of the calcite and aragonite mineral forms of calcium carbonate (chapter VII). The differences in the unit cell structure of calcite and aragonite favor different trace elements in the two minerals. As known, aragonite is iso-structural with Strontianite ( $\text{SrCO}_3$ ) and calcite is iso-structural with Magnesite ( $\text{MgCO}_3$ ) (Mason and Bery, 1968). As a result strontium (Sr) substitution should be favoured in the aragonite layers and is practically excluded from the calcite layer (remains in the range of the background). The same is valid for magnesium (Mg) which is practically excluded from the aragonite layers.

Figure 45 and Figure 46 represent PIXE calcium (Ca) and PIXE strontium (Sr) distribution maps of a 2-D cross-section of aragonite layer (Fig. 5, region 3). The pictures show distinguished boundaries reflecting the inverse occurrence of (Sr).

The calcium (Ca) map (Figure 45) does not show any observable changes in the calcium (Ca) density distribution.

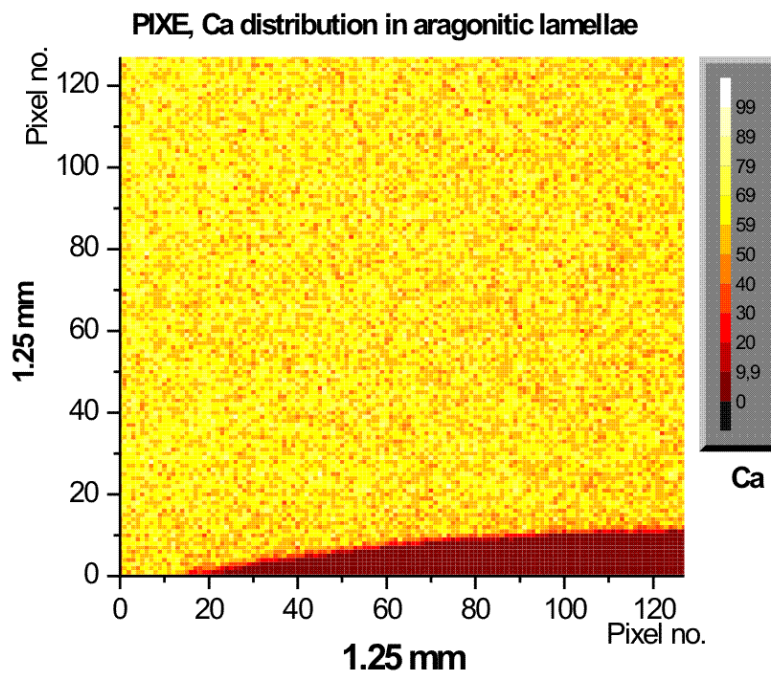


Figure 45: PIXE calcium (Ca) distribution map (in pixel no) of 2D cross section of aragonite of the *Patella crenata* shell.

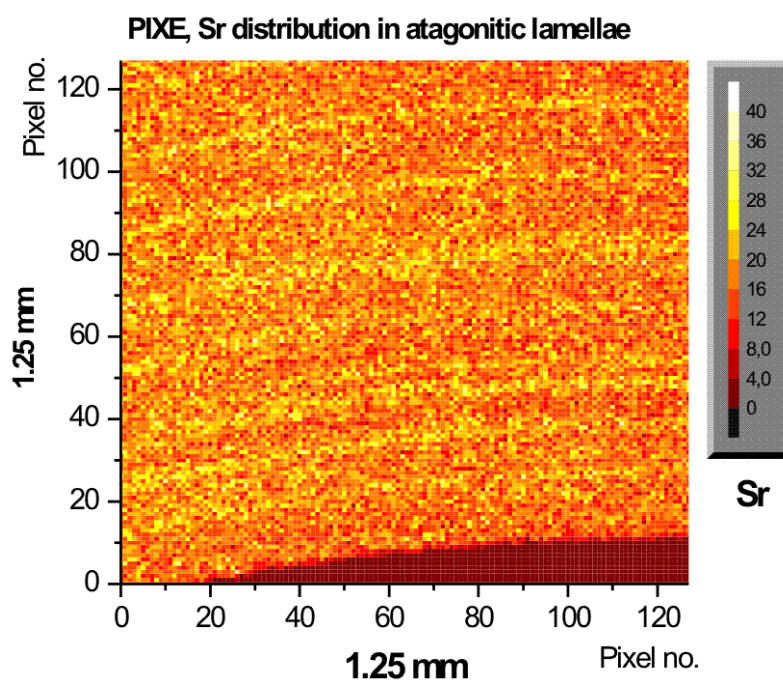


Figure 46: PIXE strontium (Sr) map (in pixel no.) of 2D cross section of aragonite of the *Patella crenata* shell.

We observe that the bright lines seen in Figure 5 (region 3) contain higher concentrations of Sr compared with the broad dark areas. The PIXE strontium (Sr) mapping (Figure 46) shows (Sr) peaks displayed as curved strips. The measured distances between the (Sr) areas are in the range of 150 to 250  $\mu\text{m}$  and the thickness of the Sr-lines is about 50  $\mu\text{m}$ .

Figure 47 (a) shows strontium density changes along the width of Sr areas measured at 64 points perpendicular to the strontium line of Figure 46, as well as Sr density changes along one strontium line, namely at 80 points parallel to the Sr line of in Figure 46.

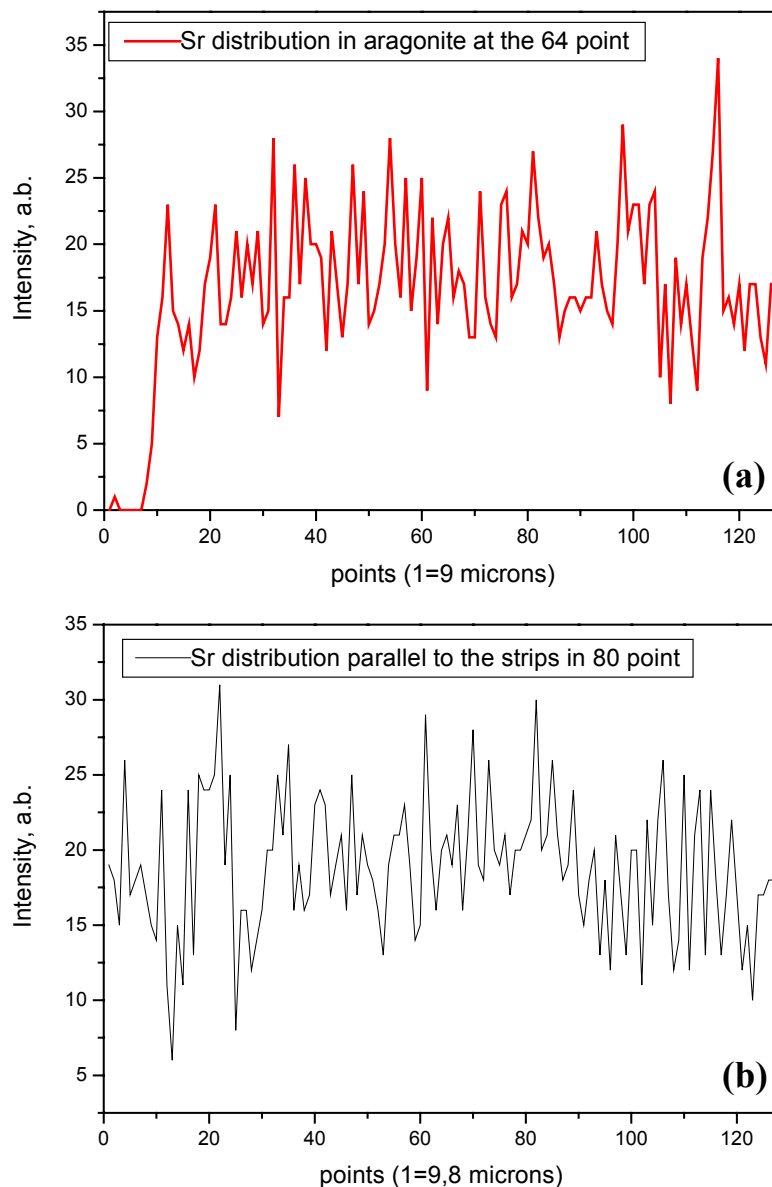


Figure 47: Strontium (Sr) density changes;  
(a) along the width of the (Sr) lines;  
(b) along the (Sr) line;

## **2. Electron Microprobe Analysis (EMPA) investigation**

The electron microprobe analysis is a commonly applied technique in material analysis. In addition to characteristic X-rays, most microprobes are equipped to analyse other effects produced by electron bombardment of a sample, including backscattered electrons, secondary electrons, and cathodoluminescence.

### **2.1. Electron Microprobe Analysis (EMP) equipment**

The absolute values of the chemical composition are determined using a CAMECA, SX100 Electron Microprobe (EMP) Analyzer. An EMP uses a beam of focused electrons to excite X-rays from a small area of a polished sample. Low-energy electrons are produced from a tungsten filament and accelerated by a positively biased anode plate to 10-30 thousand electron volts (keV). The anode plate has a hole in its centre and the electrons pass through it and are collimated and focused by a series of magnetic lenses and apertures. The electron beam is used to bombard the sample and produce analytical X-rays from it. The resulting X-rays are diffracted by crystals, then detected, and their intensities measured. In contrast to X-ray fluorescence (XRF) analysis, in electron microprobe analysis X-rays are excited from a very small volume (about 4 to 9  $\mu\text{m}^3$ ) and the analysis is made in a textural context. The unknown composition is determined by comparison with X-ray intensities from materials of known composition (standards).

### **2.2. EMP sample preparation**

Samples for microprobe analysis are mounted, ground flat, and polished. Polishing is essential – samples must be flat on the micrometer scale to avoid variation effects. The preparation is similar to the described in chapter III. Carbon coating (conductive material) is necessary to bleed off the electrical charge produced by the incident electron beam. Carbon is used for coating because it does not absorb most X-rays of interest and is not itself an element of interest. Microprobe samples are coated with a thin (250 Å) layer of pure carbon. The carbon coating is applied by evaporation at high-vacuum. Coating thickness is monitored by the interference colour produced on a clean polished piece of brass; the appropriate interference colour for 250 Å is a “plum” blue.

### 2.3. Results and Discussion

The incorporation of Mg and Sr in shells is important for the process of biomineralization as well as for the paleoceanographic research due to the potential to record physical and chemical changes in the oceanic environment (McCulloch, et al., 1999). Shells of *Patella crenata* consist of 99% CaCO<sub>3</sub>, and the quantity of Mg and Sr is typically about 1% (Pramatarova, 2003).

#### 2.3.1. Aragonite

Figure 48 shows a distinct alternating pattern of an aragonite lamella (Fig. 5-area 3) and the 2D mapping of Ca and Sr (area of 255 x 255 μm).



Figure 48: Microprobe imaging of aragonite and 2D mapping window of Ca and Sr (area of 255 x 255 μm).

The method of qualitative “chemical mapping” (element distribution pictures) yields the distribution of the main component calcium Ca. The 2D mapping of calcium Ca in the aragonite region is shown in Figure 49 (a).

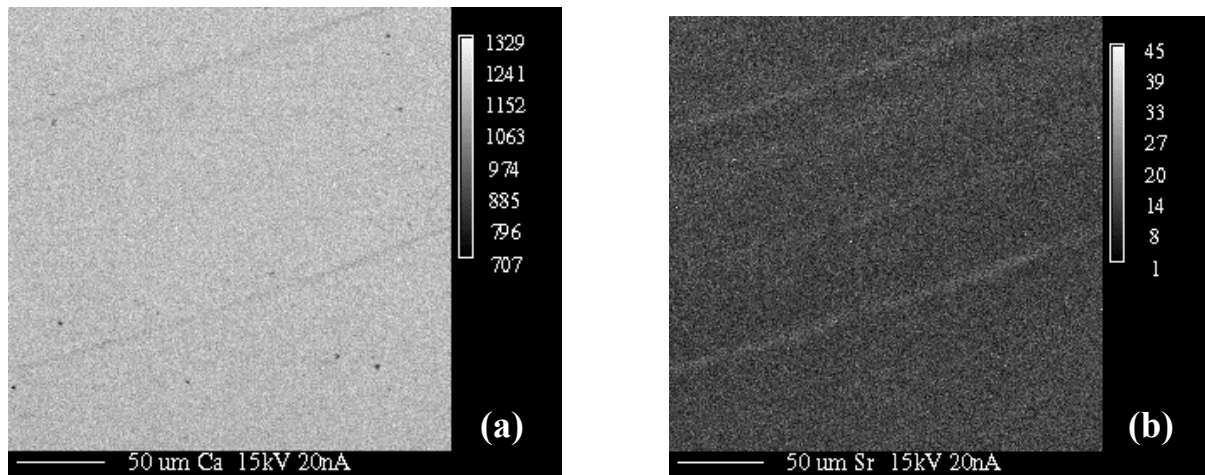


Figure 49: 2D microprobe mapping of aragonite. **(a)** Calcium mapping and **(b)** Strontium mapping.

The distribution of the element Sr is shown in Figure 49 (b). Brighter points correspond to higher concentration of Sr. The strontium mapping shows Sr concentrated along lines. The measured distances between the Sr-rich areas are in the range of 50 to 150  $\mu\text{m}$  and the thickness of the lines is about 6  $\mu\text{m}$ .

### **Quantitative element profile analysis**

Quantitative element profile analysis is obtained, in which 150 individual points along the distance of 162  $\mu\text{m}$  are analysed (dark line in Fig. 48).

Figure 50 shows the data of the strontium distribution along the measured line of first order lamellae and within the bulk between the lamellae, (dark line).

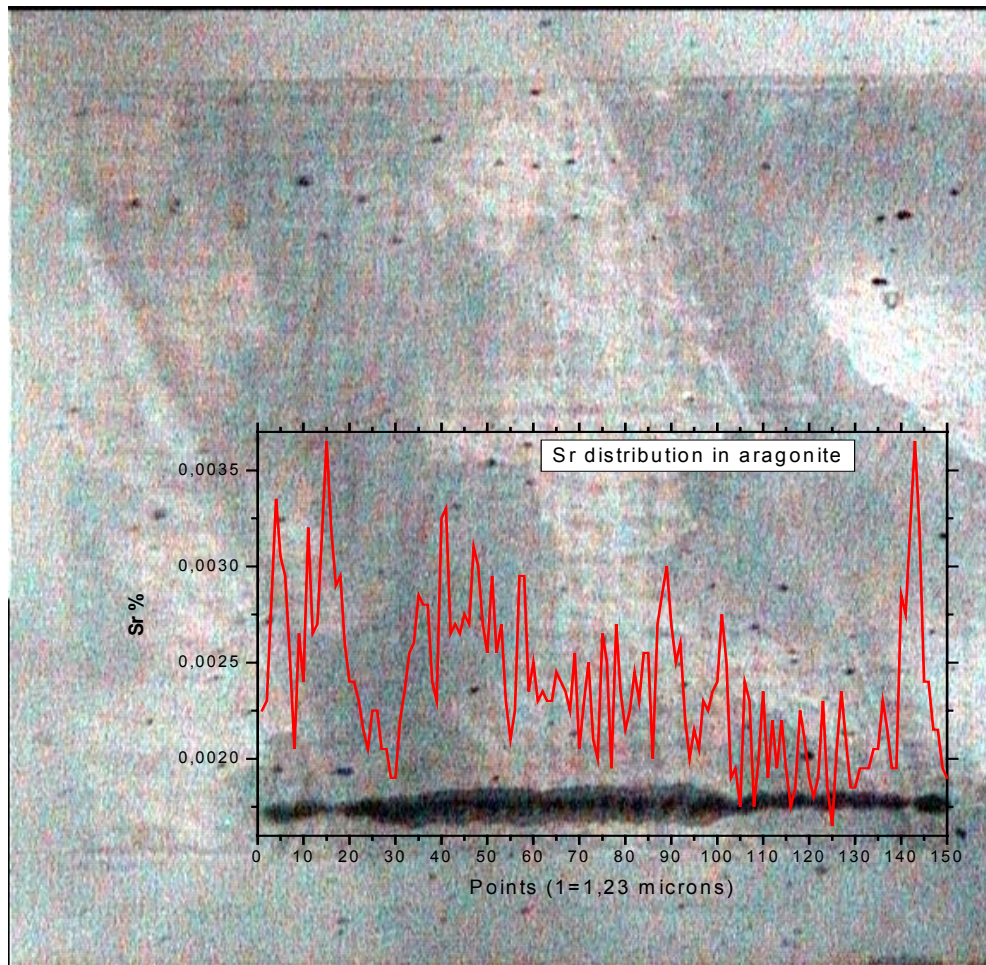


Figure 50: Strontium distribution along the dark line (Fig. 48) first order lamellae and within the bulk between lamellae, obtained by elemental analysis (Sr values in weight percent).

Microprobe analysis yields a maximum strontium content of 0.0035 wt % in first order lamella boundaries and 0.001 wt % in the bulk in aragonite (Figure 50).

### 2.3.2. Calcite

Figure 51 shows optical observation under reflection mode of the distinct alternating lamellae of first order in calcite (Fig. 5, region 1) and their orientation in the 2D mapping area (300x300  $\mu\text{m}$ ) where the Ca and Mg distributions were measured.

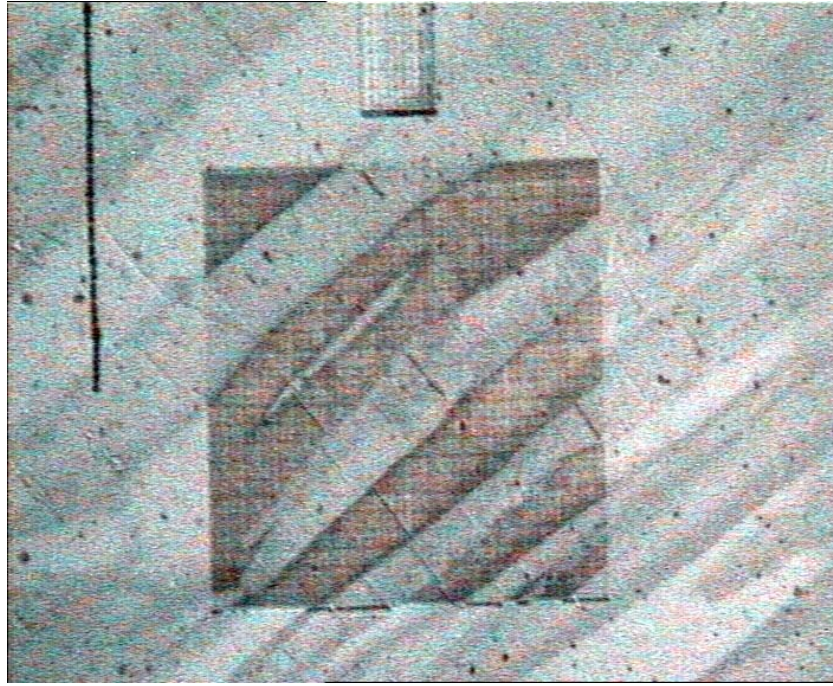


Figure 51: Alternating lamellae of first order in calcite and the 2D mapping area (300x300  $\mu\text{m}$ ) of Ca and Mg distribution measurements.

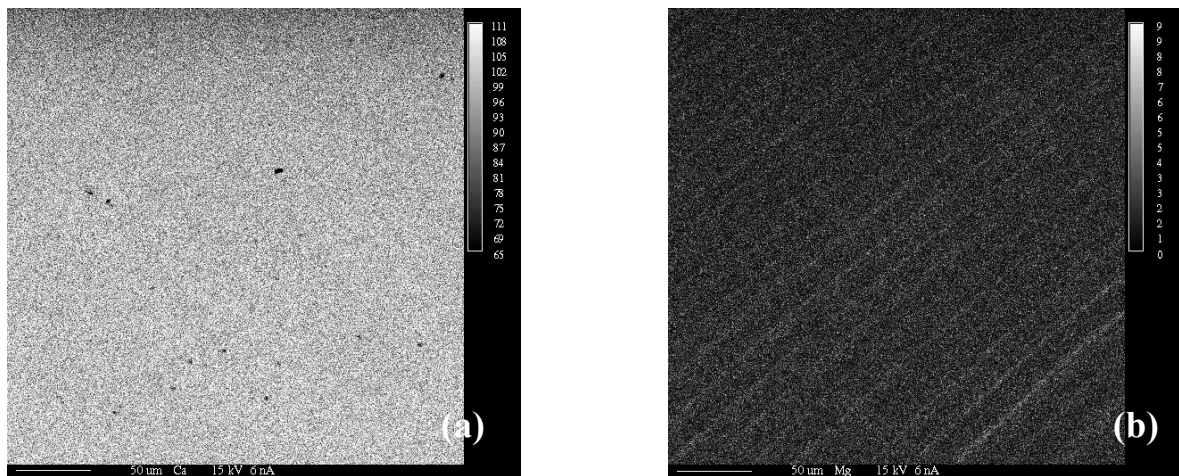


Figure 52: 2D MP mapping of calcite cross section. **(a)** Ca mapping, **(b)** Mg mapping

The qualitative chemical mapping shows the distribution of the main component calcium in calcite in Figure 52, (a). The distribution of the element Mg obtained by 2D mapping is shown in Figure 52, (b). The microprobe (Fig. 52, b) shows Mg peaks displayed as slightly curved lines. The measured distances between the Mg-rich lines are about 20  $\mu\text{m}$  and the thickness of each line is about 3 to 6  $\mu\text{m}$ .

**Quantitative element profile analysis**

A quantitative element profile analysis in calcite is obtained, in which 100 individual points along a line of 415 $\mu\text{m}$  length are analysed.

In Figure 53 the pattern of the bright and the dark lamellae in calcite (corresponding to white lines in the inset) indicates the Mg variation along the horizontal line in the inset.

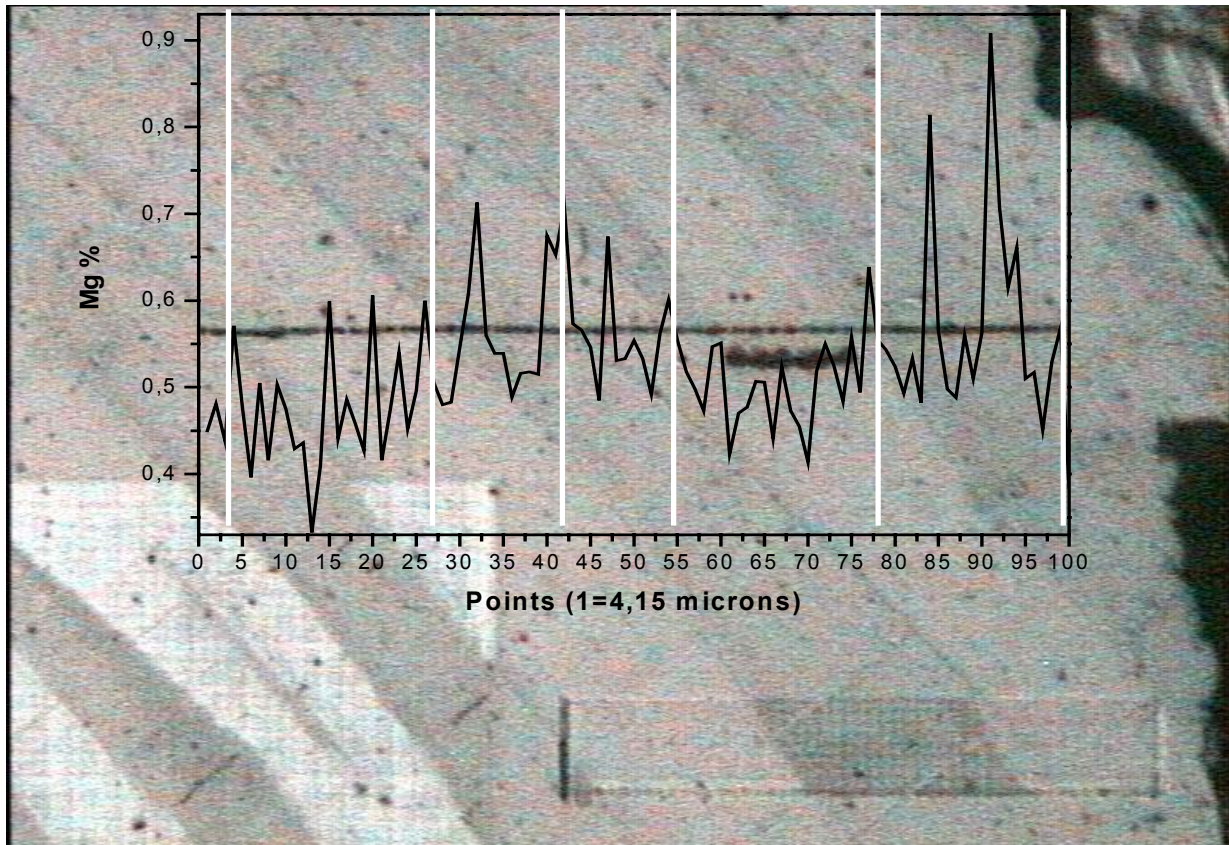


Figure 53: Magnesium distribution along first order lamellae, obtained by quantitative elemental analysis.

Microprobe analysis yields a maximum magnesium content of 0.034 wt % along first order lamellar boundaries and 0.021 wt % within the bulk of lamellae in calcite.

The distribution of strontium and magnesium is plotted (Fig. 50 and 53) based on three oxygen atoms in the structure of  $\text{CaCO}_3$ . The conversion factor (CF) to convert the total oxygen into three, gives  $\text{CF} = 5.0062$ . The conversion for the Ca, C, Mg and O (in atomic weights) are multiplied by the factor CF.

### 2.3.3. Electron interaction with calcite and aragonite using EMPA

Two major factors control the effects that can be detected from the interaction between electrons and sample volume. Beam electrons lose energy as they traverse the sample. Hence, absorption and scattering occurs in the sample. For example, although secondary and Auger electrons are produced throughout the interaction volume, they have very low energies and can only escape from a thin layer near the sample's surface. Similarly, soft X-rays, which are absorbed more easily than hard X-rays, will escape more readily from the upper portions of the interaction volume. Absorption is an important phenomenon and is discussed in details below for the studied aragonite and calcite .

#### Volume of Excitation

The excitation volume is a hemispherical to jug-shaped region with the neck of jug at the specimen surface. The depth of electron penetration of an electron beam and the volume of sample with which it interacts are a function of its angle of incidence, the magnitude of its current, the accelerating voltage, and the average atomic number ( $Z$ ) of the sample. Of these, accelerating voltage and density play the most significant role in determining the depth of electron interaction. Electron penetration generally ranges from 1 to 5  $\mu\text{m}$  with the beam incident perpendicular to the sample.

The depth of electron penetration is approximately (Potts, 1987):

$$x (\mu\text{m}) = \frac{0.1 E_o^{1.5}}{\rho}$$

where  $E_o$  = accelerating voltage (keV),  
and  $\rho$  = density ( $\text{g}/\text{cm}^3$ )

(1)

The width of the excited volume can be approximated by (Potts, 1987):

$$y (\mu\text{m}) = \frac{0.077 E_o^{1.5}}{\rho}$$

where  $E_o$  = accelerating voltage (keV),  
and  $\rho$  = density ( $\text{g}/\text{cm}^3$ )

(2)

Both of these equations are empirical expressions. Using the above empirical relationships, the depth of penetration ( $x$ ) and width of excited volume ( $y$ ) for the minerals aragonite and calcite can be calculated.

Bombarding calcite of density  $2.71 \text{ g/cm}^3$  (a minimum density for carbonate minerals) with electrons of energy  $E_0 = 15 \text{ keV}$ , gives  $x_{cc} = 2.14 \text{ }\mu\text{m}$ . For aragonite of density  $2.93 \text{ g/cm}^3$  and  $E_0 = 15 \text{ keV}$ , the value of  $x_{arg} = 1.98 \text{ }\mu\text{m}$ . At accelerating voltage  $E_0 = 20 \text{ keV}$  the depth of electron penetration will be  $x_{cc} = 3.30 \text{ }\mu\text{m}$  and  $x_{arg} = 3.05 \text{ }\mu\text{m}$  respectively.

Using equation (2), the width of the excited volume for calcite of density  $2.71 \text{ g/cm}^3$ , and bombarding with  $E_0 = 15 \text{ keV}$ , is  $y_{cc} = 1.65 \text{ }\mu\text{m}$ . For aragonite this value is  $y_{arg} = 1.53 \text{ }\mu\text{m}$  respectively. For calcite at accelerating voltage  $E_0 = 20 \text{ keV}$ ,  $y_{cc} = 2.54 \text{ }\mu\text{m}$ .

The quantitative element profile analysis of aragonite at  $E_0 = 15 \text{ keV}$  (black line in Fig. 48) yields  $y_{arg} = 1.08 \text{ }\mu\text{m}$ . For calcite with  $E_0 = 15 \text{ keV}$  the value is  $y_{cc} = 1.35 \text{ }\mu\text{m}$ . The same calcite sample, measured at  $E_0 = 20 \text{ keV}$  (100 points at  $350 \text{ }\mu\text{m}$ , see the line at Figure 54 yields  $y_{cal} = 2.03 \text{ }\mu\text{m}$ .

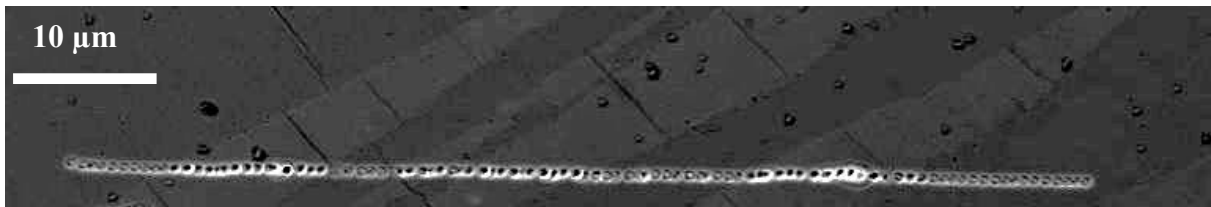


Figure 54: BSE image of calcitic crossed lamellae with scan for elemental quantitative analysis.

Using the empirical expressions 2, the density of aragonite is calculated to be  $\rho_{arg} = 4.14 \text{ g/cm}^3$  and for calcite  $\rho_{cc} = 3.39 \text{ g/cm}^3$ ,

In Figure 54 it is seen, that the depth of penetration ( $x$ ) in the bright lamellae is bigger than in dark lamellae.

### Heat

Significant amount of heat is produced within a sample because electron excitation of X-rays is not very efficient. Many low energy continuum photons and low-energy inelastically scattered electrons do not escape the sample and their energy is transformed into higher vibrational energies of the bonds (heat). The temperature increase for a given material can be expressed as:

$$\Delta T = \frac{4.8 E_0 i}{C_t d_0}$$

where  $E_0$  = accelerating voltage (keV),  
 $i$  = beam current (mA),  
 $C_t$  = thermal conductivity (W/cm·K),  
and  $d_0$  = beam diameter ( $\mu\text{m}$ ).

(3)

The experimental conditions accelerating voltage of 15 keV, beam current of 0.05  $\mu\text{A}$ , beam diameter of 1  $\mu\text{m}$ , calcite thermal conductivity 0.05 W/cm $^\circ\text{K}$  -  $\Delta T = 72^\circ\text{C}$ . The thermal conductivity,  $C_t$ , is the quantity transmitted of heat (Lide, 1998). Thus plotting the temperature rise ( $\Delta T$ ) at an accelerating voltage of 15 keV and a beam current of 50 nA, the respective beam diameters can be specified for each of the studied material.

#### 2.3.4. Backscattered electron images of aragonitic and calcitic crossed lamellae

If the primary electron (electron of the incident beam) interacts with the nucleus or a electron of a sample atom, it may be scattered in any direction with little loss of energy. Some of these scattered electrons will be directed back out of the sample. The backscattered electrons (BSE) are much more energetic than secondary electrons (backscattered electrons are those with energies above 50 eV) and so may escape from a greater depth within the sample. Therefore, compared to secondary electrons, the BSE signal will not carry as much information about sample topography nor will it be as highly resolved in space (resolution). There is a compensating advantage, however. The main influence on the strength of the BSE signal is the mean atomic number of the sample in the interaction volume. The higher the atomic number of an atom, the greater the positive charge of its nucleus and more likely an interaction that produces a BSE. On a backscattered electron image, the brighter the area, the heavier the average atomic mass of the mineral. The BSE signal therefore carries some information about sample composition. Figures 55 and 56 show images of calcite and aragonite cross lamellae in the regime of backscattered electrons (BSE), measured at  $E_0 = 15$  keV.

Figure 55 shows a BSE image of calcitic crossed lamellae of first order. The brighter regions are the heavier elements in of the material. The dark lines observed within the bright lamellae are the border between the lamellae of second order. The measurements show that such dark thin lines contain elements with lighter average atomic mass than those within the lamellae.

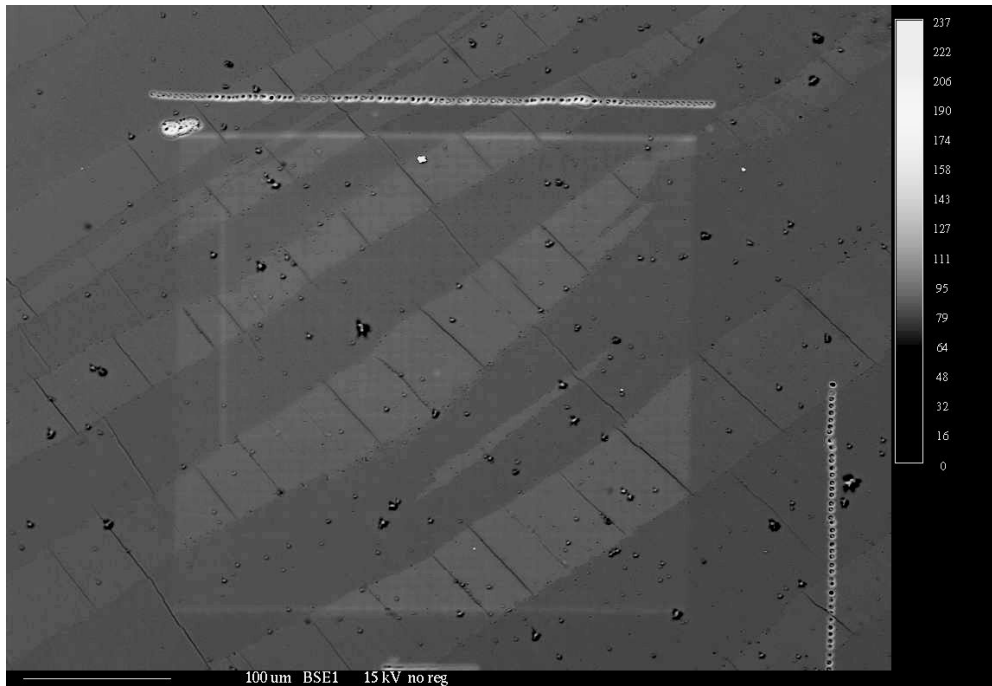


Figure 55: Backscattered electron image of calcitic crossed lamellae.

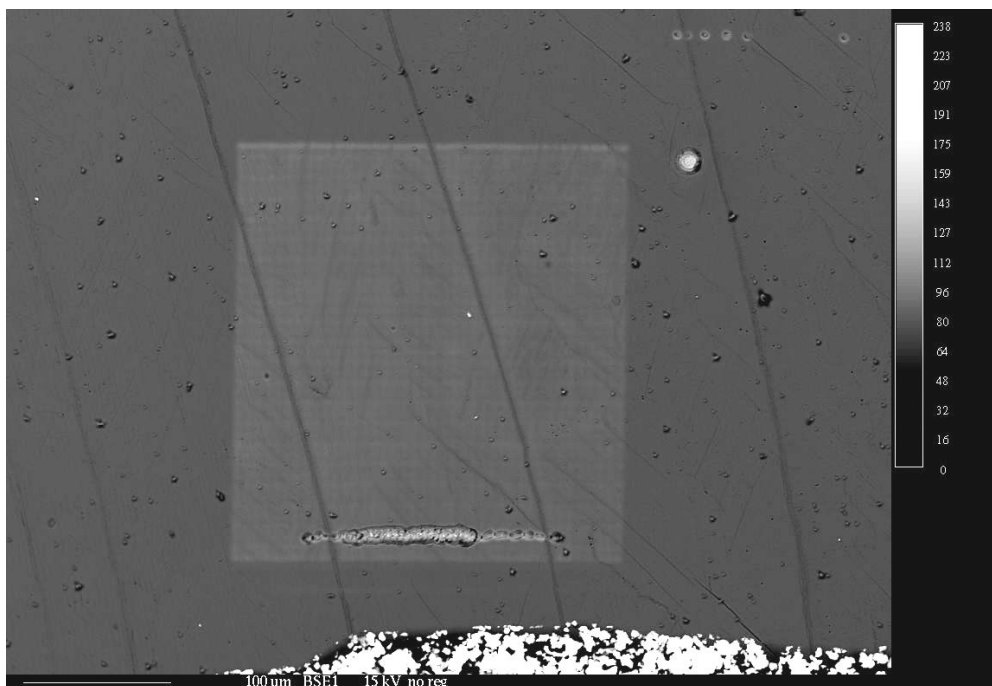


Figure 56: Backscattered electron image of aragonitic crossed lamellae.

The brighter areas (Fig. 56) correspond to the heavier atomic mass of calcium. The darker thin lines are the strontium containing areas.

## **Conclusions**

- Using polarized light microscopy it is observed that the crystallographic *c*-axis of calcitic lamellae of first order is reoriented against the wall boundaries at an angle of about 15°. This result is a sum effect of small crystallites of different orientation.
- Different degree of crystallisation in biominerals of aragonite and calcite in the shell of *Patella crenata* is found using X-ray diffraction techniques.
- The long-range order of the calcitic crossed lamellae is higher in comparison with the aragonitic crossed lamellar material.
- Observations by polarized IR spectroscopy show that the *c*-axis runs almost perpendicular to the calcite lamellae (spot size ca. 40 μm).
- Raman spectra in the aragonitic material show that preferred orientation of the crystallographic axis in the Sr-containing areas differs from that in the bulk of the crossed lamellae.
- Polarised Raman spectra show variations of the crystallographic orientation within the bulk of lamella of calcite.
- The degree of orientational ordering in bright calcitic lamellae is much lower than that in dark calcitic lamellae.
- On the atomistic length scale (HRTEM) the smallest regular cluster size is found to be in the order of 200 Å leading to cluster wise short-range order in the aragonitic material.
- Geometrical reorientation and variations in the concentration of Sr in the aragonitic crossed lamellae cause variations in brightness in the shell.
- The chemical investigations show an oscillatory zoning of due to Mg within the calcitic lamellae.

## **References:**

### **Introduction**

- Bandel, K. (1990) Shell structure of the Gastropoda excluding Archaeogastropoda. Chapter 9 in J. Carter ed. Skeletal biomineralization pattern, processes and evolution trends. 1, p. 117-134. Van Nostrand Reinold, New York.
- Bandel, K. and Geldmacher (1996). Paläontologie, Stratigraphie, Facies. Freiburger Forschungsheft, C 464, Heft 3, 1-71.
- Belcher, A.M., Wu, X.H., Chistensen, R.J., Hansma, P.K., Stucky, G.D. and Morse, D.E. (1996). Control of crystal phase switching and orientation by soluble mollusc-shell proteins. *Nature*, 381, 56-58.
- Lee, W.T. and Salje, E.K.H. (2000). Oscillatory zoning caused by oscillating surface relaxations. *European Physics Journal B*, 13, p. 395-398.
- Macclintock (1967). The Bottegari Lutebook. *JAMS* xx (1967), p. 126
- Pramatarova, R., Bismayer, U., Paulmann, C., Schmidt, H. & Bandel, K. (2000). Investigation of lamellar structures in shell of patella crenata. *HASYLAB, Annual Report, I*, p. 935-937.
- Wang, Y. and Merino, E. (1992). Dynamic model of oscillatory zoning of trace elements in calcite: Double layer, inhibition, and self-organization. *Geochimica et Cosmochimica Acta*, p. 56, 587-596.

### **Chapter I:**

- Brusca, R.C., & G.J. Brusca, 1990. *Invertebrates*. Sinauer Associates, Inc. Sunderland, Mass.
- Carter, J.G., (1990) editor. *Skeletal Biomineralization: Patterns, Processes and Evolutionary Trends*. Volume I, Crenshaw, M. A., p.1-9

From Carter (1990):

Carter, 1980b	Crenshaw. 1980
Carter and Clark, 1985	Creshaw, 1982
Crenshaw, 1964	Dalas et al., 1988
Crenshaw, 1972b;	Erben, 1972
Crenshaw and Neff, 1969	Erben, 1974
Crenshaw and Ristedt, 1975, 1976	Garside, 1982
Creighton, 1984	Gegoire et al., 1955

- Goffinet et al., 1977
- Gordon and Carriker, 1978
- Greenfield, 1987
- Greenfield et al., 1984
- Greenfield and Crenshaw, 1988
- Gregoire, 1962
- Gregoire, 1972a
- Gregoire, 1976;
- Kobayashi, 1984a,b
- Kitano et al., 1976
- Lowenstam 1981
- Mann, 1983
- Misogianes and Chasteen, 1979
- Nancollas, 1982b
- Nielsen and Christoffersen, 1982
- Niggli et al., 1982
- Nordstrom et al., 1979
- Reddy, 1986
- Rieke 1988 a, b
- Sikes et al., 1981
- Sikes and Wheeler, 1986;
- Swift et al., 1986
- Wada, 1961b
- Wada, 1965
- Wada, 1980
- Wada and Fujinuki, 1976
- Watabe, 1981a
- Weiner and Traub, 1980
- Weiner, 1981
- Weiner et al., 1983
- Weiner and Traub, 1984
- Weiner, 1986
- Wheeler, 1983
- Wheeler, 1975
- Wheeler et al., 1981
- Wheeler and Sikes, 1984
- Wilbur and Saleuddin, 1983
- Wilbur and Simkiss, 1968
- Wijsman, 1975
- Wise and Hay, 1968a
- Clarkson, E.N.K., 1993. *Invertebrate Palaeontology and Evolution*. Chapman and Hall, London, p. 434.
- Davis, K.J, Dove, P.M. and J.J. DeYoreo (2000) The role of magnesium as an impurity in calcite growth. *Science*, v. 290, p. 1134-1137.
- Davis, K.J., Dove, P.M. and De Yoreo, J.J. (2001) Molecular-Scale Mechanism for Altered Calcite Morphologies in the Presence of Magnesium: Implications for Impurity Modification of Anisotropic Materials. Spring 2001 Meeting of the Materials Research Society. Casey, A. Malkin, E. Vlieg, M. Ward, p. M9.5.1-M9.5.7.
- Dodd, J.R., and Stanton, R.J., 1981. *Paleoecology, Concepts and Applications*. John Wiley and Sons, New York, p. 559.
- Hickman, C.P., 1961. *Integrated principles of zoology*. The C.V. Mosby Company, St. Louis, p. 972.
- Hickman, C. P., 1967. *Biology of the invertebrates*. The C.V. Mosby Company, St. Louis, p. 673.

- Kozloff, E.N. 1990. Invertebrates. Saunders College Publishing, Harcourt Brace College Publishers, Philadelphia, PA.
- Lehmann, U., and Hillmer, G., 1983. Fossil invertebrates. Cambridge University Press, Cambridge, p. 350.
- Peel, J.S., 1987. Class Gastropoda in Boardman, 1987b.
- Pinna, G. 1973. The World of Fossils. Crown Publishers, New York. p. 128.
- Pojeta, J., 1987. Phylum Mollusca in Boardman, 1987b.
- Tasch, P., 1973. Paleobiology of the Invertebrates - Data Retrieval From the Fossil Record. John Wiley and Sons, New York. 946 p.
- Ruppert, E.E. & R.D. Barnes, 1994. Invertebrate Zoology, 6th Edition. Saunders College Publishing, Harcourt Brace College Publishers, Orlando, FL
- Teng, H.H., P.M. Dove, and J.J. DeYoreo (2000) Kinetics of calcite growth: Surface processes and relationships to macroscopic rate laws. *Geochimica et Cosmochimica Acta*, v. 64, p. 2255-2266.
- Teng, H.H., P.M. Dove, C.A. Orme and J.J. DeYoreo (1998) Thermodynamics of calcite growth: Baseline for understanding biomineral formation. *Science*, v. 282, p. 724-727.
- Weiner, S., (1986), *CRC Crit. Rev. Biochem.* 20, 365 (1986)

## **Chapter II**

- Duda, R., and Rejl, L., (1990): Minerals of the World. Arch Cape Press, New York, 520 p.
- Heinrich, E. W., (1965); Microscopic Identification of. New York, McGraw-Hill Book Company, 414 p.
- Roberts Willard L., Campbell Thomas J., Rapp George R., Wilson Wendell E., (1990) Encyclopedia of Minerals, 2nd ed., Van Nostrand Reinhold, 1990.

## **Chapter III**

- Bandel, K. (1990) Shell structure of the Gastropoda excluding Archaeogastropoda. Chapter 9 in J. Carter ed. Skeletal biomineralization pattern, processes and evolution trends. 1, 117-134. Van Nostrand Reinold, New York.
- Bandel, K. and Geldmacher, W. (1996) The structure of the shell of *Patella crenata* connected with suggestions to the classification and evolution of the Archaeogastropoda.

Paläontologie, Stratigraphie, Facies. Freiburger Forschungsheft, C 464, Heft 3, 1-71, Freiburg.

#### **Chapter IV**

Phillips, Wm. R., (1971). Mineral Optics, Principals and Techniques, ed. By, Gilluly, J. and Woodford, A. O., W.H.Freedman and Company, San Francisco, 1971, pp. 76 , p.82, p.117, p.159

Wenk, H.-R., (1976). Electron Microscopy in Mineralogy. Springer-Verlag Berlin – Heidelberg 1976.

#### **Chapter V**

Eichhorn, K. (1991). DIF4 User's Guide, HASYLAB, 1991.

Fischer, K., Krane, H.-G., Morgenroth, W., (1996). Nucl. Instr. Meth. A 369 (1996) 306

Hammond, C., (2001). The Basics of Crystallography and Diffraction. Oxford University Press, 2001.

Tong, H., Jimin, Hu., Wentao, Ma., Guirong, Zh., Songnian, Y., and Nianxing, C. (2002). In situ analysis of the organic framework in the prismatic layer of mollusc shell. Biomaterials, 23, p. 2593-2598.

Wenk, H.-R., (1976). Electron Microscopy in Mineralogy. Springer-Verlag Berlin Heidelberg New York, 1976.

Woolfson, M. M., (1970). An Introduction of X-ray Crystallography. Cambridge University Press, 1970.

#### **Chapter VI**

Gill, I., Hubbard, D., Olson, J.,m (1995) Corals, paleotemperature recorders, and the aragonite-calcite transformation. Geology, v. 23. p. 333-336.

Fallon S. J., McCulloch M. T., van Woesik R., and Sinclair D. J. (1999). Corals at their latitudinal limits: Laser ablation trace element systematics in Porites from Shirigai Bay, Japan. Earth and Planetary Science Letters 172(3-4), p. 221-238.

- Fisher, D.K., Gale, J.D., and Cygan, R.T., (2000). A shell model for simulation of rhombohedral carbonate minerals and their point defects, *American Mineralogist*, v. 85, p. 217-224.
- Paloczi, G.T., B.L. Smith, P.K. Hansma, and D.A. Walters. 1998. Rapid imaging of calcite crystal growth using atomic force microscopy with small cantilevers. *Appl. Phys. Lett.* 73(12), p. 1658-1660.
- Riesz, F., (2000). A quantitative approach to makyoh (magic mirror) topography. *Journal of Crystal Growth* 210 (2000) 370;
- Riesz, F., (2000). Geometrical optical model of the image formation in makyoh (magic mirror) topography. *Journal of Physics D: Appl. Phys.* 33 (2000) 3033.
- Riesz, F., Pramatarova, L.D., Pramatarova, R., Tóth, A.L. (2002). Makyoh-topography studies of the morphology of the cross sections of renal stones. *Journal of Crystal Growth* 245 (2002), p. 101-108.
- Smith B.L., Paloczi, G.T., Hansma, P.K., Levine, R.P. (2000). Discerning nature's mechanism for making complex biocomposite crystals. *Journal of Crystal Growth*, 211, p. 116-121.
- Teng, H., P.M. Dove, C.A. Orme and J.J. DeYoreo (1998) Thermodynamics of calcite growth: Baseline for understanding biomineral formation. *Science*, v. 282, p. 724-727.
- Walters, D. A., B. L. Smith, et al. (1997). Modification of calcite crystal growth by abalone shell proteins: An atomic force microscope study. *Biophysical Journal* 72(3), p. 1425-1433.

## **Chapter VII**

- Decius, J.C. and Hexter, R. M. (1987) *Molecular Vibrations in Crystal*, McGraw, New York.
- Farmer, V. C. (1974) *The Infrared Spectra of Minerals*, Mineralogical Society, London.
- McMillan, P.& Hoffmeister, (1988) Infrared and Raman spectroscopy. In *Spectroscopic methods in Mineralogy and Geology*. Rev. Mineral., Hawthorne, F. (Ed) Vol. 18. p. 99-159
- McMillan, P. (1989). Raman spectroscopy in mineralogy and geochemistry. *Ann. Rev. Earth and Planet. Sciences*. Vol. 17, p. 255-283
- Nakamoto, K., Ferraro, J. R., (1994). *Introductory Raman spectroscopy*. Academic Press, 1994, p.78-81

- Nakamoto, K. (1986). *Infrared and Raman Spectra of Inorganic and Coordination Compounds*. 4<sup>th</sup> edition, Wiley-Interscience, New York, 1986, p. 91-97 and p.125-129.
- Salje, E. and Viswanathan, K. (1978) The phase diagram calcite-aragonite as derived from crystallographic properties. *Contributions to Mineralogy and Petrology*, 55, p. 55-67.
- Weiss, I. M., Tuross, N., Addadi, L. and Weiner, S., (2002). Mollusc Larval Shell Formation: Amorphous Calcium Carbonate Is a Precursor Phase for Aragonite. *Journal of Experimental Zoology*, 293, p. 478-491 (2002)
- Williams, Q. (1995). *Infrared, Raman and Optical Spectroscopy of Earth Materials*. Mineral Physics and Crystallography. Ahrens, T.J. (Ed) AGU Reference Shelf 2. 1995, p. 291-302.

### **Chapter VIII**

- Herrmann, F. and Grambole, D. (1995). The New Rossendorf Nuclear Microprobe. *Nuclear Instruments and Methods in Physics Research B* 104, p. 26-30.
- Lide, D.R. (Ed.) (1998) in *Chemical Rubber Company handbook of chemistry and physics*, CRC Press, Boca Raton, Florida, USA, 79th edition.
- Markwitz, A., Grambole, D., Herrmann, F., Trompeter, W.J., Dioses, T., and Gauldie, R.W. (2000) Reliable micro-measurement of strontium is the key to cracking the life-history code in the otolith. *Nuclear Instruments and Methods in Physics Research B*, 168, p. 109-116.
- Mason, B. and Bery, L. G. (1968). *Elements of Mineralogy*. W. H. Freeman and company, San Francisco, p. 330.
- McCulloch M. T., Tudhope A. W., Esat T. M., Mortimer G. E., Chappell J., Pillans B., Chivas A. R., and Omura A. (1999). Coral record of equatorial sea-surface temperatures during the penultimate deglaciation at Huon Peninsula. *Science* 283, p. 202-204.
- Potts, P. J., (1987). *A Handbook of Silicate Rock Analysis*. Blackie, p. 336-337.